Fall 2011

On the ability of indentation to capture the anisotropic elastic properties of the pyrolytic carbon

Nikolay Timoshchuk
University of New Hampshire, Durham

ON THE ABILITY OF INDENTATION TO CAPTURE THE ANISOTROPIC ELASTIC PROPERTIES OF THE PYROLYTIC CARBON

BY

NIKOLAY TIMOSHCHUK

B.S.M.E., University of New Hampshire, 2009

THESIS

Submitted to the University of New Hampshire

in Partial Fulfillment of

the Requirements for the Degree of

Master of Science

in

Mechanical Engineering

September, 2011

This thesis has been examined and approved.

Thesis Director, Todd S. Gross, Professor and Chair of Mechanical Engineering

Thesis Co-Director, Igor I. Tsukrov, Professor of Mechanical Engineering

James E. Krzanowski, Professor of Mechanical Engineering

8/10/2011

Date

ACKNOWLEDGEMENTS

I would like to express my deepest gratitude to my graduate adviser Professor Todd Gross for his guidance of this research. Without his expertise and knowledge, this research would not have come this far in this amount of time. I also would like to thank him for his advice and support throughout writing of this thesis.

I am very thankful to my co-adviser Professor Igor Tsukrov for providing with valuable directions and insights on the research and assisting with the finite element modeling. I also would like to acknowledge Doctor Boris Reznik for his generous support and guidance during my stay at the Karlsruhe Institute of Technology in Germany and for contributing to this research.

I wish to thank Professor Jo Laird for allowing me to use the Petrology lab at the Department of Earth Sciences to perform the optical analysis using PLM. I am indebted to undergraduate students Khanh Nguyen and Michael Buck for performing the macroscopic tests on the samples of the bulk PyroC using strain gages. Many thanks to my lab-mate Anjali Parkhi, for making the AFM lab a fun place to work at, and to the undergraduate student Nicholas Landry for helping with the nanoindentation experiments.

I am also grateful to my family and to my fiancé Alla Maslov for supporting and believing in me throughout my graduate studies. Without them, it would be immeasurably more difficult to complete my research.

This research was supported by the National Science Foundation (NSF), Division of Materials Research, Materials World Network program grant number 0806906.

TABLE OF CONTENTS

LIST OF TABLES

LIST OF FIGURES

ABSTRACT

ON THE ABILITY OF INDENTATION TO CAPTURE THE ANISOTROPIC ELASTIC PROPERTIES OF THE PYROLYTIC CARBON

by

Nikolay Timoshchuk

University of New Hampshire, September, 2011

We used micro- and nanoindentation, macroscopic strain gage methods and FE studies to correlate the indentation modulus and the macroscopic in- and out-of-plane Young's moduli of transversely isotropic pyrolytic carbon. The out-of-plane indentation modulus of bulk PyroC was comparable with predicted values and more than a factor of two higher than the out-of-plane Young's modulus. The in-plane indentation modulus was significantly lower than predicted values which we attribute to nanobuckling of graphite-like planes. Polarized light microscopy studies on carbon-carbon composite samples infiltrated at 10, 20, 30 kPa demonstrated that the increase in pressure leads to lower texture of the PyroC and higher in-plane indentation modulus due to a decreased tendency toward nanobuckling for more isotropic structures. We observed damage of PyroC layers at critical loads when indenting normal to the plane of isotropy and attribute the damage to a combination of crack propagation and delamination types of deformation mechanisms.

CHAPTER 1

INTRODUCTION

Background on Carbon-Carbon Composites

Originally developed for aerospace industry, carbon-carbon (C/C) composites emerged as a high-performance, cost-effective alternative to refractory metals able to resist the rigors of the most extreme environments. C/C composites, comprised of carbon fibers surrounded by a carbonaceous matrix, can withstand the temperatures up to 500 °C in air and 3000 °C in vacuum[1]. This material, having only one-tenth the density of most refractory metals, features a unique set of properties including high stiffness-to-weight ratio, high heat capacity and thermal conductivity, low coefficient of thermal expansion, low reactivity, etc. It is used in a number of applications, most of which are exposed to very high temperatures. Examples would include heat shields and motor exhaust nozzles of space shuttles, brake pads and rotors of aircrafts and high-performance vehicles. Other commercial applications include furnace fixtures, heating elements, X-ray targets, etc.

Carbon fibers serve as a back-bone of the C/C composites. They can be either Polyacrylonitrile (PAN), mesophase pitch- (MP), or rayon based carbon fibers arranged in a certain pattern or randomly. The strength of carbon fibers is used to reinforce the carbonaceous matrix that surrounds them. One of the most common ways of manufacturing this matrix is by the means of chemical vapor infiltration (CVI).

Chemical Vapor Infiltration (CVI) Method

CVI is a deposition type technique in which reactant gases diffuse into an isothermal porous preform in the absence of oxygen. This method can be used to infiltrate a number of different preforms and to fabricate various ceramic matrix materials such as alumina or silicon carbide. It can also be used to produce a graphite-like matrix material. A schematic[2] of the CVI process used to fabricate a carbonaceous matrix is shown in Figure 1.

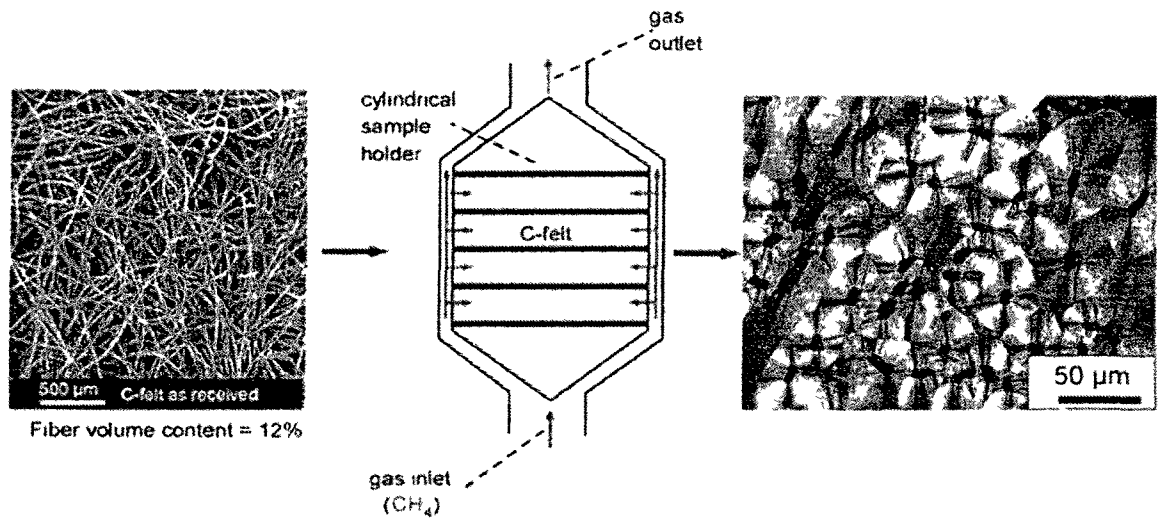

Figure 1: Schematic[2] of the CVI process showing carbon fiber preforms/felts (left) placed into a reactor chamber (center). The decomposition of a hydrocarbon gases within the chamber at high temp and low temp leads to the buildup of the carbonaceous matrix around fibers (right).

Bundles of carbon fiber preforms are initially placed in an insulated chamber. After pressure and temperature inside the chamber reach a steady-state, a hydrocarbon gas (such as methane, propane, ethane, etc.) is delivered at the inlet. The pressure and temperature ranges are typically 10-50 kPa and above 1000 °C respectively. These conditions trigger the decomposition of the precursor gas into polycyclic aromatic

hydrocarbon planes that are deposited onto the surface of the fiber preform. The condensation reactions of these planes stacked on the surface in coplanar manner forms the layers of the pyrolytic carbon matrix wrapped around the fibers[3]. The densification process is not ideal so there is a significant amount of porosity typically amounting to over 10% of the total volume.

Structure of the Pyrolytic Carbon

At the atomic level, the pyrolytic carbon may fairly be called a graphite-like material in which the atoms are arranged in open hexagons and the layers show some sort of a stacking sequence[4] as shown in Figure 2. Unlike graphite, the structure of pyrocarbons is limited to two dimensions (i.e. the hexagonal lattice of an aromatic layer) and known as the turbostratic structure.

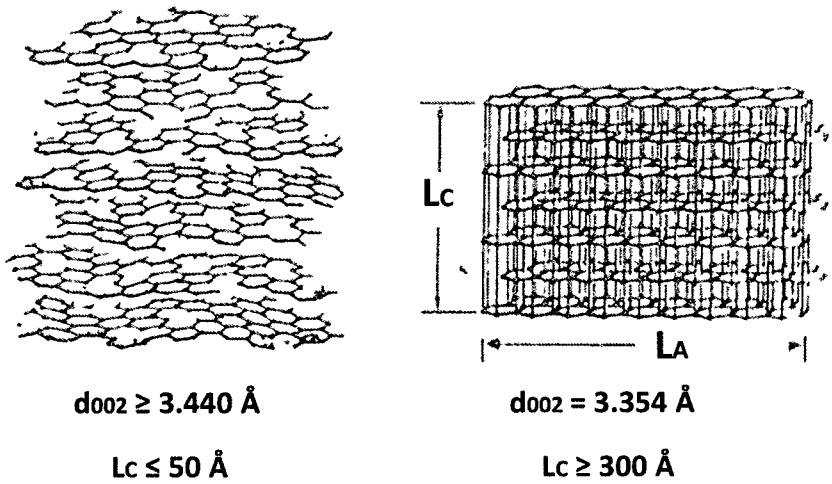

Figure 2: Schematics of (a) a turbostratic structure of the pyrocarbon and (b) an ideal graphite crystal structure. Retrieved from "Multi-Scale Study of Chemical Vapor Infiltrated Carbon/Carbon Composites", presented by A. Li at the 1st DFG-NSF-All Project meeting in Sept 2008.

PyroC exhibits strong in-plane elastic properties, such as the in-plane Young's modulus, that are governed by covalent bonds within the basal plane hexagons. The bonding between crystallites, however, is not well understood, but the basal planes seem to exhibit some cross-linkage which is often referred to as "weak Van der Waals bonds". This material is classified as a transversely isotropic polycrystalline solid.

Figure 3 shows SEM and TEM images of an infiltrated C/C composite at the micro and nano levels. This image demonstrates a very complex hierarchical microstructure of the PyroC with distinct layers visible at microscale and with coherent domains (stacks of well aligned carbon layers) at the nanoscale, so the term "layer" is rather ambiguous.

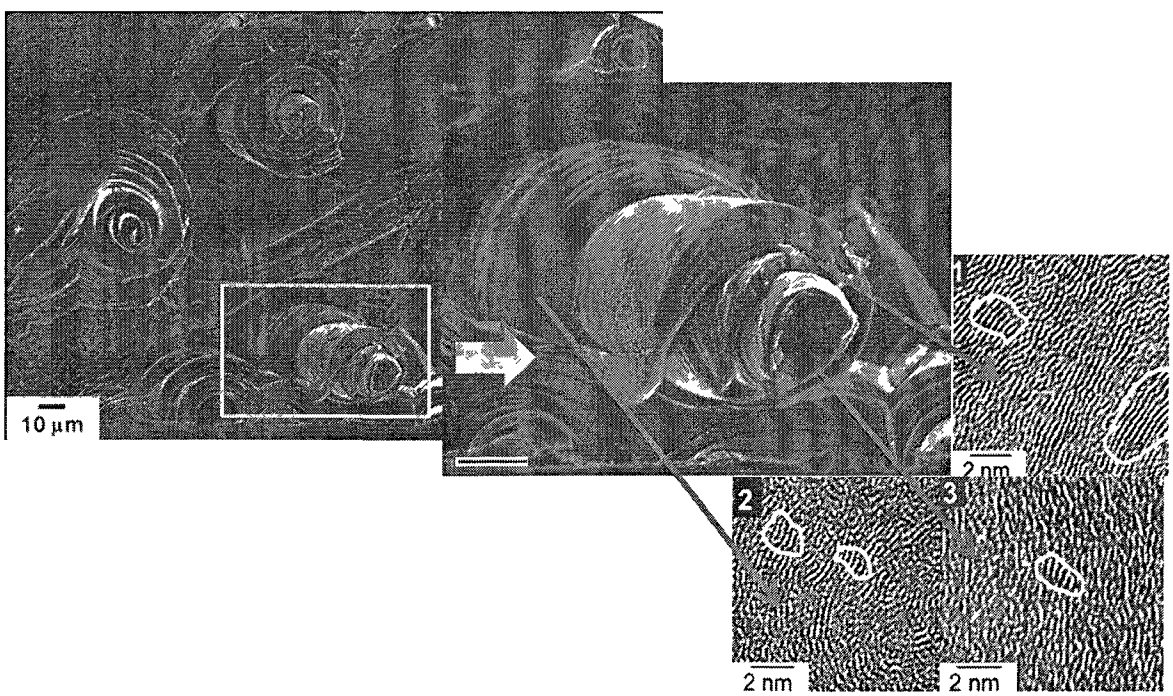

Figure 3: Complex layered microstructure of the pyrolytic carbon on various length scales. SEM images show layers of the PyroC wrapped around fibers at microscale. TEM images show the orientation of the coherent domains as a function of distance from the fiber at nanoscale. Retrieved from "Materials World Network: Multi-Scale Study of CVI C/C composites", presented by B. Reznik at the 1st DFG-NSF-All Project meeting in Sept 2008.

Three TEM images of the PyroC matrix taken at different distances away from the fiber show a variation in the alignment of the coherent domains. This variation suggests a textural gradient and, ultimately, a mechanical properties gradient of the pyrolytic carbon as a function of distance from the fiber.

The texture of the pyrolytic carbon within C/C composites has been extensively studied by some research groups in the past. Oberlin[5] provided a thorough overview of various kinds of pyrocarbon materials and discussed how this material can be characterized using optical microscopy, transmission electron microscopy, and diffraction methods.

Reznik et al[6-13] showed the correlation between the optical anisotropy and structural anisotropy of differently textured PyroC layers using polarized light microscopy (PLM), high resolution transmission electron microscopy (HRTEM), and atomic force microscopy (AFM). They utilized a method for angular-resolved characterization of the optical anisotropy of the pyrolytic carbon[14] by measuring the so-called extinction angle, *Ae*. These papers show that the optical anisotropy of the PyroC is directly related to the microstructural anisotropy. They classified different preferred orientations, or textures of the pyrolytic carbon layers in relation to the surface of the fibers into isotropic, low, medium, and high texture as shown schematically[6] in Figure 4.

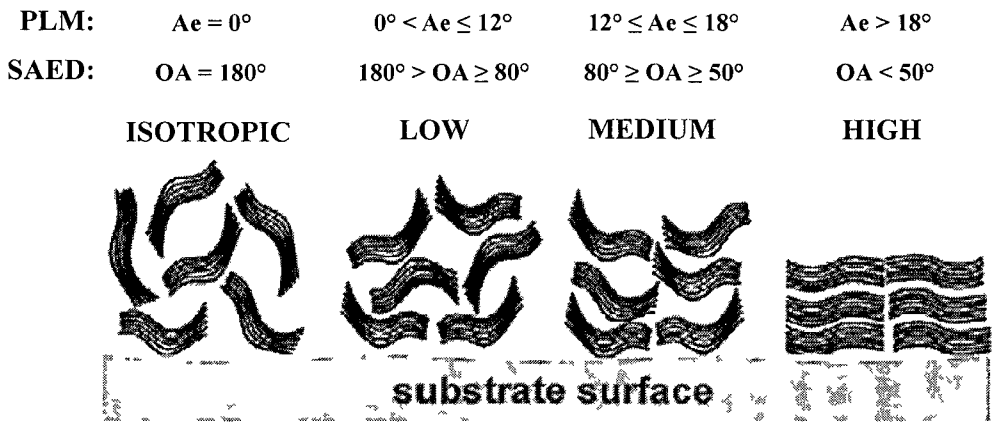

Figure 4: Schematic[6] of different preferred orientations of PyroC layers in relation to the substrate surface characterized by the extinction angle, Ae, using PLM or by the orientation angle, OA, determined by SAED measurements.

In case of the HRTEM studies, the optical anisotropy is determined by measuring the orientation angle, *OA*. The measurement procedure of *Ae* and *OA* are described in detail by Bourrat et al[15,16] and by Bortchagovsky et al[17 18].

Bulk Pyrolytic Carbon

The pyrolytic carbon material discussed in this thesis (will also be referred to as bulk PyroC) was purchased from the company named Schunk Kohlenstofftecknik GmbH, Heuchelheim, Germany. It was manufactured by chemical vapor deposition in the form of 100 mm diameter disk with a nominal thickness of 1.5 mm. The manufacturer stated that the impurity content of the material does not exceed 10 ppm. The micrographs of this material's cross-section obtained using PLM and SEM are shown in Figure 5 (a) and Figure 5 (b) respectively.

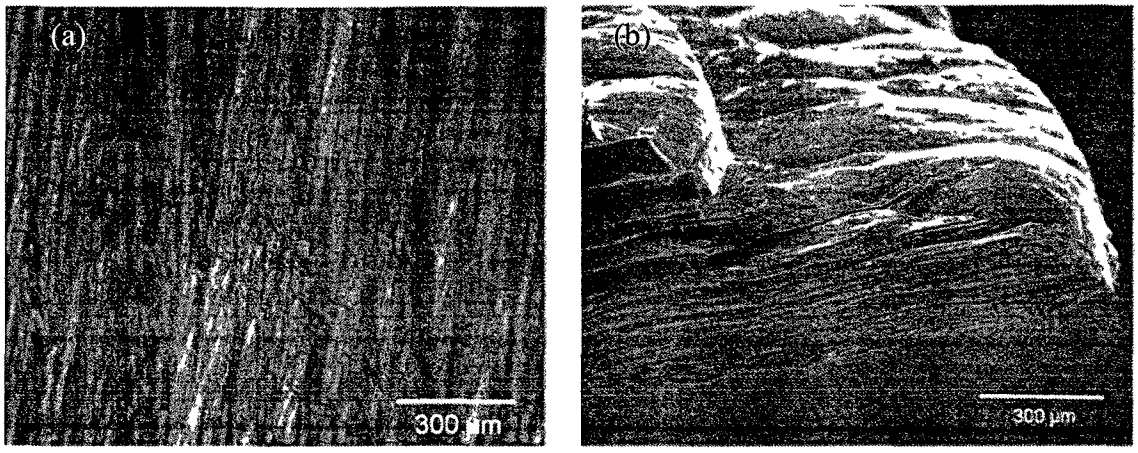

Figure 5: (a) PLM image of the bulk PyroC in cross-section showing the columnar features and (b) SEM image of fractured portion of the bulk PyroC showing layered structure. Image (b) Retrieved from "A model of the spatial organization of pyrolytic carbon", presented by B. Reznik at the NSF-DFG-All Project meeting in Mar 2010.

Each of these images displays distinct features of the pyrolytic carbon microstructure. The microstructure observed in PLM exhibits a ~10 µm wide columnar features that exist through the thickness of a pyrolytic carbon. Their origin and significance is still not well understood. However, these columnar features are not visible in scanning electron microscope. Instead, a unique structure of stacked graphene layers of various thicknesses can be observed on the fractured sample in SEM as shown in Figure 5 (b).

The SEM image in Figure 6 (a) shows the kinked, turbostratic structure of the PyroC on the microscale while the HRTEM image in Figure 6 (b) displays the individual stacks of roughly aligned graphene planes that are also kinked within discontinuous domains.

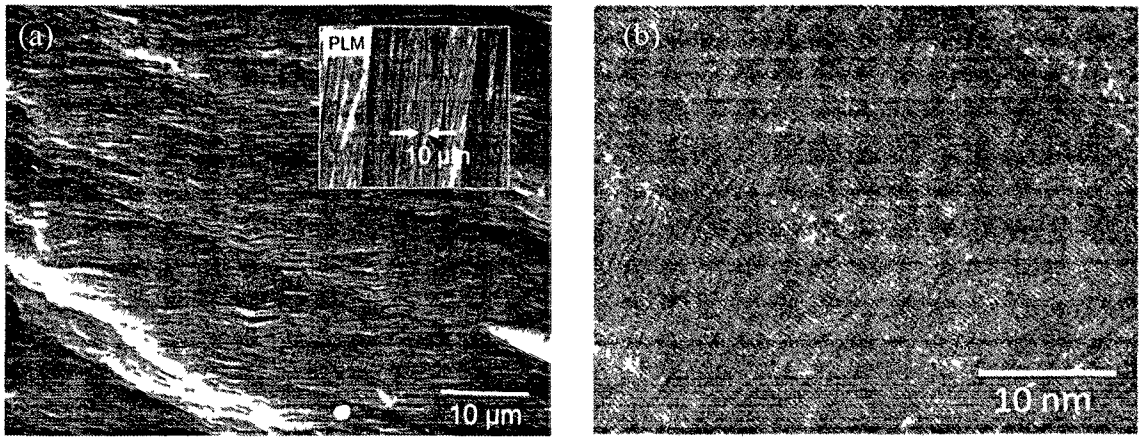

Figure 6: (a) SEM image of fractured portion of the bulk PyroC sample showing turbostratic, kinked structure and (b) HRTEM image of the high-textured kinked graphene planes and discontinuous domains. Retrieved from "A model of the spatial organization of pyrolytic carbon", presented by B. Reznik at the NSF-DFG-All Project meeting in Mar 2010.

The micrographs of the bulk PyroC in the deposition plane (i.e in the plane of isotropy) are shown in Figure 7 (a-b).

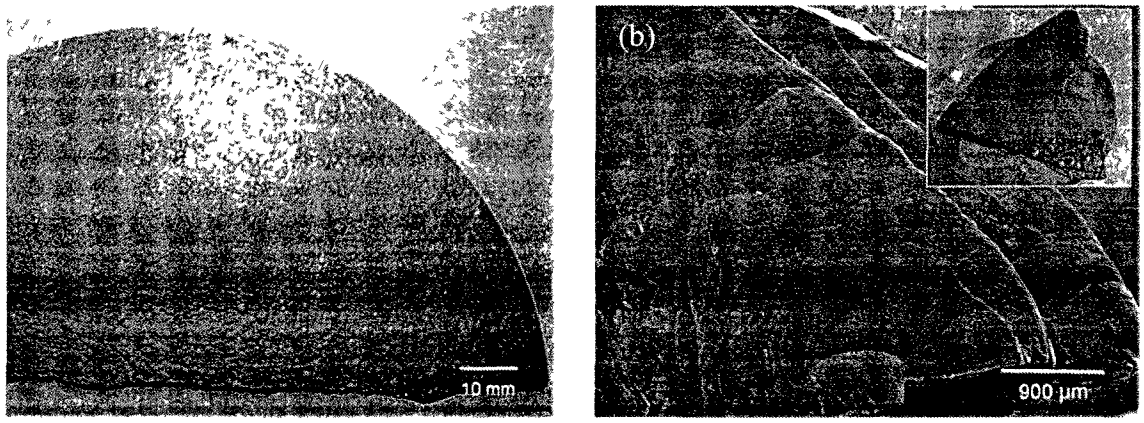

Figure 7: Micrographs of the bulk PyroC as observed in (a) PLM and (b) SEM. Retrieved from "A model of the spatial organization of pyrolytic carbon", presented by B. Reznik at the NSF-DFG-All Project meeting in Mar 2010.

The "bubble"-like features of the material in the deposition plane, which are the tops of the columnar features, make it very difficult to polish a smooth surface sufficient for atomic force microscopy and for nanoindentation. In their recent studies, Gebert et al[19] used PLM and TEM to show that the bulk PyroC samples do not exhibit textural

gradients along the deposition direction. They also showed that PyroC exhibits transverse isotropy by measuring all its independent elastic constants by ultrasonic phase spectroscopy.

Carbon-Carbon Composite Project

The degree of texture and, ultimately, the mechanical properties of the pyrolytic carbon matrix, are strongly influenced by the deposition and annealing conditions as first reported by Bokros and Price[20] in 1966. They identified several factors that impact the resulting microstructure/mechanical properties of a pyrolytic carbon material obtained by decomposing a hydrocarbon gas including, but not limited to: (1) the precursor gas, (2) the temperature and pressure of pyrolysis, (3) the residence time, and (4) the geometry of the reactor. Therefore, an ability to correlate the texture to the mechanical properties so that one can identify the desirable microstructures that will ultimately be produced by optimizing the deposition/annealing conditions would significantly advance the understanding of the C/C composites manufacturing using CVI and make the production of this material more affordable.

Research groups from the University of New Hampshire (UNH) and from the Karlsruhe Institute of Technology (KIT) in Germany joined efforts to perform a multi-scale study of chemical vapor infiltrated C/C composites. The goal of the project was to increase the fundamental understanding of how nanotexture and microstructure of C/C composites are defined by the CVI parameters and to develop a multi-scale numerical model relating microstructure on nano-, micro-, and meso-levels to the overall material properties.

The material production was performed at KIT where they have the facilities to manufacture C/C composites using CVI. The optical characterization was also carried out by the experienced staff at KIT where they have the necessary equipment to conduct a comprehensive optical analysis of the C/C composite microstructure using PLM, SEM, TEM, HRTEM, etc. We also used PLM techniques to measure the degree of the optical anisotropy of the supplied C/C composite samples. The material modeling was performed by the research groups from both universities which included the multi-scale models of the elastic properties, thermomechanical behavior, etc. They utilized the micromechanical modeling, texture modeling using correlation functions, and FE modeling methods.

The focus of our research was to conduct multi-scale mechanical testing to validate the models developed by our collaborators. Nanoindentation method was the primary tool because it allows measuring the near-surface elastic properties with the micrometer spatial resolution. Considering that the typical diameter of the fibers is only 10 μm and the thickness of the pyrolytic carbon layers around fibers rarely exceed 30-40 μm, it seemed to be the most appropriate mechanical method capable of estimating the elastic property gradients through the thickness of the PyroC layers. Both the bulk pyrolytic carbon samples as well as the PyroC within C/C composites were studied using nanoindentation.

We also utilized microindentation on the bulk pyrolytic carbon samples. If nanoindentation operates on sub-micron to micro-scale, microindentation operates on the scale of one to two orders of magnitude higher. In addition, we performed macroscale tensile and compression tests on the samples of the bulk PyroC.

Literature Review

Nanoindentation, seemingly an ideal technique to measure the elastic properties with the micrometer spatial resolution, presents significant challenges concerning with its ability to characterize the carbon-like materials. Pyrolytic carbon is a transversely isotropic solid with a turbostratic layered structure. Methods employed to estimate the elastic properties, such as Young's modulus or hardness, are oriented for the isotropic materials. In addition, pyrolytic carbon tends to exhibit an elastic response to indentation and does not yield in a similar manner to the materials for which the indentation method analysis methods were developed.

Indentation-based techniques have been utilized on variety of carbon materials in the past with several authors reporting on a purely elastic response to indentation[21-23,25,27,28,31]. Sakai et al[21] performed Vickers indentation on glassy carbons produced by different densification processes. They considered a large load range (0 to 20 N) and observed a purely elastic response of the loading and unloading load-displacement curves.

Diss et al[23] performed micro- and nanoindentation tests on C/C composites and on other carbons such as HOPG, glassy C, smooth and rough laminar pyrocarbons. They observed a nearly elastic response for low loads (<100 mN for microindentation) and utilized the Sneddon's solution[24] to estimate the elastic modulus of the material. They observed crack initiation at higher loads. Although most materials they tested exhibited a high degree of anisotropy, they claimed the indentation modulus to be an effective Young's modulus. This is highly unlike the case for anisotropic materials. Even though

they acknowledged the possible effect of the material structure on the indentation modulus estimates, they did not investigate the effects of the orientation of the basal planes with respect to the loading direction.

Similarly, Marx at al[25] used nanoindentation methods on five different C/C composites as well as on isotropic and anisotropic CVD carbons. They utilized the standard elastoplastic approach proposed by Oliver and Pharr[26] to estimate the modulus values. They also observed that the carbon materials exhibit almost completely elastic response to indentation. However, the effects of anisotropy were not considered as the only one value of modulus was given for anisotropic CVD carbon. The difference in modulus' values of ICVD (30.69±0.97 GPa) and ACVD (29.92±0.94 GPa) were not statistically significant.

Hoffman et al[27] performed nanoindentation tests on the pyrolytic carbon coating deposited onto stationary graphite rods by decomposing a mixture of propane and nitrogen at atmospheric pressure within a fluidized bed reactor at 1350 °C. The indentations were made transverse to the deposition direction. They estimated the modulus to be 24.4 ± 0.8 GPa for the smooth deposits and 8.8 ± 1.9 GPa for rough deposits. They made an assessment that the pyrolytic carbon coating was isotropic based on the optical observations using the polarized light microscopy. The load-displacement curves exhibited nearly elastic behavior and the standard elastoplastic analysis method[26] for isotropic materials were employed to estimate the modulus.

More thorough studies were performed by López-Honorato et al[28] who used nanoindentation to characterize PyroC deposited from acetylene or a mixture of

acetylene/propylene onto 0.5 mm alumina spheres in a fluidized CVD bed over a wide range of deposition conditions. They performed nanoindentation both normal and parallel to the deposition plane of the PyroC. By utilizing standard elastoplastic method[26] for isotropic materials to estimate the modulus, they found that the material exhibited higher nanoindentation-derived moduli values perpendicular to the deposition plane. They also observed a drop in modulus from 30 to 13 GPa as a result of reducing the manufacturing temperature. They concluded that anisotropy, domain size and level of graphitization have a strong influence on mechanical properties of the pyrolytic carbon.

Guellali et al[29,30] performed three-point bending tests to measure the elastic modulus of the highly textured PyroC subjected to different heat treatments. The in-plane elastic modulus of as-deposited PyroC was found to be on the order of 17.8-18.5 GPa. There was an approximately 10% increase in Young's modulus for the sample which was heat treated up to 2900°C/2hr (~21 GPa). They attributed this phenomenon to the fact that heat treatment leads to further graphitization (i.e. PyroC become more high textured) and a higher fraction of σ-bonding in xy-plane.

Ozcan et al[31] investigated the effects of heat treatment at temperatures between 1800 °C and 2400 °C on the microstructure and elastic properties of individual components of C/C composites using PLM, HRTEM, and nanoindentation techniques. They considered two types of commercial C/C composites: a two directional randomly chopped pitch fiber reinforced composite with charred resin/CVI matrix and a three directional PAN fiber composite with CVI matrix. They observed that the heat temperature treatment (HTT) in some cases leads to the formation of a better organized microstructure of fibers and the matrix and also to thermal cracks. Heat treated samples

of the rough laminar pyrocarbon matrix yielded lower estimates of the indentation modulus (18 GPa before and 12 GPa after HTT), and they attributed these results to shearing and kinking of the graphene sheets within better-organized microstructures. They utilized the Oliver and Pharr method[26] to estimate the modulus.

Gebert et al[19] characterized the microstructure of the bulk PyroC samples (the same material as discussed in this thesis), and performed ultrasound phase spectroscopy to measure the elastic constants. They used polarized light microscopy and high-resolution transmission electron microscopy to show that this particular pyrolytic carbon material is highly-textured and does not exhibit a textural gradient in the direction of deposition. The independent elastic constants were estimated from the velocity of longitudinal and shear waves. While some of the stiffness components C_{12} and C_{13} have relatively large error (17% and 46% respectively), the engineering elastic modulus values were estimated and exhibited transverse isotropy with 12.8 GPa parallel to the growth direction (out-of-plane modulus), and 27.1 GPa transverse to the growth direction (in-plane modulus).

Scope of Research

This research was conducted to provide the experimental support to the multidisciplinary efforts of characterizing carbon-carbon composites on various length scales. Although the ultimate goal was to establish the correlation between various degrees of texture of the pyrolytic carbon and elastic properties, the extent of the material presented in this master thesis is primarily concerned with the ability of the sharp indentation methods, particularly nanoindentation, to accurately capture the anisotropic elastic properties of the pyrolytic carbon. We utilized the samples of the bulk PyroC for

which the elastic constants were characterized using (1) strain gage methods by us, and (2) ultrasonic phase spectroscopy methods by others[19] to estimate the relationships between the indentation-induced modulus and the in-plane and out-of-plane Young's moduli of the pyrolytic carbon materials.

We constructed 2D axisymmetric models to investigate the effects of anisotropy on the indentation load-displacement curves obtained by indenting normal to the plane of isotropy of a transversely isotropic medium. Both the experimental nanoindentation estimates and the FE predictions of the out-of-plane indentation modulus of the bulk PyroC samples were compared with the analytical approximations of an expected indentation modulus derived by Delafargue and Ulm[32] for transversely isotropic materials. FE modeling was also used to answer the questions concerning with the effects of the indenter shapes on the indentation modulus estimates.

In addition, we performed nanoindentation studies on three C/C composite samples infiltrated at different pressures, namely at 10, 20, and 30 kPa. We were able to estimate the effects of the infiltration pressure on the microstructure and elastic properties of the pyrolytic carbon by measuring the indentation modulus and the extinction angles of the PyroC matrix as a function of distance from the fiber and to correlate the optical and structural anisotropy of the pyrolytic carbon layers.

Lastly, we examined the possible mechanisms of failure of the pyrolytic carbon layers subjected to indentation normal and transverse to the plane of isotropy. We utilized indentation load-displacement curves and observations using SEM and PLM to make an assessment of what might have caused the permanent damage in certain cases of micro- and nanoindentation measurements.

CHAPTER 2

EXPERIMENTAL METHODS AND MODELING

Indentation

The Fundamentals of Indentation

Indentation is an experimental technique used to measure mechanical properties such as elastic modulus, hardness, friction coefficient, fracture toughness, and other important parameters. Indentation has been practiced for over a century ever since Heinrich Hertz made the pioneering contribution to the contact mechanics between two elastic bodies[33]. Over the decades, the focus of material sciences shifted to smaller and smaller scales which, in turn, encouraged the development of more sophisticated devices capable of measuring the above mentioned properties on micro- and, finally, on sub-micron length scales. In the 1980's, the nanoindentation entered the stage with the ability to measure the near-surface elastic properties of the variety of different materials and thin films.

A simple schematic of an indenter is shown in Figure 8 (a). An indenter of a specific geometry penetrates into the sample while the load and displacement are simultaneously recorded versus time.

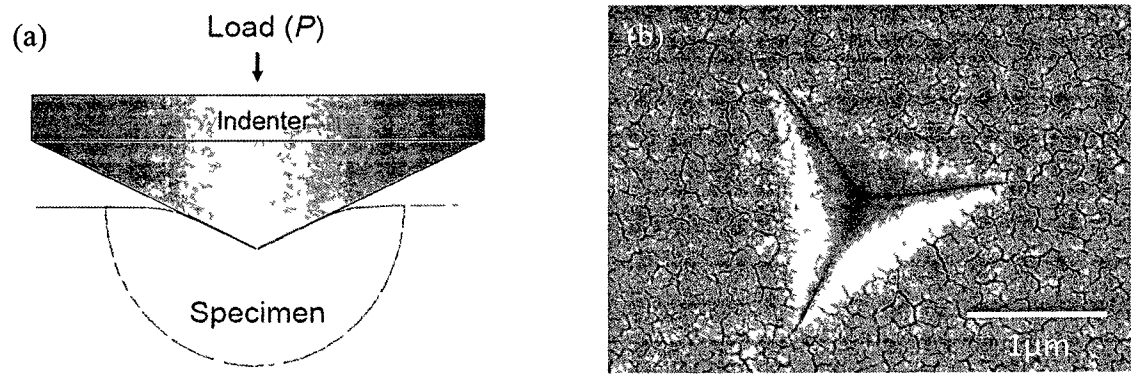

Figure 8: (a) Schematic of an indenter penetrating into a specimen and (b) a typical residual impression on the surface of a specimen upon indenter withdrawal.

If the indenter causes the permanent deformation of the material, the residual impression of the indent will remain on the surface of the specimen as shown in Figure 8 (b). The shape of the impression depicts the shape of the indenter and is often accompanied by either the material pile-up or material sink-in along the perimeter of an indent.

Although the working principles of the commercially available nanoindenters vary from system to system, the setup we used was developed by Hysitron TriboScope® which utilizes a three-plate capacitive force-displacement transducer. A schematic of the transducer is shown in Figure 9. This set-up provides high sensitivity, large dynamic range, and a linear force or displacement output signal.

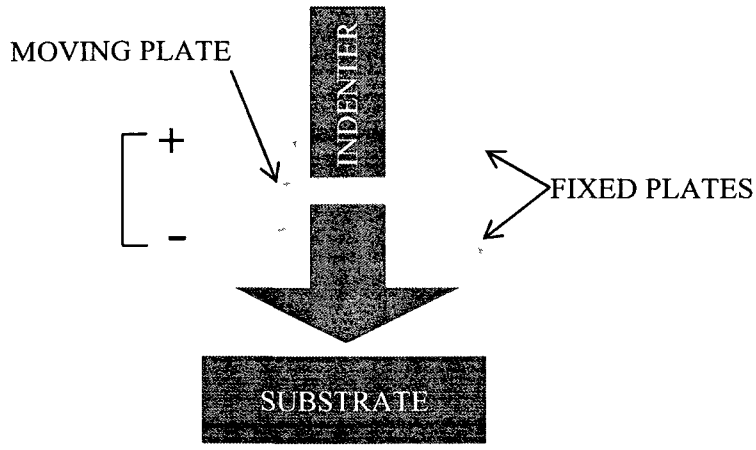

Figure 9: Schematic of the three-plate capacitive force-displacement transducer.

When two AC signals 180° out-of-phase with each other are applied at two fixed outer parallel plates, it creates a strong electric field potential that changes linearly between the plates. Since the signals are equal in magnitude but opposite in polarity, the electric field potential is maximized and is equal to the applied signal at the outer plates. However, the electric field potential at the center (i.e. in between two outer plates) is equal to zero because two opposite polarity signals cancel each other out. This enables the center plate to float in between two outer plates.

To activate the indenter, a DC signal is applied at the lower plate of the transducer which creates an electrostatic attractive force that pulls the center plate down. The displacement is deduced from the capacitance measurement via AC signal. The transducer records both the DC and AC signals simultaneously as a function of time. The DC and AC voltages have linear relationships with the load and displacement respectively; thus producing the raw data in the form of load versus time and displacement versus time. Since both the load and displacement are recorded against time, one can plot load versus displacement for further analysis.

Although the load-displacement curves may look different for different materials, the curve presented in Figure 10 represents an indent which caused a substantial amount of permanent deformation. Most of the analytical schemes developed to extract the elastic properties from the load-displacement curves targeted the materials that exhibited this behavior.

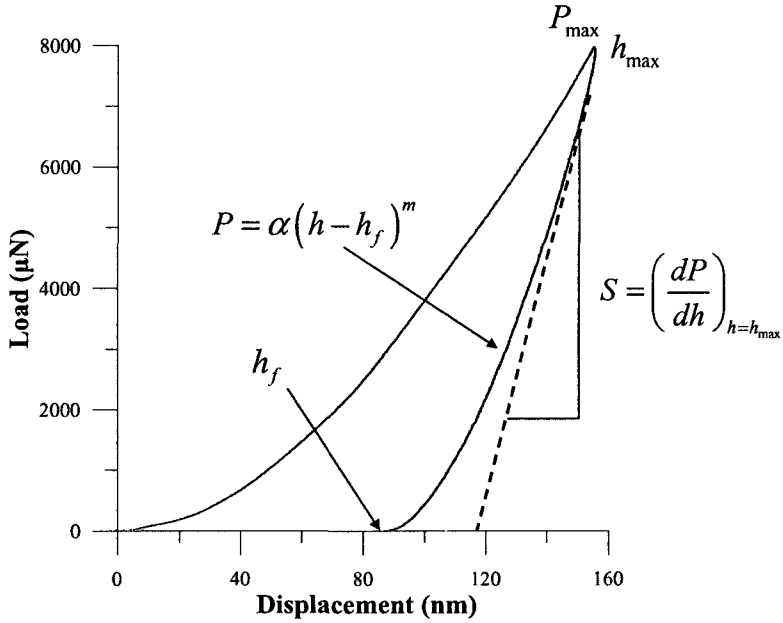

Figure 10: Typical load-displacement curve.

The load-displacement curves are typically analyzed using some variation of the method described by Oliver and Pharr[26] to determine the reduced elastic modulus and hardness. They estimate the modulus using the slope of the unloading curve at maximum displacement, $S=dP/dh$, where P is the applied load, h is the displacement, and $A(h_c)$ is the contact area function calibrated for each tip on isotropic material with known properties. The contact depth h_c is the actual depth of penetration into the sample not including the elastic deformation of the sample or the indenter system:

$$h_c = h_{max} - \varepsilon \cdot \frac{P_{max}}{S} \quad (1)$$

with the suggested value of ε of 0.72 for conical indenters and 0.75 for paraboloids of revolution (spherical indenters). The contact depth is used in the tip area function, $A(h_c)$, to estimate the reduced Young's modulus, E_r, using;

$$E_r = \frac{S \cdot \sqrt{\pi}}{2 \cdot \sqrt{A(h_c)}} \tag{2}$$

The tip area function, $A(h_c)$, is an estimate of an area of contact between a tip and a substrate as a function of depth. The Oliver and Pharr method was validated by comparing scanning electron microscope images of plastic indentations with the fit of the area function on fused quartz and several other materials that exhibit elasto-plastic deformation that is homogeneous on the scale of the indentation. The applicability of this method to estimate the contact area when indenting into a pyrolytic carbon material needs to be examined since these materials exhibit an elastic response. To the best of our knowledge, there is currently no method to estimate the area of contact for a purely elastic contact and the $A(h_c)$ estimated from the software packages included with most commercial nanoindenters is likely to be an overestimate the area of contact.

Equation 2 is used to estimate the value of the reduced Young's modulus for isotropic materials. The relationship between the reduced elastic modulus, E_r, and the actual Young's modulus of a specimen, E, is described by the following expression:

$$\frac{1}{E_r} = \frac{1-\upsilon^2}{E} + \frac{1-\upsilon_i^2}{E_i} \tag{3}$$

where E_i and ν_i are the Young's modulus and the Poisson's ratio of an indenter, and ν is the Poisson's ratio of a specimen. If $E_i >> E$ then the value of the reduced Young's modulus is practically equal to the value of the actual Young's modulus of the material.

When Equation 2 is used for anisotropic materials, it provides an estimate of the indentation modulus which is an average (or an apparent) modulus sampled by an

indenter in the direction of indentation. The strategies to estimate the relationships between the indentation modulus and the anisotropic elastic constants are being developed, both in implicit[34,35] and in explicit[32] forms, and this dependence will be addressed in this thesis.

Indentation Modulus Predictions

Several research groups in the past attempted to establish the link between the indentation modulus and the elastic properties of a general anisotropic material. Vlassak and Nix[34] noted that the indentation modulus is different from the Young's modulus in the direction of indentation and the difference depends on the degree of anisotropy of a given material. They concluded that the indentation modulus is rather approximated by the weighted average of the elastic constants. The mathematically implicit solution schemes by Vlassak and Nix[34] for triangular indenters and by Swadener and Pharr[35] for conical and parabolic indenters are difficult to implement and require a numerical solution of the equations for particular cases.

Delafargue and Ulm[32] proposed explicit approximations for the indentation moduli of a transversely isotropic medium under a rigid conical indentation in three principal material symmetry directions with an assumed pressure distribution. The orientation of the plane of isotropy relative to the coordinate system is shown in Figure 11[32]. The coordinate system chosen by Delafargue and Ulm[32] deviates from ours as they chose the direction 3 to be the direction along the axis of symmetry (direction 1 in our cases). This difference was taken into account to produce the consistent results.

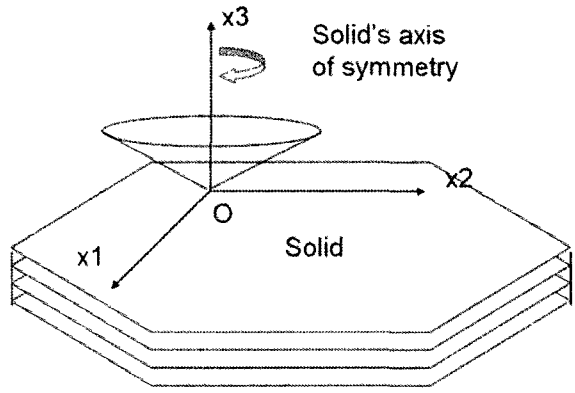

Figure 11: Schematic[32] of indentation in the solid's axis of symmetry.

The approximation of an indentation modulus, M_1 (=M_2), normal to the axis of symmetry was given in the following form:

$$M_1 = \sqrt{M_{12} M_{13}} \tag{4}$$

where M_{13} appears to be the indentation modulus obtained by indenting into an isotropic solid and given by:

$$M_{13} = \frac{C_{11}^2 - C_{12}^2}{C_{11}} \tag{5}$$

and M_{12} is the indentation modulus in the direction along the solid's axis of symmetry and given by:

$$M_{12} = M_3 \sqrt{\frac{C_{11}}{C_{33}}} \tag{6}$$

Constants C with various subscripts represent the components of the stiffness tensor of a transversely isotropic material. The indentation modulus in the direction along the solid's axis of symmetry, M_3, was based on Elliot-Hanson solution[36,37] and simplifies to the following form:

$$M_3 = 2\sqrt{\frac{C_{31}^2 - C_{13}^2}{C_{11}} \left(\frac{1}{C_{44}} + \frac{2}{C_{31} + C_{13}} \right)^{-1}} \tag{7}$$

These approximations of the indentation moduli greatly enhance their utility in their explicit forms. However, they only work when a set of elastic constants is known.

They cannot be used to determine the elastic properties of a transversely isotropic material from the indentation data alone.

Nanoindentation

The nanoindentation was performed using a Hysitron TriboScope® nanoindenter. The Hysitron® three-plate capacitive force/displacement transducer was attached to Veeco® Dimension SPM. This combination provided us with the ability not just to perform nanoindentation tests, but also to scan the indentation site with the indenter tip using the SPM mode before and after an indentation to distinguish the deformation from any other irregularities in the sample. The range of the applied loads of this instrument is 25 μN to 15mN with the load resolution of less than 1 nN and displacement resolution of about 0.0004 nm. Nanoindentation was carried out on the samples of the bulk pyrolytic carbon as well as on the carbon-carbon composite samples. Depending on the applied load and the indenter tip, the displacement range of nanoindentation experiments was 50-1000 nm with most indents being in 100-350 nm range. The schematics of the cube corner, Berkovich, and cono-spherical (60° included angle, 3 μm radius) indenters used in nanoindentation experiments are shown in Figure 12 (a-d). All three tips are made of diamond with the Young's modulus of about 1 TPa.

Figure 12: Schematic of the (a) cube corner, (b) Berkovich, (c) cono-spherical tips used in nanoindentation and the (d) Vickers tip used in microindentation. Retrieved on June 17, 2011 from <http://www.home.agilent.com/upload/cmc_upload/ck/zz-other/images/TipSummaryChart.a.jpg>.

Both the cube corner tip and the Berkovich tip are made in the shape of a three-sided pyramid. The included angles, which are twice the half angles shown in the images above, are 142.3° for the Berkovich tip and 90° for the cube corner tip. Both of these indenters had a 200 nm radius of curvature. The cono-spherical tip had the smallest included angle out of three indenters used for nanoindentation (60°); however, it had a large 3 μm radius of curvature. Radii of curvature for all three indenter tips were estimated by Imagemet® software's (Version 8.0) implementation of the blind tip reconstruction method on SPM images obtained by each indenter. The radius of curvature for the cono-spherical tip was also measured to be 3 μm by SEM. All three indenters were calibrated on the sample of a fused quartz for which the material properties were known. Our estimates of the indentation modulus utilized methods based on the Oliver and Pharr method[26] as implemented by Hysitron's Triboscope software version 8.0.

Microindentation

The microindentation measurements were performed on a FisherScope® H100C dynamic microindenter. The instrument was equipped with the optical microscope and the indenter head. The optical microscope allowed the user to observe the surface of a specimen to navigate to the desired location of indentation. The load range of the instrument was 0.4-1000 mN with the load resolution of 0.2 μN. Microindentation was performed on several different types of the pyrolytic carbon materials. The Vickers indenter tip was used throughout all experiments and its schematic is shown in Figure 12 (d). A Vickers indenter is made in a shape of a square pyramid with the included angle

of 138°. The tip was calibrated on a sample of steel with known material properties. The penetration depth ranged from 2-8 μm.

Sample Preparation

Pyrolytic Carbon

For our studies, small straight sections of the material were cut from the bulk PyroC disk using a Buehler Isomet low speed saw and glued to 15 mm diameter steel AFM discs. The samples were mounted so that the surface was either parallel or transverse to the deposition direction. The prepared samples were initially polished using 15 μm and 9 μm diamond lapping films with water as a lubricant. They were then polished with 5 μm alumina followed by a final polish with 0.02 μm colloidal silica suspension. The average surface roughness was measured to be 10 nm for transverse sections and 40 nm for the deposition plane by scanning the surface using a nanoindenter tip. This material was used for micro- and nanoindentation, strain gage measurements by us, and for ultrasonic phase spectroscopy measurements[19] by others.

We also performed microindentation on two additional carbon samples microstructurally similar to the bulk PyroC. One of them is pyrolytic graphite and the other one is glassy carbon, both prepared by others. The pyrolytic graphite and bulk PyroC samples were classified as high-texture, but the glassy carbon sample was isotropic.

Carbon-Carbon Composites

Carbon-carbon composite specimens provided to us for the nanoindentation testing were infiltrated in the facilities of Karlsruhe Institute of Technology in Germany. They supplied three (3) specimens with the dimensions of about 58mm x 48mm x 9mm each as shown in Figure 13 (a) manufactured at different pressures of 10 kPa, 20 kPa, or 30 kPa and at the constant temperature of 1100°C.

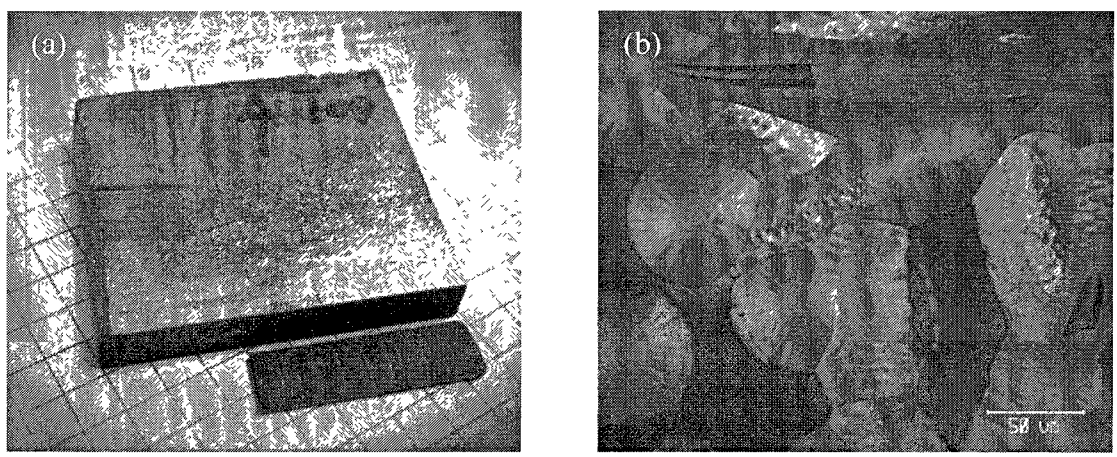

Figure 13: (a) Image of one of the C/C composite specimens showing its overall dimensions and the "bottom" section used for nanoindentation testing. (b) Typical microstructure of C/C composites showing the carbon fibers surrounded by the pyrolytic carbon matrix.

The specimens of the carbon-carbon composites were marked indicating their orientation in the reaction chamber during the pyrolysis. We cut small sections as shown in Figure 13 (a) using a Buehler Isomet low speed saw from the "bottom" part of the specimens. A sample had to fit on a 15 mm diameter steel AFM disk, so the average size of the prepared samples was on the order of 12 mm x 9 mm x 2mm. The sample preparation process was nearly identical to the one described for the bulk PyroC samples. The C/C composite samples were initially ground using a 400 grit abrasive paper followed by 15 μm, 9 μm, and 6 μm diamond lapping films and 5 μm alumina

suspension as the intermediate polishing steps. Finally, the mirror-like finish was achieved using 0.02 μm colloidal silica to reveal the microstructure shown in Figure 13 (b).

Strain Gage Measurements

We also utilized conventional strain gage methods to measure the elastic properties of the bulk pyrolytic carbon on the macro-scale. The majority of this work was performed by Khanh Nguyen and by Michael Buck, the undergraduate students who helped with the research. We used an Instron® model 1350 instrument with Futek® LSB303 200 pound load cell in displacement control to obtain the stress-strain curves for the bulk PyroC samples loaded in uniaxial tension and in uniaxial compression in the directions both normal and transverse to the plane of isotropy.

The set-up of the in-plane tension test is shown in Figure 14 (a). The tensile specimen was about 20 mm long with the cross-section of approximately 2 mm by 1.5 mm. This experiment required a use of the custom-made grips to clamp the sample.

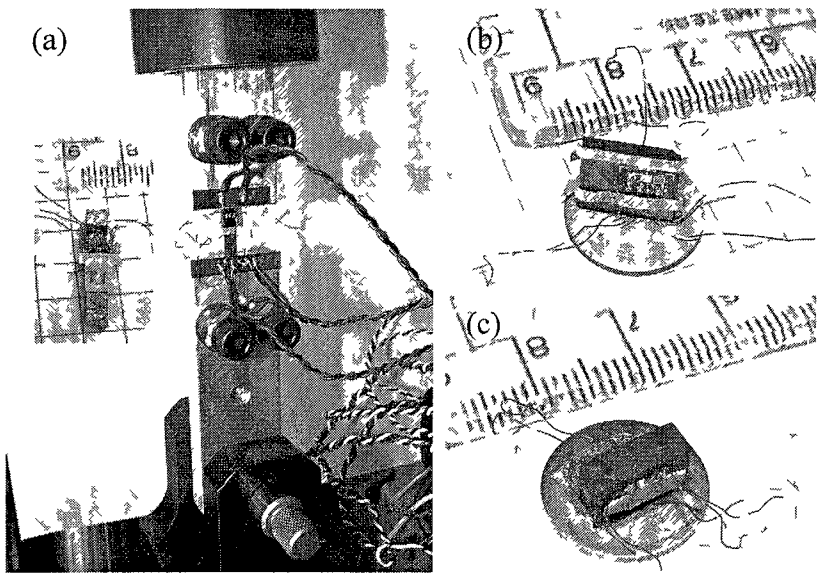

Figure 14: (a) The bulk PyroC sample mounted in the custom made grips for the uniaxial in-plane tension test, (b) the uniaxial in-plane compression test sample, and (c) the uniaxial out-of-plane compression test sample.

The dimensions of the in-plane compression sample were approximately 10 mm wide, 1.5 mm thick, and 5 mm high as shown in Figure 14 (b). The out-of-plane compression sample consisted of three 1.5 mm thick layers of the material glued together with the section of about 10 mm by 3 mm and is shown in Figure 14 (c). The samples for the in-plane and for the out-of-plane compression tests were glued to AFM steel disks and placed in between two parallel plates.

The 120 ohm strain gages were connected to quarter bridges composed of 0.01% precision resistors with a short, two wire connection. Two strain gages that measured the axial strain were mounted on the opposing sides of a sample to ensure that there was no significant torsion and/or bending present on the sample. Also, each sample had a single strain gage that measured the lateral strain.

The specimens were loaded to stresses of 10-20 MPa and referenced to the zero load state before and after loading. The excitation signal and the bridge imbalance were

recorded at a 100 Hz rate for all three bridges along with the load cell output from the 200 lb load cell.

The in-plane and out-of-plane Young's moduli of the bulk PyroC samples were determined using the Hooke's Law:

$$E = \frac{\sigma}{\varepsilon} = \frac{P/A}{\Delta l / l_0} = \frac{Pl_0}{xy\Delta l} \tag{8}$$

We also estimated the lumped uncertainty of the modulus measurements using the uncertainties of the individual parameters as shown in the following expression:

$$dE = \sqrt{\left(\frac{l_0}{xy\Delta l}dP\right)^2 + \left(\frac{P}{xy\Delta l}dl_0\right)^2 + \left(\frac{-Pl_0}{x^2 y\Delta l}dx\right)^2 + \ldots} \sqrt{\ldots + \left(\frac{-Pl_0}{xy^2\Delta l}dy\right)^2 + \left(\frac{-Pl_0}{xy\Delta l^2}d\Delta l\right)^2} \tag{9}$$

The uncertainty of the load P was approximately 0.01% of the applied load, roughly about 0.01-0.02 N. The uncertainty in the measurements of the specimen dimensions were on the order of 25 μm. The bridge imbalance was measured directly with 0.5 μV resolution which corresponds to a strain resolution of ~2e-6. Thus, the lumped uncertainty of the modulus was calculated to be about 0.1%.

However, the uncertainty of the modulus measurement, including variations in alignment that caused a small bending moment on every measurement, is on the order of 1-2%. The modulus was computed from the average slope obtained from the gages on the opposing faces of the specimen. The Poisson's ratio was calculated from the ratio of strains of the gages on the same face of the specimen and is therefore unaffected by the small bending moment.

Two Dimensional Finite Element Modeling

We used commercial software Marc Mentat by the MSC software corporation to construct two-dimensional (2D) finite element models to answer the following questions:

1). What are the effects of anisotropy on the relationships between the indentation modulus and the actual Young's modulus of a substrate in the direction of indentation,

2). How does the tip geometry impact the indentation modulus when indenting into a transversely isotropic material,

3). What are the axial and transverse stresses relative to the indentation axis for the cube corner, Berkovich, and cono-spherical tips and how do they impact the ability of these indenters to cause bucking of the graphene planes when indenting parallel to the plane of isotropy of the pyrolytic carbon.

We used 2D axisymmetric finite element models to answer the posed questions. All models were contact problems involving a rigid tip and a deformable substrate. These models were intended for the indentations normal to the plane of isotropy in which the material properties are the same. We realize that axisymmetric models are not appropriate for the indentations transverse to the plane of isotropy because the material properties in two directions lateral to the direction of indentation are not isotropic. However, the results still provide some insight into the material's behavior. One would need to construct a full 3D model to gain a better understanding of the response of a transversely isotropic material indenting parallel to the plane of isotropy.

FE Modeling Procedures

Dimensions and Geometry

The choice of the dimensions of both the substrate and the indenter was very crucial. The conventional procedure of deriving the elastic properties from the indentation load-displacement curves proposed by Oliver and Pharr[26] is based on Sneddon's solution[24] for linearly elastic solids which makes the following assumptions: (1) the specimen is an infinite half-space, (2) the tip has a perfect geometry (i.e. perfect cone, pyramid, etc.) and is infinitely sharp, and (3) material is linearly elastic and incompressible. All of these assumptions need to be carefully addressed in order to conduct meaningful finite element studies.

It is impossible to construct a finite element model of an infinitely large half-space. However, it is possible to create a substrate sufficiently large so that its solution will converge and the error associated with the finite dimensions of the substrate can be neglected. Appendix B provides details on how the size of the substrate was selected.

A typical FE mesh used for 2D axisymmetric modeling is shown in Figure 15. The size of the substrate varied based on the desired indentation depth. The substrate size and the element size were optimized to achieve the convergence with the least amount of elements. The optimal substrate size was determined to be about 30-50 times the indentation depth with the size of the finest elements of about 30-35 nm measured diagonally.

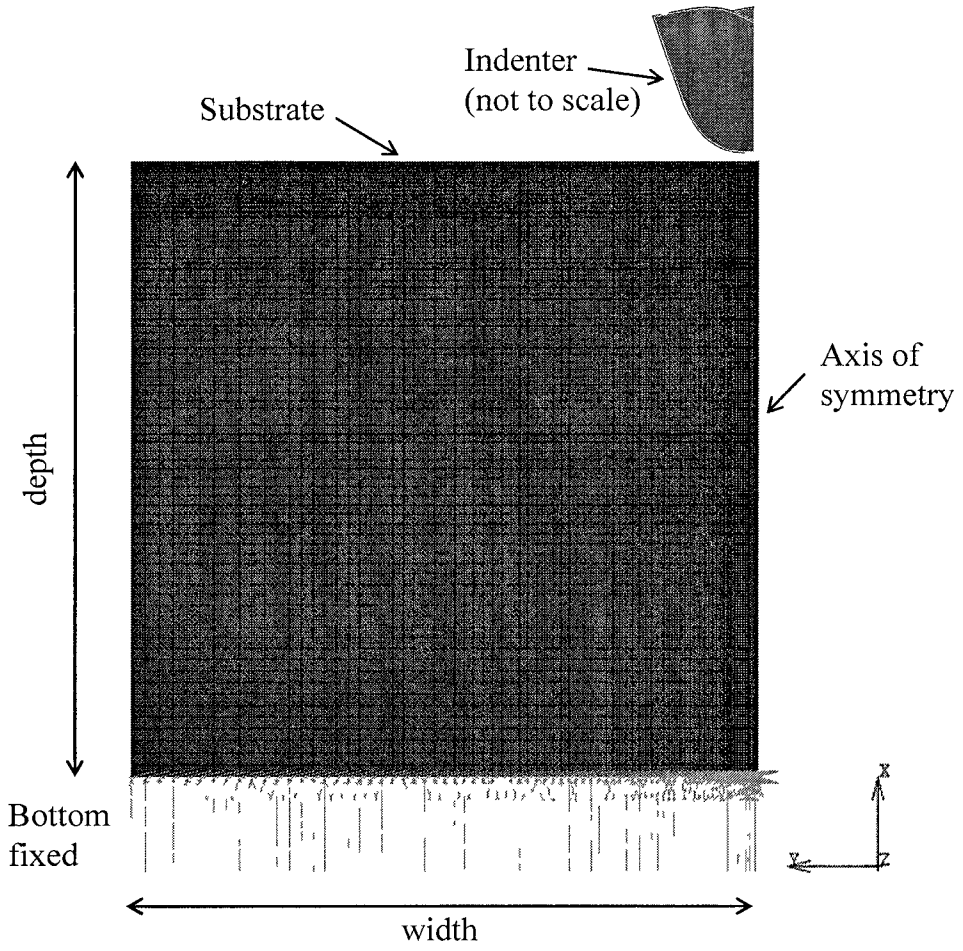

Figure 15: FE mesh used for 2D axisymmetric modeling. The size of the quadrilateral elements varies linearly from the lower left (188 nm) to the upper right (36 nm). Rigid indenter is drawn not to scale for visual purposes (the actual size is much smaller). Nodes at the bottom of the substrate are fixed in all directions.

The number of the quadrilateral elements varied based on the dimensions of the entire substrate but most models had about 6400 elements. A bias factor was applied in the construction of the mesh to maintain the fine meshing in the vicinity of the contact between the indenter and the substrate and the coarser meshing further away from it. This dramatically reduced the amount of elements and saved a tremendous amount of computational time and resources. The finest and the coarsest elements were about 36 nm and 188 nm respectively measured diagonally. Only the elements in direct contact

with the indenter were assigned to be deformable contact elements. The rest of the elements were not assigned any contact properties. We assumed zero friction and no plasticity. We experimentally determined that the pyrolytic carbon tends to deform elastically when subjected to indentation so the use of the linear elastic elements was appropriate.

The indenter was modeled as a rigid body with a constant penetration velocity of 1 nm per time step (in some cases 2 nm/time step). The assumption of a rigid tip was accurate considering that the Young's modulus of a diamond indenter (1 TPa) is about two orders of magnitude higher than the Young's modulus of most pyrolytic graphite materials.

We considered three different indenter geometries corresponding to the respective geometries of the cube corner, Berkovich, and cono-spherical tips used in the nanoindentation experiments. The asymmetric indenter tips (i.e. cube corner tip and Berkovich tip) were modeled as effective cones with certain effective cone angles that gave them the same area to depth relationship as the pyramidal indenter in question[34].

The cube corner and Berkovich indenters were constructed using two curves – an arc with the radius of 200 nm and a line tangent to the arc with the effective cone angle of 42.28° and 70.3° for cube corner and Berkovich tips respectively. The cono-spherical tip was modeled as an arc with the 3μm radius of curvature. The indenter geometries shown in Figure 16 (a-c) are the most accurate 2D axisymmetric representations of the physical indenters used in nanoindentation.

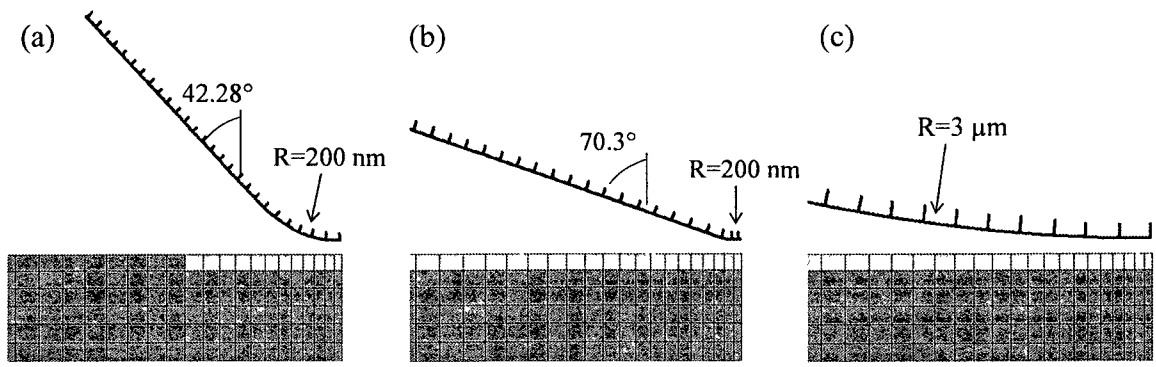

Figure 16: FE representation of the (a) cube corner, (b) Berkovich, and (c) cono-spherical indenters.

Boundary Conditions and Material Properties

The boundary conditions for all the models were the same. The axis of symmetry for the 2D axisymmetric models was chosen along the axis of indentation (the right-hand edge of the substrate in Figure 15). The symmetry line (not shown) was constructed to assign that boundary condition. Additionally, the bottom nodes of the substrate were fixed in X, Y, and Z directions. We experimented with restricting the displacement in the Y-direction of the left-hand side of the substrate (the opposite side of the axis of symmetry edge), but it did not affect the results so it was left out.

We considered various cases of the material properties assigned to the substrate to answer the questions posed earlier. Initially, we considered the simplest case when the substrate was modeled as an isotropic elastic solid. This model was used for validation (see Appendix A) and for comparison with other models which had transversely isotropic properties assigned to them. The Young's modulus of 10 GPa and the Poisson's ratio of 0.3 were selected arbitrarily as reasonable values at the initial stages of the FE modeling.

After the model was validated, we started varying the material properties to obtain an insight on how the anisotropy affects the load-displacement curves and, ultimately, the indentation modulus. We assigned the transversely isotropic properties to the substrate with the in-plane Young's modulus being 10, 5, 2, 0.5, 0.2, and 0.1 times the value of the out-of-plane Young's modulus which was again selected to be 10 GPa. The other three independent elastic constants were the in-plane Poisson's ratio (was set to 0.3), and the out-of-plane Poisson's ratio and shear modulus (both varied, based on the ratio of in-plane/out-of-plane Young's modulus – see Equation 11). More details on the property selection for transversely isotropic models are forthcoming. For this study, we utilized the model with the cube corner rigid tip penetrating 125 nm into the substrate.

At the later stages of the FE studies, we utilized the experimentally measured elastic constants for the bulk pyrolytic carbon using strain gages and compared the resulting indentation moduli with the predicted indentation moduli obtained by Delafargue und Ulm[32] approximations as well as with experimentally determined indentation moduli by micro- and nanoindentation measurements. We used the respective geometries of the cube corner, Berkovich, and the cono-spherical indenters presented in the previous section for these FE models in order to simulate nanoindentation experiments as closely as possible.

Loadcases

The loadcases for all the models were mechanical static with a constant time step. The rigid tip was controlled by the velocity of the penetration. For most cases, the velocity was set to 1 nm per time step. The loadcase time and the number of steps were set to the same number providing with the displacement increment of 1nm per time step.

For two cases, when Berkovich and the cono-spherical indenters were set to displace 400 nm and 600 nm respectively, the velocity was at 2 nm per time step, doubling up the depth of penetration over the loadcase time.

Guidelines for the Selection of the Transversely Isotropic Material Properties

For the FEA results to be meaningful, the appropriate elastic constants had to be prescribed to the finite element mesh. The following guidelines need to be followed to satisfy the requirements of the transverse isotropy.

Pyrolytic carbon exhibits the transverse isotropy with the same properties in the deposition plane (in-plane, directions 2 and 3) as shown in Figure 17. The properties in the deposition direction (out-of-plane, direction 1) are different. Material property selection began by assigning certain values to the independent variables of a compliance tensor for a transversely isotropic material, namely the out-of-plane Young's modulus E_1, the in-plane Young's modulus E_2 (= E_3), the in-plane Poisson's ration v_{23} (= v_{32}), and the out-of-plane Poisson's ratio v_{21} (=v_{31}). The compliance tensor S for a transversely isotropic material is as follows:

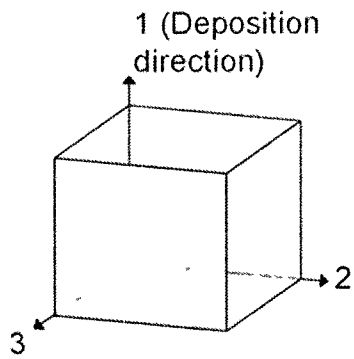

Figure 17: Coordinate system correlation to deposition direction

$$S = \begin{pmatrix} \frac{1}{E_1} & \frac{-\nu_{21}}{E_2} & \frac{-\nu_{31}}{E_3} & 0 & 0 & 0 \\ \frac{-\nu_{12}}{E_1} & \frac{1}{E_2} & \frac{-\nu_{32}}{E_3} & 0 & 0 & 0 \\ \frac{-\nu_{13}}{E_1} & \frac{-\nu_{23}}{E_2} & \frac{1}{E_3} & 0 & 0 & 0 \\ 0 & 0 & 0 & G_{23} & 0 & 0 \\ 0 & 0 & 0 & 0 & G_{31} & 0 \\ 0 & 0 & 0 & 0 & 0 & G_{12} \end{pmatrix} \tag{10}$$

Following the symmetry of the compliance tensor, v_{12} (= v_{13}) can be found by the following expression:

$$\upsilon_{12} = \upsilon_{21} \cdot \frac{E_1}{E_2} \tag{11}$$

Once all Poisson's ratios were determined, the following condition for transversely isotropic materials had to be satisfied according to Kachanov et al[38]:

$$1 - \upsilon_{12}^2 > 0 \tag{12}$$

$$1 - \upsilon_{31}\upsilon_{13} > 0 \tag{13}$$

$$1 - 2\upsilon_{12}\upsilon_{13}\upsilon_{31} - \upsilon_{12}^2 - 2\upsilon_{13}\upsilon_{31} > 0 \tag{14}$$

If any of these conditions were not satisfied, the set of elastic properties did not meet the requirements of the transverse isotropy and the independent properties had to be changed. The in-plane shear modulus G_{23} was calculated by the following formula:

$$G_{23} = \frac{E_2}{2(1+\upsilon_{23})} \tag{15}$$

The out-of-plane shear modulus G_{12} (=G_{31}) was approximated by Saint-Venant's relation[39] for hyperelastic transversely isotropic materials given in Cazacu[40]:

$$G_{12} = \frac{1}{E_1} + \frac{1}{E_2} + \frac{2\upsilon_{21}}{E_2} \tag{16}$$

This relation provides reasonable approximation of the out-of-plane shear modulus of a pyrolytic carbon material which also exhibits large elastic strains (i.e. hyperelastic) when subject to indentation. Over 200 quasi-static and dynamic tests performed on various transversely isotropic rocks by Worotnicki[41] support the validity of Saint-Venant's relation[39].

For the FEA studies of the transverse isotropy, when the ratio of the in-plane/out-of-plane modulus varied, the selection of the out-of-plane Poisson's ratio was a challenge. Considering that the difference between in-plane and out-of-plane moduli was one order of magnitude, the difference in Poisson's ratios was also of the same order between v_{21} (= v_{31}) and v_{12} (= v_{13}). So when initial Poisson's ratio selections were made, we made sure that the other pair of the Poisson's ratios does not get outrageously large (greater than 2) or outrageously low (less than 0.05). Finally, all the Poisson's ratio values were checked against restrictions on the transversely isotropic materials noted by Kachanov et al[38].

CHAPTER 3

RESULTS AND DISCUSSIONS

Strain Gage Measurements of the Bulk PyroC

Three different tests were performed on the bulk pyrolytic carbon including the in-plane tensile test as well as the in-plane and the out-of-plane compression tests. For the in-plane tensile test, the axial strain gages were attached to the opposing sides of the sample of the deposition plane, and the lateral strain gage was attached to one side of the deposition plane. The in-plane Young's modulus E_2 ($=E_3$) of the bulk PyroC in tension was found by extracting a linear slope of the fitting curve of the stress-strain data obtained by axial strain gages. The data chosen for the analysis exhibited the difference in slopes between the opposing axial strain gages of only 1-2%. This difference was largely due to bending or torsion moments exerted on the sample by a small misalignment of the load train. The Poisson's ratios v_{21} ($=v_{31}$) and v_{23} ($=v_{32}$) were calculated by dividing the measured lateral strains of the transverse plane and of the deposition plane respectively by the axial strain. For all the Poisson's ratio calculations, the ratio of the strains of the gages on the same face of a specimen were chosen and therefore were not affected by the small bending/torsion moment.

In a similar manner, other elastic constants of the bulk PyroC were found by the in-plane and out-of-plane compression tests. The in-plane compression test was used to

measure the in-plane Young's modulus E_2 (= E_3) in compression and Poisson's ratio v_{23} (=v_{32}). The out-of-plane compression test was used to measure the out-of-plane Young's modulus E_1 in compression and Poisson's ratio v_{12} (=v_{13}). The out-of-plane tension test was not conducted because of the size limitations of the given sample.

The stress-strain curves obtained by the in-plane tension and compression tests are superimposed in the plot of Figure 18. The most remarkable finding is the presence of the tension-compression anisotropy in the bulk pyrolytic carbon as documented by Gross et al[42]. The in-plane Young's modulus measured in tension (E_2,E_3=30.2 GPa) is significantly higher than if the sample was loaded in compression (E_2,E_3=18.8 GPa).

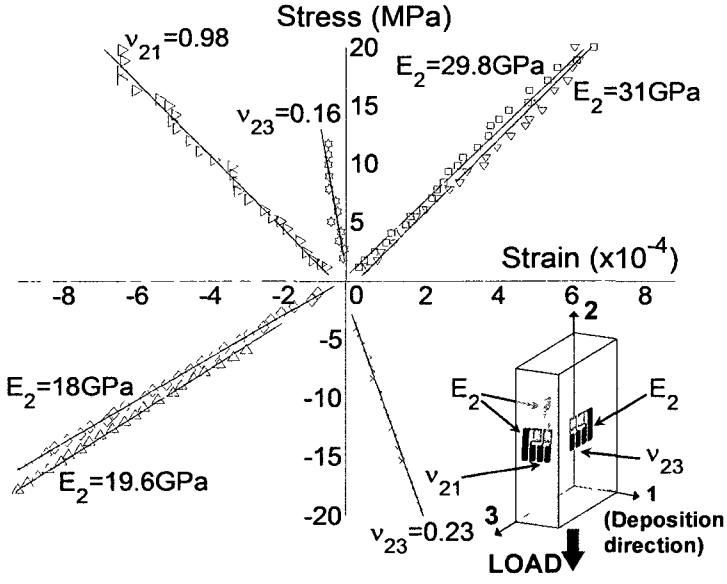

Figure 18: Stress-strain curves obtained by the in-plane tension and compression tests showing specimen orientation and location of strain gages for each elastic constant.

To the best of our knowledge, Gross et al[42] were the first to document the tension-compression anisotropy for the pyrolytic carbon. However, Oya and Johnson[43] reported on the tension-compression anisotropy in elastic modulus and the yield strength for PAN-

based fibers. They attributed this phenomenon to the presence of the needle-like pores along the longitudinal direction of the fibers.

As previously stated, bulk PyroC, or any pyrolytic carbon for this matter, exhibits a turbostratic structure that consists of roughly aligned graphene planes that are kinked and discontinuous within the domain-like regions. Therefore, one of the possible explanations for the presence of the tension-compression anisotropy is the buckling and puckering of the graphene planes when they are subjected to a compressive load as suggested by Riter[44]. Gross et al[42] point out that the kinks in the turbostratic structure of the PyroC may deform by bending in compression and yielding a lower modulus while straightening in tension resulting in a higher modulus. Also, there might be the disk-like voids that "buckle open" when loaded in compression.

The measured values of the Poisson's ratios that vary from 0.16 for v_{23} to 0.97 for v_{21} are reasonable and satisfy the restrictions on Poisson's ratios of the transversely isotropic materials. Also, the differences between the in-plane and out-of-plane Young's moduli and between the out-of-plane Poisson's ratios v_{12} (= v_{13}) and v_{21} (= v_{31}) are consistent with each other in terms of the elastic symmetry. The elastic constants determined from the linear regression of the stress-strain curves are summarized in Table 1.

Given that the analysis of ultrasonic measurements assumes tension-compression isotropy, the results obtained by the strain gage methods are believed to be the most accurate. They involved the standard uniaxial tension and compression tests used for decades on isotropic as well as on anisotropic materials. The strain gage methods were able to capture the tension-compression anisotropy of the PyroC.

	Tension	Compression	Ultrasonic[19]	Three point Bending[30]
E_1 (GPa)	-	5.2 ± 0.3	12.8	-
$E_2 = E_3$ (GPa)	30.2 ± 1.1	18.8 ± 0.7	27.1	17.5-20.5
$\nu_{12} = \nu_{13}$	-	0.35 ± 0.007	0.22	-
$\nu_{23} = \nu_{32}$	0.16 ± 0.03	0.22 ± 0.01	0.35	-
$\nu_{21} = \nu_{31}$	0.97 ± .04	-	0.47	-

Table 1: Elastic constants of the bulk PyroC measured by the strain gages showing the tension-compression anisotropy of the material.

The ultrasonic measurements by Gebert et al[19] produced the value of the in-plane Young's modulus (~27.1 GPa) somewhere in between the in-plane Young's moduli found in tension and in compression using the strain gage measurements. The elastic constants found by the ultrasonic tests were directly correlated with the velocity of the acoustic waves propagating through the sample and these waves were not capable of detecting the tension-compression anisotropy. The elastic constants estimated by the ultrasonic studies rather reflect an average or an apparent modulus in the direction of the applied ultrasonic pulse. The out-of-plane Young's modulus measured by ultrasonic studies (~12.8 GPa) yielded a value that is twice higher than what was measured by strain gage tests. It is worth noting that some elastic constants obtained by ultrasonic measurements, particularly C_{12} and C_{13}, had uncertainties of 17% and 46% respectively. The estimates of the Young's modulus by three point bending tests[30] were also based on tension-compression isotropy utilizing the standard linear elasticity solutions.

Indentation Measurements of the Bulk PyroC

Nanoindentation

Indenter Tips

Nanoindentation tests on the bulk pyrolytic carbon samples were performed using a cube corner tip and a Berkovich tip with an approximate radius of curvature of 200 nm for both. A cono-spherical tip with a radius of 3 μm was also utilized. Their respective SEM images are shown in Figure 19 (a-c).

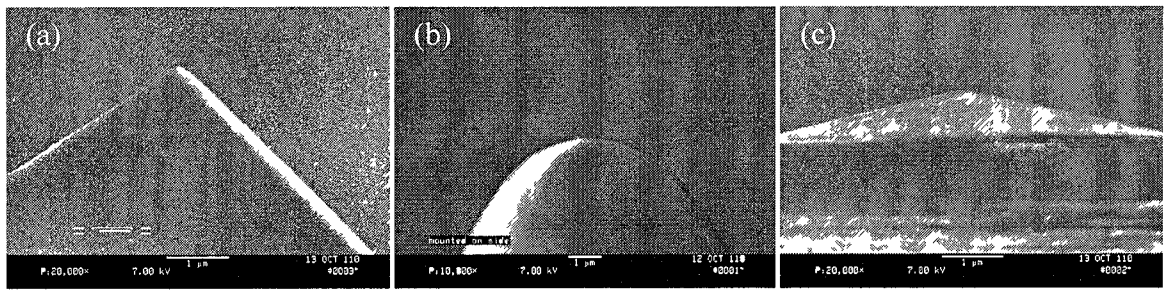

Figure 19: SEM images showing (a) cube corner tip with the included angle of 90° and 200 nm radius of curvature (b) cono-spherical tip with the 3 μm radius of curvature and (c) Berkovich tip with the included angle of 142.3° and 200 nm radius of curvature.

The cube corner tip was able to penetrate the most for a given load. The range of the applied loads used for the analysis was from 100 μN to 400 μN in the direction normal to the plane of isotropy (i.e. parallel to the deposition direction), and 40-3000 μN in the direction parallel to the plane of isotropy (i.e. transverse to the deposition direction). The corresponding penetration depths were 70-300 nm and 60-1,000 nm for indentation normal and parallel to the plane of isotropy of the PyroC respectively. The material exhibited mostly elastic behavior with distinct loading and unloading curves. In

some cases, the indenter left small residual impressions on the surface. The residual impression is shown in Figure 20.

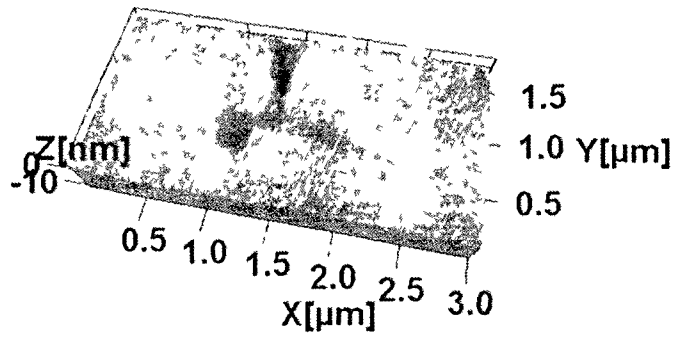

Figure 20: SPM scan of the area of the bulk PyroC sample which was indented in the deposition plane with a cube corner tip leaving residual imprints on the surface.

We observed load discontinuities at loads above 400-600 μN indenting normal to the plane of isotropy. Barsoum et al[45] attribute this phenomenon to the propagation of the kink bands as will be discussed in Chapter 5. These curves were not considered in the indentation modulus estimates.

Indentation performed with a cono-spherical tip yielded lower penetration depths than the cube corner indenter for a given load but higher than the Berkovich indenter. The range of the applied loads used for the analysis was from 470-4,000 μN in the direction normal to the plane of isotropy and 470-10,000 μN in the direction parallel to the plane of isotropy. The corresponding depth ranges were 120-540 nm and 130-1500 nm respectively. No discontinuities were observed up to the maximum load for indentations parallel to the plane of isotropy and there were no residual impressions on the surface. Discontinuities in the load-displacement curves and the material pile-ups were observed for the indents normal to the plane of isotropy at loads exceeding 5000 μN. Again, this phenomenon will be discussed in Chapter 5.

The Berkovich indenter penetrated the least for a given load. The range of the applied loads used for the analysis was 145-10,000 μN in the direction normal to the plane of isotropy, and 140-5,000 μN parallel to the plane of isotropy. The corresponding penetration depth ranges were 70-800 nm and 60-540 nm. No discontinuities in the load-penetration curves were observed for the Berkovich indenter tip for either orientation and there were no residual impressions.

Indentation Moduli Predictions

The elastic properties of the bulk pyrolytic carbon measured by the strain gage methods and by the ultrasonic phase spectroscopy methods[19] were used in conjunction with the Delafargue and Ulm explicit approximations[32] to estimate the expected indentation moduli. We assumed a shear modulus of 2.86 GPa which was not measured using the strain gage methods but was approximated by the Saint-Venant's relation[39] for a transversely isotropic material. The in-plane and the out-of-plane indentation moduli using the ultrasonic data were found to be 20.65 GPa and 9.59 GPa respectively. The strain gage data yielded similar results of 20.9 GPa for the in-plane indentation modulus and 9.6 GPa for the out-of-plane indentation modulus.

Nanoindentation Data

Figure 21 (a-b) shows the typical load-displacement curves of all three indenters at approximately 200 nm depth of penetration both normal and parallel to the plane of isotropy. All curves are nearly reversible with a substantial hysteresis which suggests that material exhibits some viscoelastic characteristics.

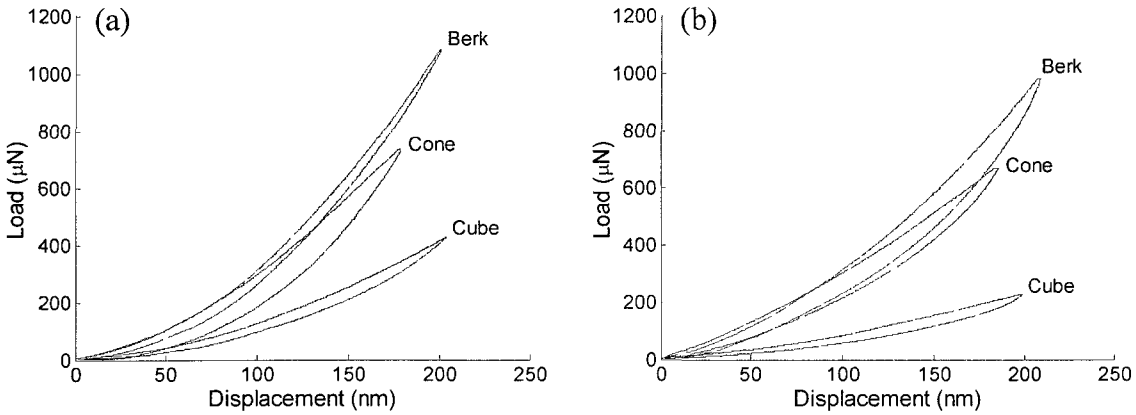

Figure 21: Nanoindentation load-displacement curves obtained using all three indenters at 200 nm displacement (a) normal to the plane of isotropy (b) parallel to the plane of isotropy.

Figure 22 (a-b) shows the indentation modulus estimates for all three indenters in the directions normal and parallel to the plane of isotropy.

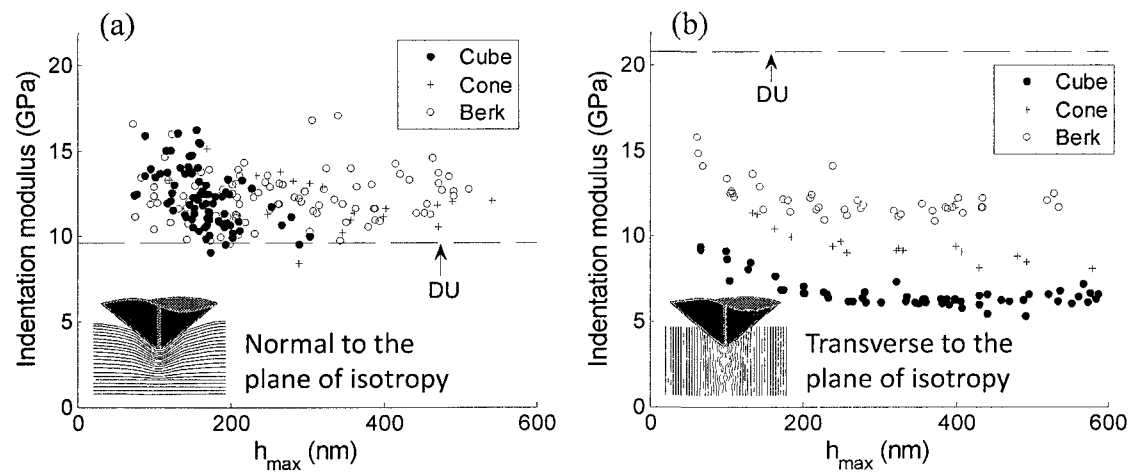

Figure 22: Indentation modulus estimates for the cube corner, Berkovich, and the cono-spherical tips in the direction (a) normal and (b) transverse to the plane of isotropy of the bulk PyroC. Dashed line indicates the indentation modulus prediction by Delafargue and Ulm[32] (DU).

In the indentation normal to the plane of isotropy, there is a large scatter of the indentation modulus which we attribute to the surface roughness measured to be approximately 40 nm using the indenter in the SPM mode. The indentation modulus

estimates appear to be relatively constants for all three indenters and above the prediction by the Delafargue and Ulm approximations[32] by about 27%.

In the indentation parallel to the plane of isotropy, all three indenters exhibit distinct indentation modulus values. These estimates are the highest for the Berkovich indenter and the lowest for the cube corner indenter and all are surprisingly lower than the predicted in-plane indentation modulus. Also, there is a pronounced trend of the indentation modulus drop with increasing displacement. Both of these observations will be discussed in detail further in this chapter.

Table 2 presents the estimates of the indentation modulus of the bulk PyroC from the nanoindentation load-displacement curves along with the values of the Young's modulus obtained by ultrasonic phase spectroscopy[19], by strain gage measurements, and by bending tests[30]. The uncertainty of the experimental data is given in terms of one standard deviation.

Test		E_1 (GPa)	$E_2=E_3$ (GPa)
Strain gage (tension) test		-	30.2±1.1
Strain gage (compression) test		5.2±0.3	18.8±0.7
Ultrasonic test		12.8	27.1
Bending test		-	18.5
		M_1 (GPa)	$M_2=M_3$ (GPa)
Nanoindentation	Cube Corner	12.21 ± 1.68	6.67 ± 0.79
	Cono-Spherical	12.09 ± 1.49	9.25 ± 0.89
	Berkovich	12.25 ± 1.45	12.19 ± 1.02
DU[32] Prediction	Strain gage	9.6	20.9
	Ultrasonic[19]	9.59	20.65

Table 2: Summary of the in- and out-of-plane Young's moduli, E_1 and E_2, obtained by strain gage, ultrasonic, and bending test methods and of the in- and out-of-plane indentation moduli, M_1 and M_2, obtained by nanoindentation and by Delafargue and Ulm approximations[32] based on strain gage and ultrasonic phase spectroscopy data[19].

The out-of-plane indentation modulus, M_1, estimated using Equation 2 was nearly the same for all three indenter tips. These estimates are about the same as the out-of-plane Young's modulus, E_1, measured by the ultrasonic phase spectroscopy. However, there is more than a factor of two difference between the in-plane indentation modulus and the in-plane Young's modulus obtained by strain gage methods. It is important to note that the indentation modulus and the Young's modulus of a material are not necessarily the same values, especially in a case of an anisotropic solid.

The in-plane indentation moduli, M_2 (=M_3), estimated using Equation 2 were distinctly different for each indenter and all of them were well below the predictions based on the ultrasonic phase spectroscopy measurements and the strain gage measurements. In spite of the fact that the in-plane modulus of the PyroC is expected to be higher than the out-of-plane modulus, the estimates of the in-plane indentation modulus from the cube corner and the cono-spherical indenters were less than the out-of-plane estimates. The difference between the in-plane and out-of-plane estimates of the indentation modulus obtained by the Berkovich indenter was within 1%.

Comparing indentation moduli predictions with the experimental estimates of the Young's moduli obtained by both methods, one may make an important observation. The in-plane Young's modulus measured by the strain gages (18.8 GPa in compression and 30.2 GPa in tension) and by the ultrasonic tests (27.1 GPa) are comparable to the values of the indentation modulus predicted using the explicit approximations by Delafargue and Ulm(~21 GPa). The out-of-plane estimates of the Young's modulus obtained by the strain gage methods (5.2 GPa in compression) and by the ultrasonic measurements (12.8 GPa) are lower than the in-plane values and so is the predicted out-

of-plane indentation modulus (~9.6 GPa). Therefore, one may conclude that the transverse properties of a material relative to the axis of indentation have a substantial impact on the indentation modulus predictions. We observe about 85% difference between the out-of-plane Young's modulus measured using the strain gages and the out-of-plane indentation modulus.

Microindentation

The layered structure of the pyrolytic carbon is observed on various length scales, from nanoscale to microscale as shown in the images presented in Figure 5 and in Figure 6. Since the typical nanoindentation depths are measured in the range of hundreds of nanometers, the use of microindentation, which operates in the range of tens of microns, could improve our understanding of how pyrolytic carbon material responds to indentation at different length scales and how the microstructure of the PyroC could impact the indentation modulus estimates. Therefore, microindentation was performed on various carbon-based materials at the facilities of KIT.

Indenter Tip

The Vickers indenter was used for all microindentation measurements. The schematic of a Vickers indenter is shown in Figure 12 (d). The tip was calibrated on a sample of steel with known properties. Vickers indenter is made in the shape of a four-sided pyramid with the included angle of 136° and with the same depth-to-area ratio as the Berkovich indenter. We did not determine the radius of curvature of the tip. However, according to the manufacturer who serviced the instrument on quarterly basis, the radius of curvature of the Vickers indenter could not exceed 500 nm.

Microindentation Data of the Bulk PyroC

Five microindentation tests (three of them are shown in Figure 23 (a-b) below) were performed parallel and five test transverse to the plane of isotropy of the same bulk PyroC sample studied by nanoindentation. The applied loads were 150, 300, 600, 800, and 1000 mN. The penetration depths ranged from 2 μm to 8 μm. All the tests produced consistent data.

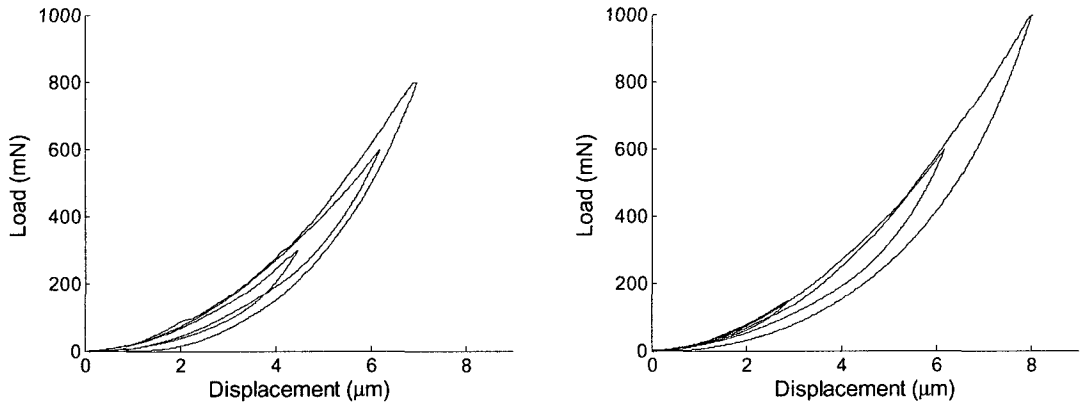

Figure 23: Microindentation load-displacement curves of the bulk PyroC obtained using Vickers indenter (a) normal to the plane of isotropy (b) parallel to the plane of isotropy.

The loading and the unloading curves exhibited nearly the same elastic behavior as for nanoindentation with similar hysteresis. The indentation moduli in the directions normal and parallel to the plane of isotropy were estimated to be 10.0±0.32 GPa and 9.97±0.2 GPa respectively, using Equation 2. Both the in- and out-of-plane indentation moduli estimates obtained by the Berkovich indenter were also close (~12 GPa). The similarity of these results is not surprising considering that both indenters are blunt with similar included angles and the same depth-to-area ratios, in spite of the Vickers indenter being a four-sided pyramid tip and the Berkovich tip having a three-side pyramid configuration. Both of these two indenters produced the estimates of the in-plane and

out-of-plane indentation moduli with only about 20% difference in values. This difference may be attributed to two different length scales on which these experiments were carried out and to slight differences in the respective geometries of the Vickers and the Berkovich indenters.

Microindentation Data of Other Carbon-Based Materials

In addition to testing the bulk PyroC samples, the microindentor was also used on another pyrolytic graphite and on glassy carbon samples. The microstructure of the pyrolytic graphite sample shown in Figure 24 exhibits the same columnar features that exist throughout the entire cross-section of the bulk PyroC as observed in the PLM image presented in Figure 5 (a).

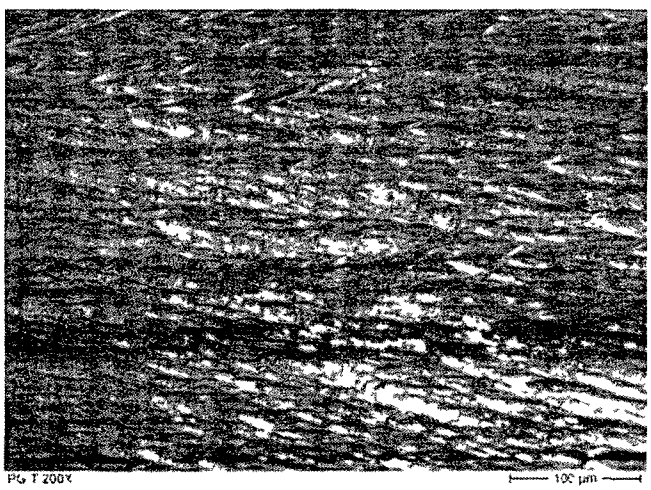

Figure 24: PLM image of the pyrolytic graphite sample in cross-section showing columnar features.

The load-displacement curves of the pyrolytic graphite sample shown in Figure 25 (a-b) are also very similar to the ones obtained for the bulk PyroC samples. However, more hysteresis is observed for the pyrolytic graphite material than for the bulk PyroC shown in Figure 23 (a-b). The in-plane and out-of-plane indentation moduli of the

pyrolytic graphite sample were measured to be 10.75±0.65 GPa and 9.1±0.26 GPa respectively.

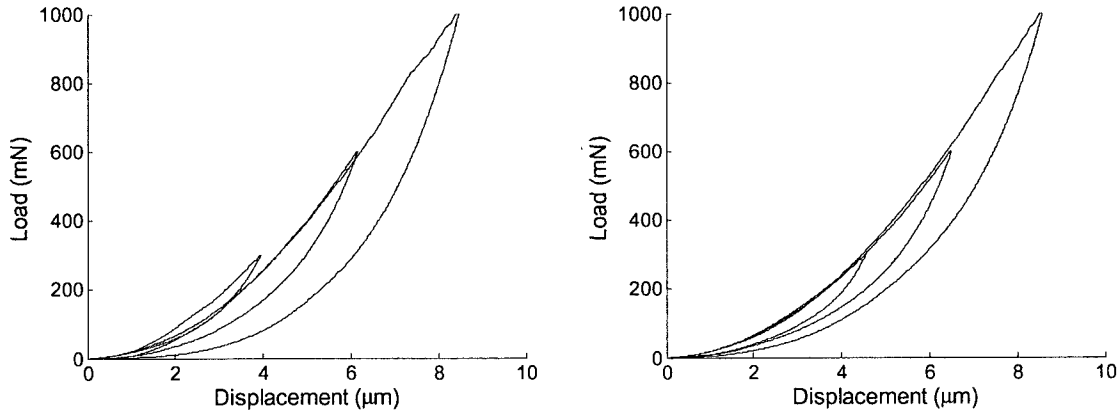

Figure 25: Microindentation load-displacement curves of the pyrolytic graphite sample obtained using Vickers indenter (a) normal to the plane of isotropy (b) parallel to the plane of isotropy.

We also performed microindentation on the glassy carbon sample, the only isotropic pyrolytic carbon we considered. Unlike the bulk PyroC samples or the pyrolytic graphite sample which had a high degree of texture with the graphene-like domains oriented more or less parallel to the plane of isotropy, glassy carbon exhibits an isotropic texture. The load-displacement curves of the glassy carbon sample are shown in Figure 26 below.

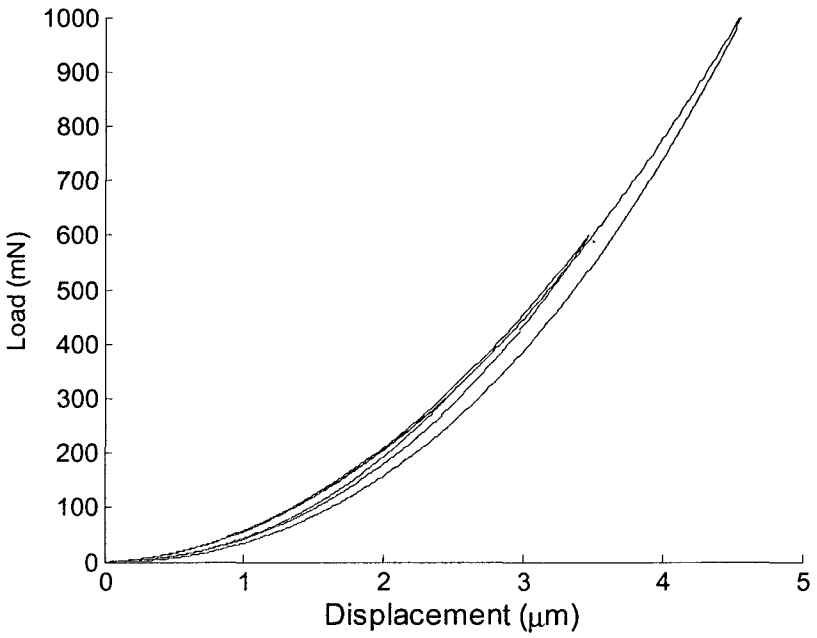

Figure 26: Microindentation load-displacement curve of the glassy carbon sample obtained by the Vickers indenter.

The indentation modulus of Glassy Carbon was measured to be 26.48±0.26 GPa. Since Glassy Carbon is isotropic, the indentation modulus in this case can be regarded as a reduced Young's modulus which is very close to the value of the actual Young's modulus of the material.

Nanobuckling Deformation Mechanism

A surprisingly low in-plane indentation modulus, M_2 (=M_3), was obtained by nanoindentation. It was even lower than the out-of-plane indentation modulus, M_1, especially using the cube corner indenter. This can be attributed to a similar argument that was made about the tension-compression anisotropy, namely the buckling and kinking of the graphene layers in compression. When indenting normal to the plane of isotropy as shown in Figure 27 (a), layers of the pyrolytic carbon that are directly under

the tip undergo an elastic deformation without causing any yielding, thus sampling the stiffness of the material in the direction of the indentation. The estimates of the indentation modulus are then determined based on the stiffness sensed by the indenter.

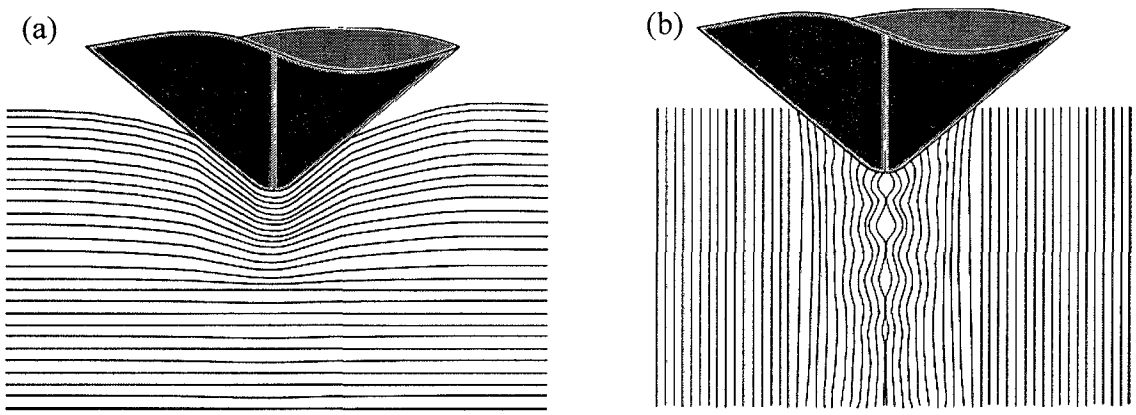

Figure 27: A schematic showing the possible deformation of the pyrolytic carbon when it is subjected to the indentation in the direction (a) normal to the plane of isotropy (b) parallel to the plane of isotropy.

However, in the case of the indentation transverse to the plane of isotropy, the turbostratic structure of the pyrolytic carbon may buckle under the tip by activation of a secondary reversible deformation of individual graphene planes present at that length scale as shown in Figure 27 (b). The kinking and buckling would require a smaller amount of force to penetrate a certain distance, thus lowering the stiffness seen by the indenter, and ultimately, the indentation modulus.

The included angle of an indenter seems to affect the indentation modulus of the bulk PyroC in the direction parallel to the plane of isotropy. The cube corner tip with the included angle of 90° yields the lowest indentation modulus of only about 6.7 GPa. The Berkovich tip with the included angle of 142.3° yields an indentation modulus of about 12.2 GPa. The 3 μm cono-spherical tip which is blunter than the cube corner tip but not as blunt as the Berkovich tip is positioned somewhere in the middle with the indentation

modulus of about 9.3 GPa. We suspect that the geometry of an indenter has a direct impact on the differences in axial and lateral stress fields responsible for the activation of the nanobuckling mechanism of the turbostratic structure of pyrolytic carbon. This was one of the subjects of our FE studies.

FE Studies of Indentation

The Effect of the Anisotropy on the Indentation Modulus

To understand how the anisotropy impacts the indentation modulus, we constructed several 2D axisymmetric models with the varying degree of anisotropy for comparison. Only the indentation normal to the plane of isotropy was considered. We included the isotropic model (E=10 GPa, v=0.3) and several transversely isotropic models with the out-of-plane Young's modulus, E_1, being equal to 10 GPa and the in-plane Young's modulus, E_2 (=E_3), being equal to 10, 5, 2, 1, 0.5, 0.2, and 0.1 times E_1. The in-plane Poisson's ratio, v_{23}, was set at 0.3. The other values of the Poisson's ratios, v_{12} (=v_{13}) and v_{21} (=v_{31}), were selected arbitrarily but used consistently and in accordance to the restrictions set by Kachanov et al[38]. The in-plane shear modulus, G_{23}, was calculated using Equation 15. The out-of-plane shear modulus, G_{12} (=G_{31}), was approximated by Equation 16. Table 3 summarizes the material properties used for these studies as well as the estimated indentation modulus M_1.

Case	E_1 (GPa)	E_2 (GPa)	ν_{12}	ν_{23}	ν_{31}	G_{23} (GPa)	G_{12} (GPa)	**M_1 (GPa)**
$E_2=10E_1$	10	100	0.1	0.3	1	38.46	7.692	**16.17**
$E_2=5E_1$	10	50	0.1	0.3	0.5	19.23	7.143	**14.92**
$E_2=2E_1$	10	20	0.1	0.3	0.2	7.692	5.882	**13.48**
Isotropic	10		0.3			3.846		**10.68**
$E_2=0.5E_1$	10	5	0.2	0.3	0.1	1.923	2.941	**8.61**
$E_2=0.2E_1$	10	2	0.5	0.3	0.1	0.769	1.429	**5.26**
$E_2=0.1E_1$	10	1	1	0.3	0.1	0.346	0.769	**2.97**

Table 3: Elastic constants used in 2D axisymmetric FE modeling.

We utilized these models to produce load-displacement curves. The load was the contact force between a rigid tip and a substrate in the direction of indentation and the displacement was the depth of penetration up to 125 nm. The load-displacement curves were fitted to a power law from about 40 nm to 125 nm and the stiffness (i.e. the slope) was estimated by taking the derivative of the power law relation in respect to the displacement and evaluated at every nm of penetration. The contact area was the actual projected area of contact between the tip and the substrate. It was estimated each time a new node would come in contact with the tip using the equation of the area of a circle. Then we used a polynomial fit to obtain a quadratic equation which was used to predict the area of contact at each increment of displacement. All fits described the data very well with an R^2 value of at least 0.99.

Having the stiffness and the area of contact, we utilized Equation 2 to obtain the indentation modulus at each increment beginning at the increment corresponding to 40 nm of displacement. The estimates of the indentation modulus below 40 nm of displacement were not stable. This may be attributed to the fact that only a few elements were in contact with the tip at shallow depths. The maximum value of the standard

deviation between the estimates for all three indenters was just ±0.22 GPa. Indentation modulus estimates M_{ind} are listed in Table 3 above.

Figure 28 shows the ratio of indentation modulus to the actual modulus along the indentation axis. One can see that the factor of 10 increase or decrease of the modulus in the lateral direction over the modulus along the indentation axis raises or lowers the indentation modulus by about 70% respectively.

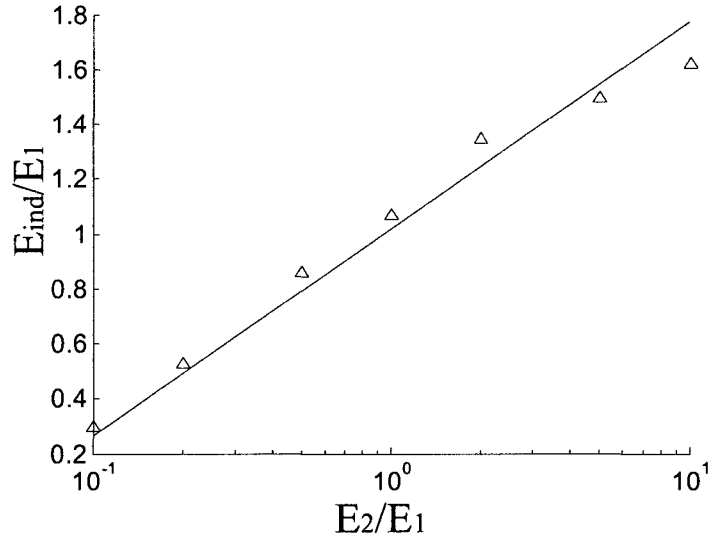

Figure 28: Ratio of indentation modulus to the Young's modulus in the indentation direction as a function of in-plane to out-of-plane Young moduli ratio. The indentation modulus was estimated from analysis of the FE force displacement curves.

This study has shown that the lateral properties have a substantial effect on the indentation modulus. This effect depends primarily on the degree of anisotropy. The higher is the degree of anisotropy, the higher is the contribution of the lateral stresses on the overall indentation response. The dependence of the indentation modulus on the in-plane and out-of-plane ratio presented in Figure 28 is just an approximation, but it yields a valuable insight on role of anisotropy in correlating the indentation modulus to the elastic properties of a material.

FE Indentation Modulus of Bulk PyroC based on Strain Gage Measurements

We estimated the out-of-plane indentation modulus, M_1, of the bulk PyroC by utilizing the elastic constants determined by the strain gage measurements as the material input parameters in the FE models for all three indenters. We considered the indentation normal to the plane of isotropy with the indentation depth of 200 nm. Table 4 summarizes the elastic constants that were used for these simulations and the resulting indentation moduli.

	M_1 (GPa)	E_1 (GPa)	E_2 (GPa)	ν_{12}	ν_{23}	ν_{31}	G_{23} (GPa)	G_{12} (GPa)
Cube Corner	**9.06±.44**	5.2	18.8	0.35	0.22	1.157	7.705	2.713
Cono-Spher.	**9.96±.01**							
Berkovich	**9.18±.47**							

Table 4: Elastic constants based on the strain gage measurements of the bulk PyroC and the FE estimates of the out-of-plane indentation modulus, M_1, for the cube corner, the cono-spherical, and Berkovich indenters.

The FE models did not consider the tension-compression anisotropy of the bulk PyroC detected by the strain gage measurements, so certainly there is an error associated with the estimates of the indentation modulus presented in Table 4. However, since indentation imposes mostly compressive stresses, we selected the elastic constants measured in compression. This pertains to the in-plane and out-of-plane Young's moduli, E_1 and E_2 ($=E_3$), the in-plane Poisson's ratio, ν_{23}, and the out-of-plane Poisson's ratio, ν_{12}. The out-of-plane Poisson's ratio, ν_{31}, was not determined experimentally, so it was calculated based on the elastic symmetry (similar to Equation 11). The in-plane shear modulus, G_{23}, was calculated using Equation 15. The out-of-plane shear modulus, G_{12} ($=G_{31}$), was approximated following the Equation 16.

The FE predictions of the out-of-plane indentation modulus, M_1, for all three indenters were approximately the same (9-10 GPa) and also were very similar to the predictions based on the explicit approximations derived by Delafargue and Ulm[32]. The FE model with the material properties of the bulk PyroC measured by strain gages predicted ~74% difference in the indentation modulus over the modulus in the direction of indentation using the cube corner indenter.

Table 5 presents the out-of-plane indentation modulus, M_1, of the bulk PyroC measured by the nano-, microindentation, und ultrasonic phase spectroscopy[19] as well as its predictions based on Delafargue and Ulm's approximations[32] and on 2D FE modeling.

		M_1 (GPa)
Nanoindentation	Cube Corner	12.21 ± 1.68
	Cono-Spherical	12.09 ± 1.49
	Berkovich	12.25 ± 1.45
Microindentation	Vickers	10.0 ± 0.32
Ultrasonic[19]		9.59
Strain gages		9.38
2D FE modeling	Cube Corner	9.06±.44
	Cono-Spherical	9.96±.01
	Berkovich	9.18±.47

Table 5: Bulk PyroC out-of-plane indentation modulus M_1 obtained by nano-, microindentation, as well as the predictions by Delafargue and Ulm[32] based on ultrasonic phase spectroscopy[19] and strain gage measurements and by 2D FE modeling.

One may observe a considerable difference between the indentation modulus measured using nanoindentation (~12 GPa) and the predicted values by the Delafargue and Ulm's approximations[32] and by the FE modeling (~9 GPa). Although there might be additional causes, we believe that the ~3 GPa difference in the out-of-plane indentation modulus is caused primarily by two reasons. The first reason is the assumption of

tension-compression isotropy used by the Delafargue and Ulm's predictions[32] and in FE modeling. Although an indenter causes mostly compressive stresses in the axial and transverse directions, we found transverse tensile stresses at the surface of a substrate when indenting normal to the plane of isotropy. The magnitudes of these stresses for different indenter configurations were about the same, but 1-2 orders smaller than the compressive stresses (will be discussed further). Therefore, the extent of the error associated with the assumption of tension-compression isotropy is probably small.

The second reason is concerned with the viscoelastic nature of the pyrolytic carbon. We observed the hysteresis loops with distinct loading and unloading curves. The slope of unloading curves was used to estimate the stiffness of the material, and not the slope of the loading curves. The slopes of the unloading curves were considerably higher, and so were the estimates of the indentation moduli. In FE modeling, however, viscoelasticity was not considered and the loading and the unloading curves were identical.

Axial and Lateral Stress Fields between Indenter and Substrate

The in-plane indentation modulus, M_2, obtained via nanoindentation for the sample of the bulk PyroC was lower than the out-of-plane indentation modulus, M_1. We attribute this somewhat surprising result to the elastic nanobuckling deformation mechanism when the indentation is performed parallel to the plane of isotropy. The cube corner, Berkovich, and the cono-spherical tips all produced different values of the in-plane indentation modulus suggesting that the combination of the axial and transverse stresses imposed by an indenter of the certain geometry favor its ability to cause this type of the material response. We propose the axial stress required to initiate nanobuckling

will be lower when there is a lateral tensile stress under an indenter which reduces the lateral constraint for deformation.

Figure 29 and Figure 30 show the axial and transverse stress contours imposed by all three indenters on a substrate using the material properties of the bulk PyroC measured with strain gages. The contours in Figure 29 represent the case when the transverse modulus is stiffer than the modulus in the direction of indentation. This scenario accurately describes the situation of the indentation normal to the plane of isotropy of the bulk PyroC sample.

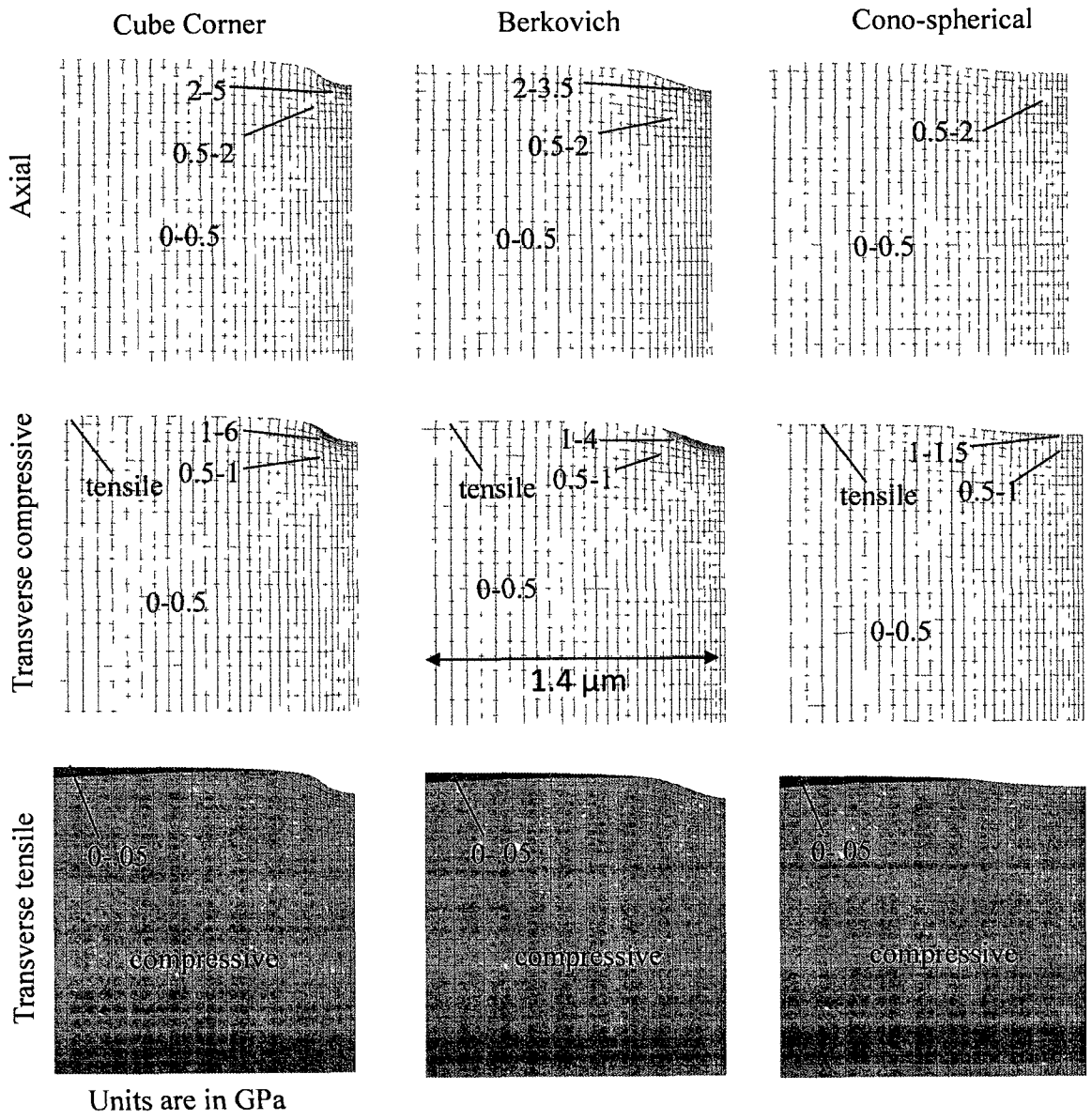

Figure 29: Axial and transverse stress field contours imposed by the cube corner, Berkovich, and the cono-spherical indenters on the substrate with the stiff transverse properties.

The contours in Figure 30 represent the case when the transverse modulus is softer than the modulus in the direction of indentation. We realize that this model does not precisely correspond to the indentation parallel to the plane of isotropy of the bulk PyroC because it assumes the same properties transverse to the line of symmetry, but it still

yields some insight on the material behavior. All simulations were for a displacement of 116 nm because it was as deep the cube corner indenter was able to penetrate without the need to remesh the model (which was not implemented to preserve consistency when considering different indenter geometries).

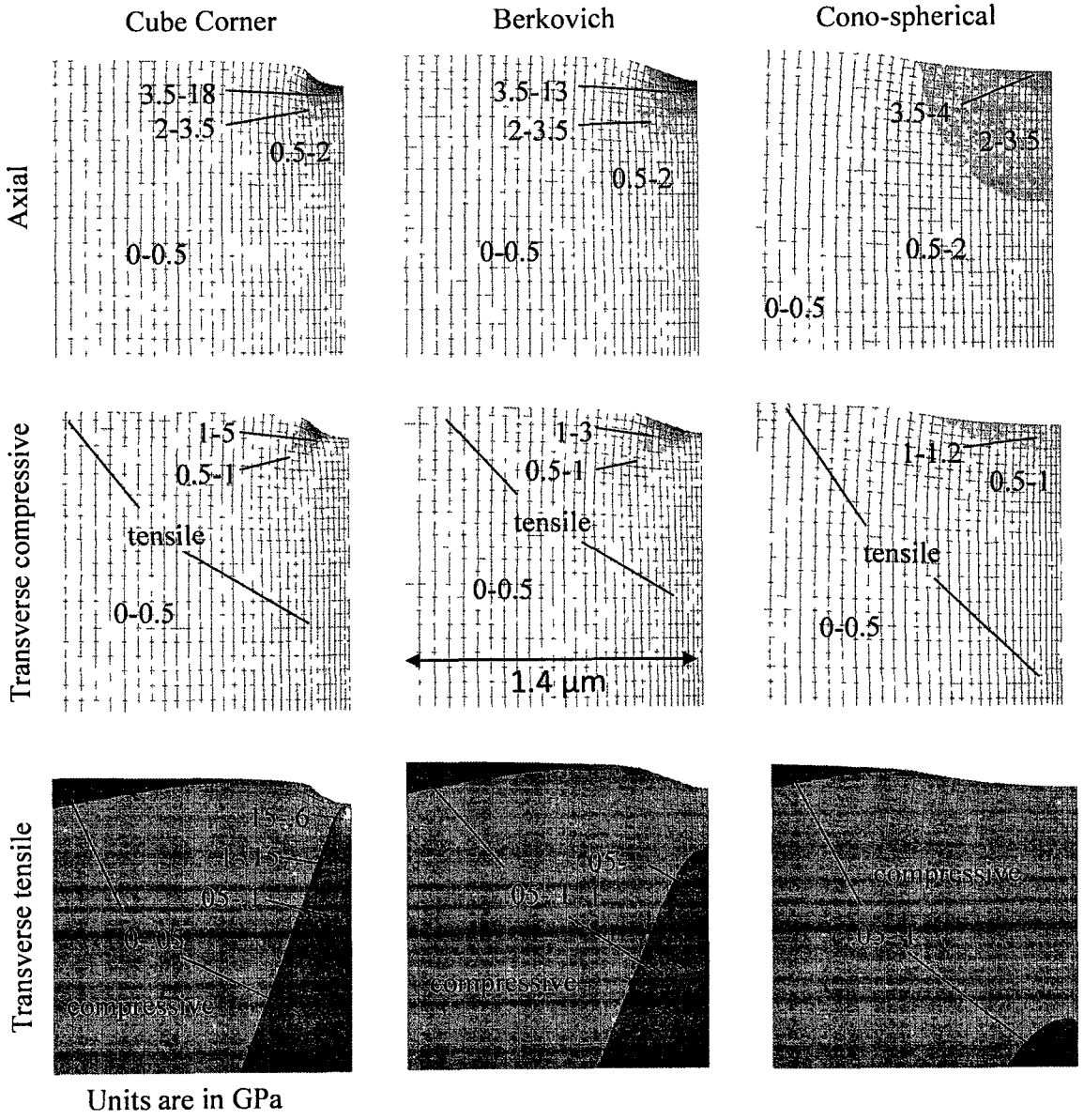

Figure 30: Axial and transverse stress field contours imposed by the cube corner, Berkovich, and the cono-spherical indenters on the substrate with the soft transverse properties.

Clearly the extent of the axial compressive stresses and their magnitudes are much higher for the soft transverse indentations, or in the case of the bulk PyroC, for the indentations parallel to the plane of isotropy for which we observed low values of the indentation modulus. The magnitudes of these stresses are highest for the cube corner indenter and are lowest for the cono-spherical indenter. However, the cono-spherical indenter samples the largest volume. Compressive axial stresses are the driving force for the activation of the elastic nanobuckling and their magnitudes appear to be very high, especially for the cube corner indenter. However, with the activation of the elastic nanobuckling mechanism, these stresses would significantly drop.

In the case of the stiff transverse indentation, the extent and the magnitudes of the axial compressive stresses is much smaller and also not nearly as the indenter shape-dependent. This observation supports the experimental measurement of the out-of-plane indentation modulus, M_1, which was found to be about the same using any of the three indenters.

The other important observation is the presence of the transverse tensile stresses for the soft transverse indentations which are absent for the stiff transverse indentations. These stresses would reduce the lateral constraint for buckling. The magnitude of the transverse tensile stress field is greatest for the cube corner indenter and lies immediately under the tip. The same stress field, however, for Berkovich and for the cono-spherical indenters lies approximately 200 nm and 1000 nm respectively under the indenter and their magnitudes a much smaller than for the cube corner indenter. Transverse tensile stresses are also present at the surface of the substrate.

Based on these observations, we propose that the cube corner indenter has the lowest indentation modulus in the direction parallel to the plane of isotropy because of the combination of high in-plane compressive stresses and high transverse tensile stresses both of which enhance nanobuckling. The cono-spherical indenter has a lower indentation modulus than the Berkovich indenter because of the volume of the stressed zone is much larger.

Effects of the Force Vector on the Indentation Modulus

The in-plane indentation modulus, M_2, obtained by nanoindentation for the sample of the bulk PyroC has a tendency to decrease with the increasing penetration depth (see Figure 22 (b)). We used FE studies of the effects of anisotropy on the indentation modulus to show that the properties of a transversely isotropic material lateral to the axis of indentation have substantial effects on the indentation modulus. The goal of this section is to examine how the vector of the contact force changes for different indenters as they penetrate deeper into the material. The expectation was that the contribution of the transverse properties would increase with the increasing angle between the indentation axis and the resultant force vector.

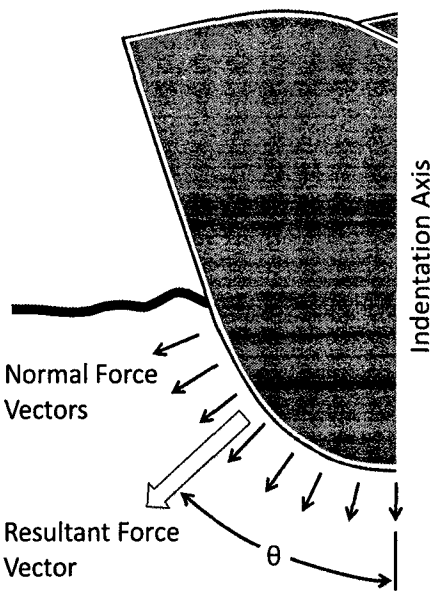

Figure 31: Schematic of an indenter showing the angle θ between the indentation axis and the resulting force vector.

We utilized 2D axisymmetric models for the cube corner, Berkovich, and cono-spherical

tips indenting into a transversely isotropic medium with both the soft transverse and stiff transverse properties. The material properties of the substrate were based on the bulk PyroC elastic constants determined by the strain gage measurements. The angle θ between the indentation axis and the resultant force vector shown in Figure 31 was calculated using the following formula:

$$\theta = \tan^{-1}\left(\frac{F_y}{F_x}\right) \tag{17}$$

where F_x is the component of the resultant force vector in the direction of indentation, and F_y is the component of the resultant force in the transverse direction. Figure 32 shows how the angle of the resultant force vector changes for all three indenters with the increasing penetration depth.

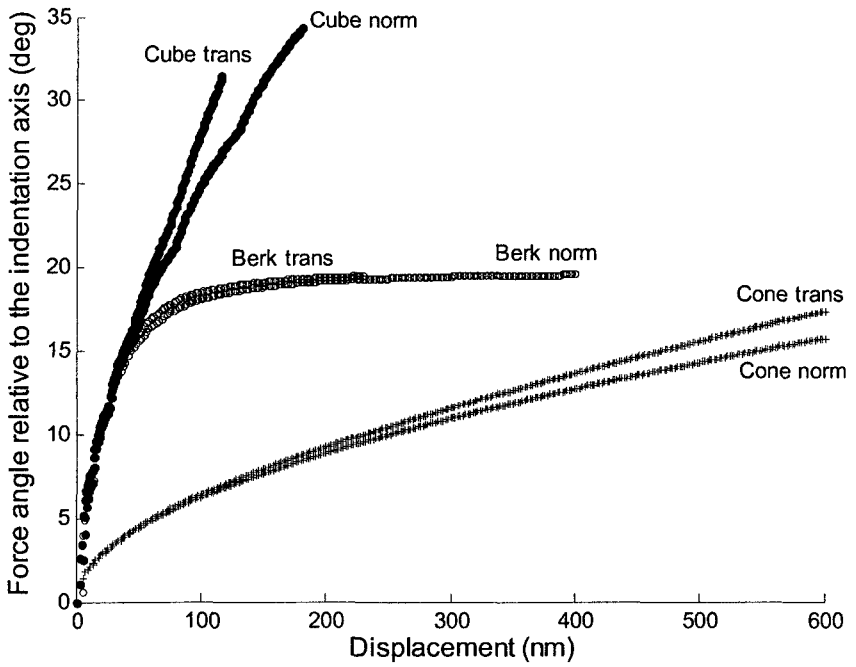

Figure 32: Dependence of the resultant force angle relative to the indentation axis on penetration depth for all three indenters indenting into a transversely isotropic material with both soft transverse (trans) and stiff transverse (norm) properties.

The resultant force angle for the Berkovich indenter saturates fairly quickly because it does not take long for the indenter to penetrate past the spherical region of the tip. The simulations for the cube corner indenter were unable to reach past the spherical part of the tip. The resultant force angle for the cube corner indenter is expected to saturate some distance past that point. The angle of the resultant force continually increases with increasing depth for the cono-spherical indenter thereby increasing the impact of the soft transverse elastic modulus.

These observations are very consistent with the nanoindentation estimates of the in-plane indentation modulus of the bulk PyroC presented in Figure 22 (b). Both the angle of the resultant force in Figure 32 and the in-plane indentation modulus, M_2 (=M_3), in Figure 22 (b) saturate at about 150-200 nm depth for the Berkovich indenter. For the cono-spherical indenter, saturation was not achieved due to the constant increase of the force angle at the considered depth range. The in-plane indentation modulus obtained by the cube corner indenter saturates at about 300 nm depth. However, we were not able to run the simulations for the cube corner tip to this depth to show a correlation. Nonetheless, it shows a good correlation between the drop in the in-plane indentation modulus with the increasing displacement and the penetration depth at which the resultant force vector saturates.

CHAPTER 4

CARBON-CARBON COMPOSITE TESTING

Our collaborators from KIT provided us with samples of the carbon-carbon composites manufactured at pressures of 10, 20, and 30 kPa and a constant temperature of 1100°C. This sample variety enabled us to study the influence of the pressure on the microstructure and on the elastic properties of the material. We performed nanoindentation experiments for all three samples to examine the spatial variation of the indentation modulus of the pyrolytic carbon layers surrounding the fiber preforms. In addition, we performed extinction angle measurements on the same samples using PLM to determine the degree of anisotropy of the pyrolytic carbon layers and to correlate the optical anisotropy with the structural anisotropy detected by nanoindentation.

Microstructure

As mentioned earlier, the microstructure of the pyrolytic carbon matrix is strongly influenced by the manufacturing conditions. Therefore, it is of no surprise that the provided samples also exhibited significant differences in the microstructure observed in the polarized light microscope (PLM) and in the indentation modulus obtained by the nanoindentation.

The Nikon Epiphot microscope model #360340 was used to obtain the micrographs of the studied samples. Figure 33 (a-c) shows the microstructure of all three

samples at low magnification (100x) observed in PLM. At this level, it is difficult to distinguish the specifics of the microstructure, but even at this magnification one may notice a considerable difference in texture, especially between the sample at the pressure of 10 kPa and the other two samples.

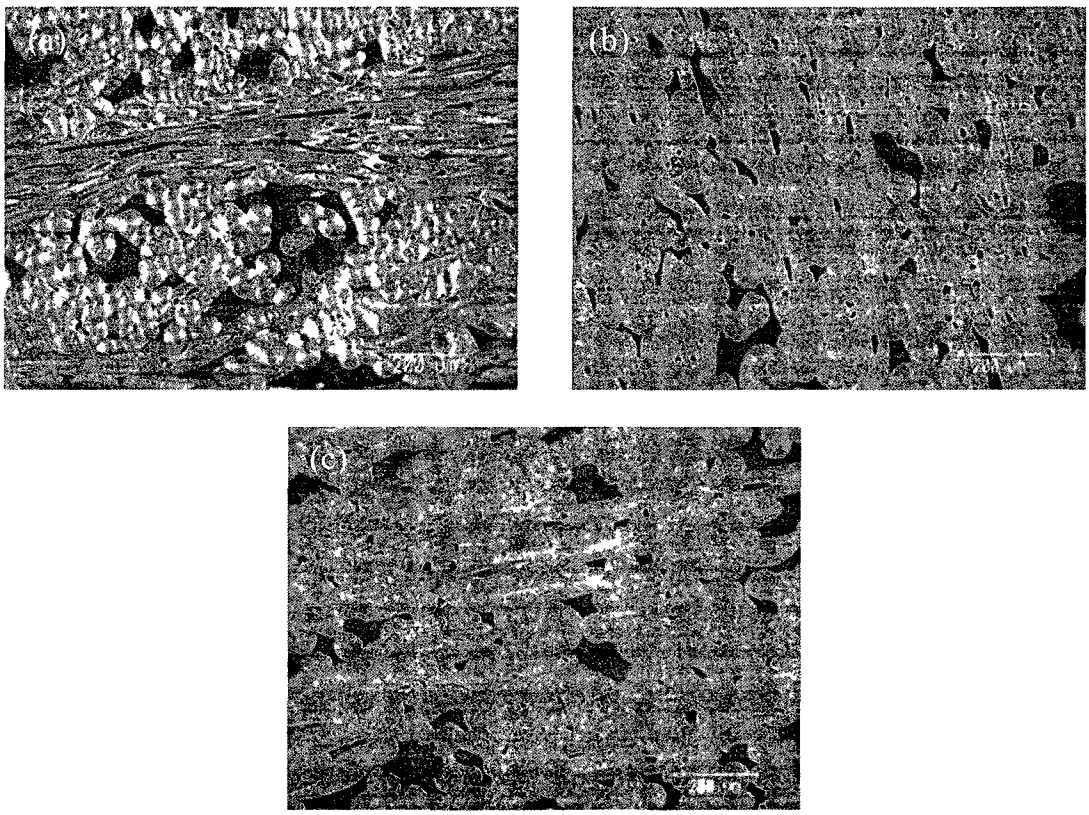

Figure 33: PLM images of the carbon-carbon composite samples infiltrated at the pressure of (a) 10 kPa, (b) 20 kPa, and (c) 30 kPa showing microstructure at 100x.

The difference in texture between the samples is more noticeable at higher magnification (400x) as shown in Figure 34 (a-c). The microstructure of the PyroC for the 10 kPa sample appears to be very "grainy", i.e. exhibiting tilted regions which distribution is rather chaotic as if it was not well polished. The texture of the 20 kPa and 30 kPa samples appears to be very smooth, but exhibits a lower level of polarized activity.

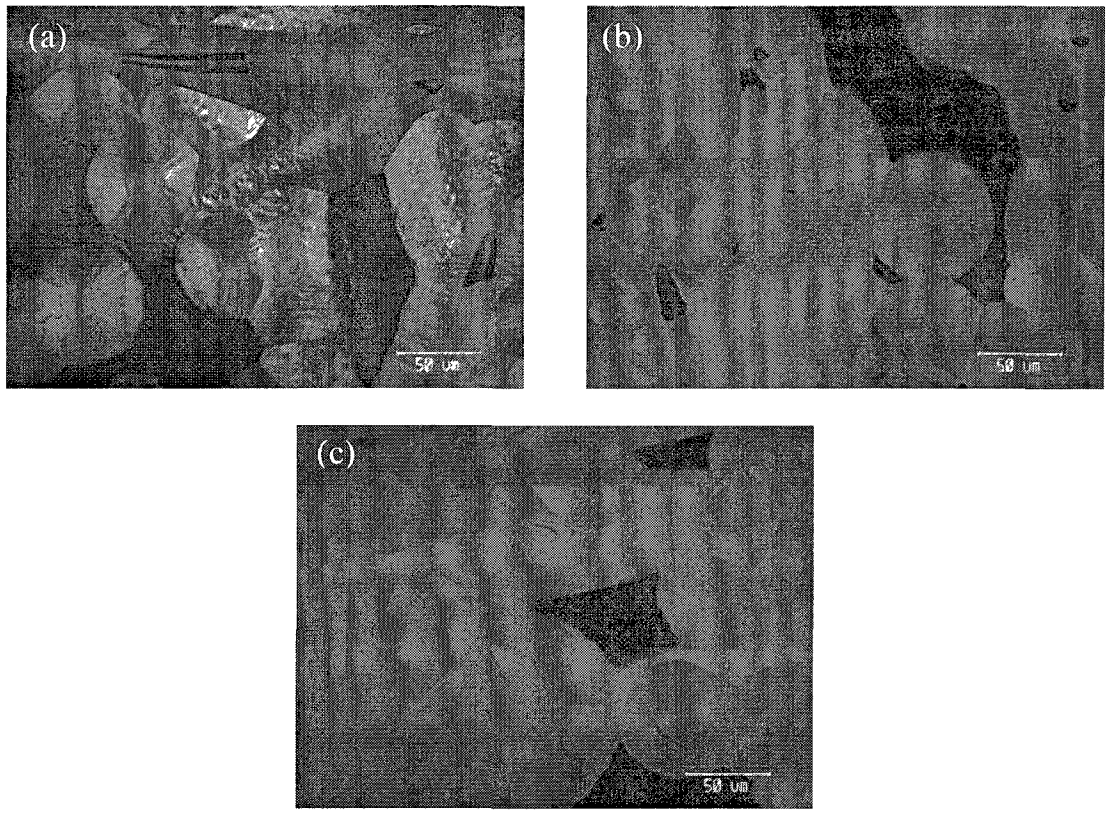

Figure 34: PLM images of the carbon-carbon composite samples with the pressures of (a) 10 kPa, (b) 20 kPa, and (c) 30 kPa showing microstructure at 400x.

There is a higher contrast of the light and dark phases for the 10 kPa sample than for the other two samples when viewed using polarized light. A higher contrast suggests a higher degree of texture (or graphitization). These images were only partly polarized because the polarizer and the analyzer were not at the 90° angle to each other at which the maximum polarization is achieved and at which the Maltese crosses are visible. Instead, they were at some arbitrary angle to each other; however, both the light and dark phases were still clearly visible.

The sample manufactured at 10 kPa pressure appears to be not only more textured than the samples produced at 20 kPa and 30 kPa, but it also has two distinct zones that have different sensitivity to the polarized light as shown in Figure 35 (a). The high

contrast of the thick outer layer suggests that it is a high textured pyrolytic carbon, and the thin inner layer of the PyroC which is in contact with the carbon fiber appears to be a low to medium texture as it is much less sensitive to the polarized light. We also observed circumferential boundaries between layers within the carbonaceous matrix in the HT regions.

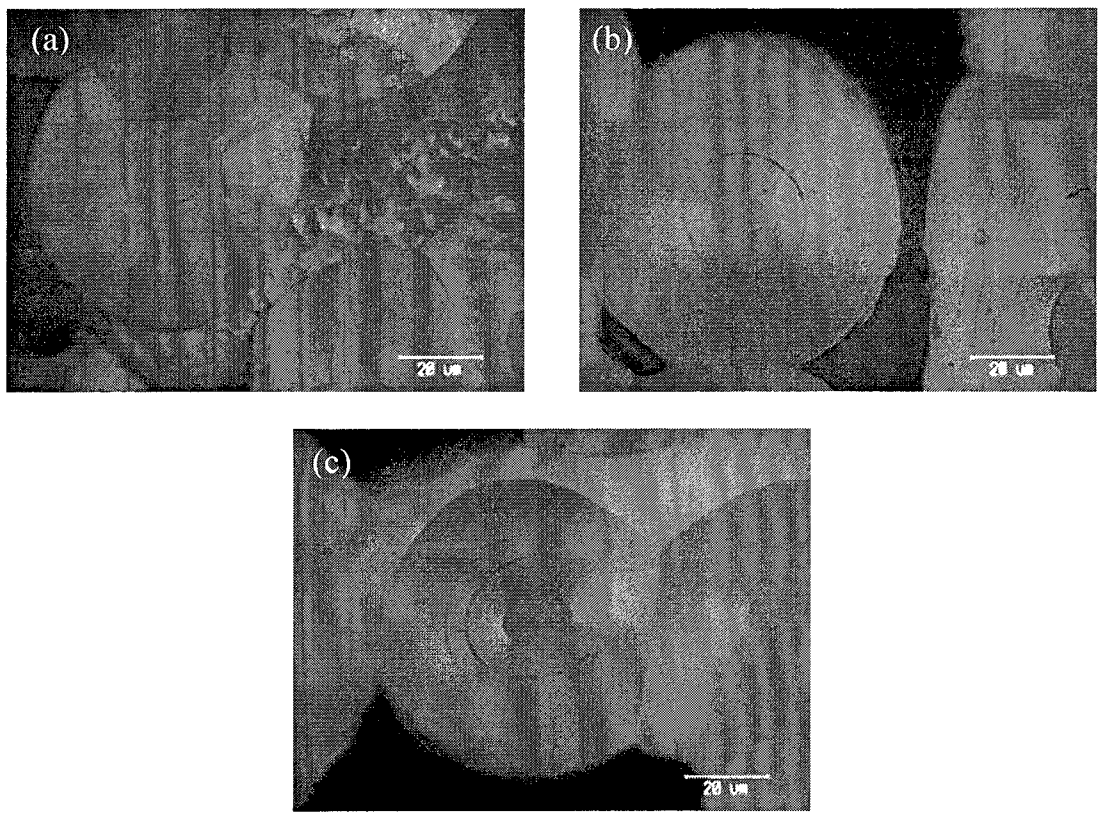

Figure 35: PLM images of the carbon-carbon composite samples with the pressures of (a) 10 kPa, (b) 20 kPa, and (c) 30 kPa showing microstructure at 1000x.

The microstructure appears significantly different for the 20 kPa sample as presented in Figure 35 (b). The contrast between the dark and the light reflections is barely visible suggesting that the PyroC in this sample has a much lower degree of texture, most likely of low to low/medium texture. We also observed circumferential cracks which can be attributed to several factors such as the disruptions or alterations in

the manufacturing or curing process, differences in the coefficients of thermal expansion of the fiber, the matrix and even the individual layers within a matrix. Polishing of the samples could also generate these cracks along the weak interfaces. The microstructure of the 30 kPa sample shown in Figure 35 (c) looks very similar to what was observed for the 20 kPa sample. It also exhibits a low sensitivity to the polarized light suggesting a LT or LT/MT pyrolytic carbon.

Extinction Angle Measurements

Polarized light microscopy is capable of distinguishing between isotropic and anisotropic substances. Isotropic materials have only one refractive index and no restriction on the vibration direction of light passing through them. Anisotropic materials, however, have optical properties that vary with the orientation of the incident light with respect to the crystallographic axes. Reznik et al[14] proposed an improved method for angular-resolved characterization of the optical anisotropy of the pyrolytic carbon with circular morphology which suggests the correlation between the optical and structural anisotropy of a pyrolytic carbon matrix around fibers. Figure 36 (a) shows a PLM image of the fiber surrounded by the pyrolytic carbon for the 10 kPa sample under crossed polarizer and analyzer Nicols yielding an intensity pattern in the form of a Maltese cross. This pattern is realized for the direction parallel and perpendicular to the polarizer position only as the light reflected at these angles will be completely extinguished by the crossed analyzer.

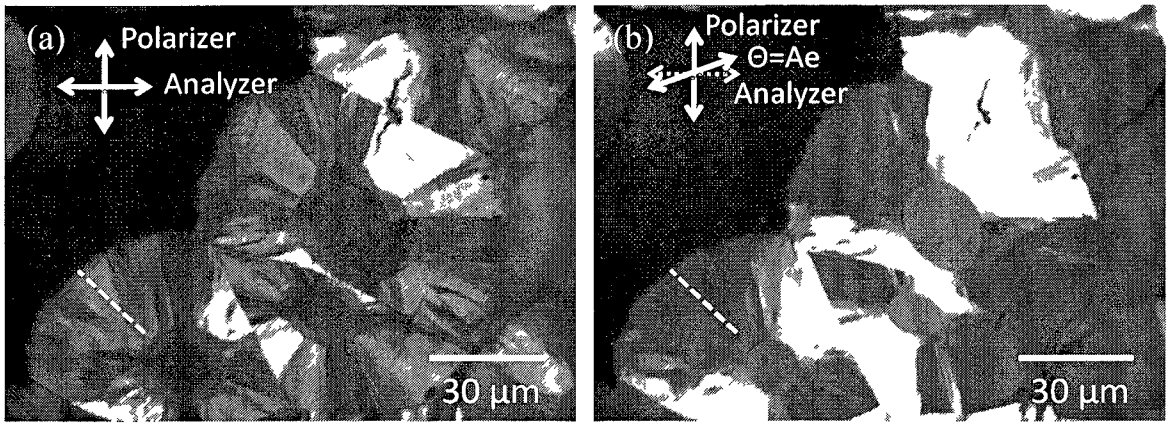

Figure 36: PLM micrographs of a polished cross-section of 10 kPa sample when (a) analyzer is perpendicular to polarizer and the quadrant lying at about 45° is light (indicated by white dashed line) and Maltese crosses are visible; (b) analyzer is apart from cross.

By rotating the analyzer, two of the four diagonal quadrants lying in between the contours of a Maltese cross change their intensity from bright to dark as shown in Figure 36 (b). The angle of the analyzer that corresponds to the lowest intensity level is called the extinction angle, *Ae*, and is used to characterize the degree of texture of the pyrolytic carbon. More details on the theoretical calculations and the physical meaning of the extinction angles can be found in the work by Bourrat et al[15,16] and by Bortchagovsky et al[17,18].

We utilized Leitz® Ortholux 2 Pol BK microscope equipped with a linear polarizer and an adjustable analyzer to measure the extinction angles of 10, 20 and 30 kPa C/C composite samples as a function of distance from the fiber. Conventionally, the texture characterization using PLM is performed manually by an operator who rotates an analyzer and visually observes at which angle the extinction is achieved. Although this technique can be used with success for a rapid texture characterization, its accuracy may be as low as ±3° between different operators. Galer[46] points out that the human eye is sensitive to contrast changes rather than to absolute levels of brightness and it can

distinguish between less than 64 gray levels comparing to at least 256 gray levels distinguished by digital cameras.

We obtained PLM images in .tiff format using Leica® DFC 320 camera at 1-2 degrees increments of the analyzer. The samples were locked in place so it was assumed that pixels between the images were aligned with each other. The intensity level at each pixel was plotted using MatLab® 2009 software as shown in Figure 37 (a). The noise was filtered out using the median filter averaging over 9x9 pixel areas. The dashed line indicates the 45° line along which we constructed a light intensity profile as a function of distance from the fiber as shown in Figure 37 (b) at each pixel along that line.

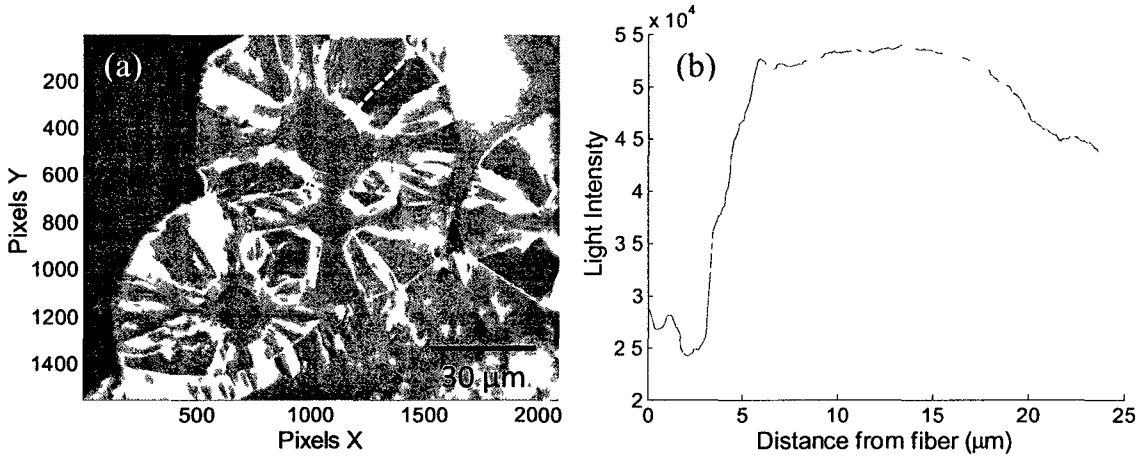

Figure 37: (a) A typical image of the C/C composite sample observed in PLM showing the light intensity level at each pixel, and (b) the light intensity profile across one of the quadrants of the Maltese cross.

The light intensity values along the same line were found for all images starting from the position when the polarizer and analyzer were crossed (i.e. at 0°) to the position when they were uncrossed up to 30°. The intensity levels at each corresponding pixel between the images obtained at different analyzer positions were compared and the angle that corresponded to the lowest intensity level was selected as the extinction angle.

Figure 38 shows the plot of extinction angles found for all three C/C composite samples. The extinction angle of the ~5μm thick layer of the PyroC adjacent to the fiber for the 10 kPa sample was measured to be approximately 11°. According to the nomenclature by Reznik et al[6], the texture of this layer is classified as low-to-medium texture (LT-MT). The rest of the PyroC of the 10 kPa sample exhibited a higher degree of optical anisotropy with the measured extinction angle of approximately 18° (HT).

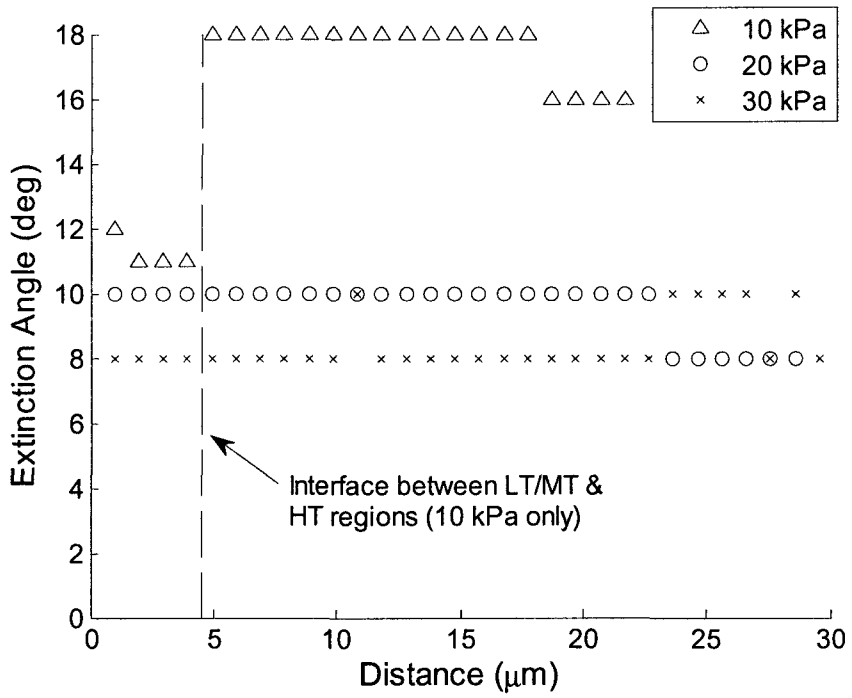

Figure 38: Plot of the extinction angles of the PyroC as a function of distance from the fiber for the 10, 20, and 30 kPa samples.

The texture of the 20 kPa sample was also estimated to be LT-MT and uniform through the thickness of the material. The 30 kPa sample was measured to be LT with the extinction angle of approximately 8°. We observed a slight change in the extinction angle at approximately 17 μm for the 10 kPa sample and at 23 μm for the 20 and 30 kPa samples. This result may be attributed to a sudden change in texture or to imperfections

of the sample on which these measurements were carried out. These results can be improved by analyzing more areas and by increasing the angle variation from 1-2 degrees to less than one degree.

These values are only estimates and there are several sources of error associated with these experiments. We assumed that the 0° dial position of the analyzer corresponded to the position when the polarizer and analyzer were exactly perpendicular to each other. Also, the noise of the light source could introduce an error to the light intensity captured by the camera. However, these estimates of the extinction angles provide a meaningful insight on the effects of the manufacturing pressure on the resulting texture of the PyroC.

Nanoindentation of C/C Composites

These samples were tested using nanoindentation. We used the cube corner indenter for all experiments and the indentation was performed in the direction parallel to the expected plane of isotropy. It was already shown that the indentation in this direction does not correlate with the macroscopic elastic properties of the material. However, these experiments could demonstrate if these C/C composite samples exhibit the elastic properties gradient as a function of distance from the fiber and what are the effects of the manufacturing pressure on the microstructure of the material.

The indents were made both in the fibers and in the matrix. Figure 39 (a-b) shows the PLM image of a typical carbon fiber in cross-section surrounded by the pyrolytic carbon matrix deposited at 10kPa and a corresponding SPM image of the fiber on which we performed nanoindentation. The indents were performed at 3 μm spacing starting at

the center of the fiber and included the areas of the fiber, MT and HT layers of the PyroC. Indentation was performed at least on three different fibers/PyroC for each sample.

The highest indentation modulus values were recorded in the fibers (~30 GPa). The PyroC layer adjacent to the fiber for the 10 kPa sample exhibited lower values of the indentation modulus (15-17 GPa). The indentation modulus was found to be significantly lower for the rest of the PyroC (~12 GPa) and we observed no indentation modulus gradient as a function of distance away from the fiber. The slight variation was primarily due to the surface roughness and/or imperfections of the PyroC.

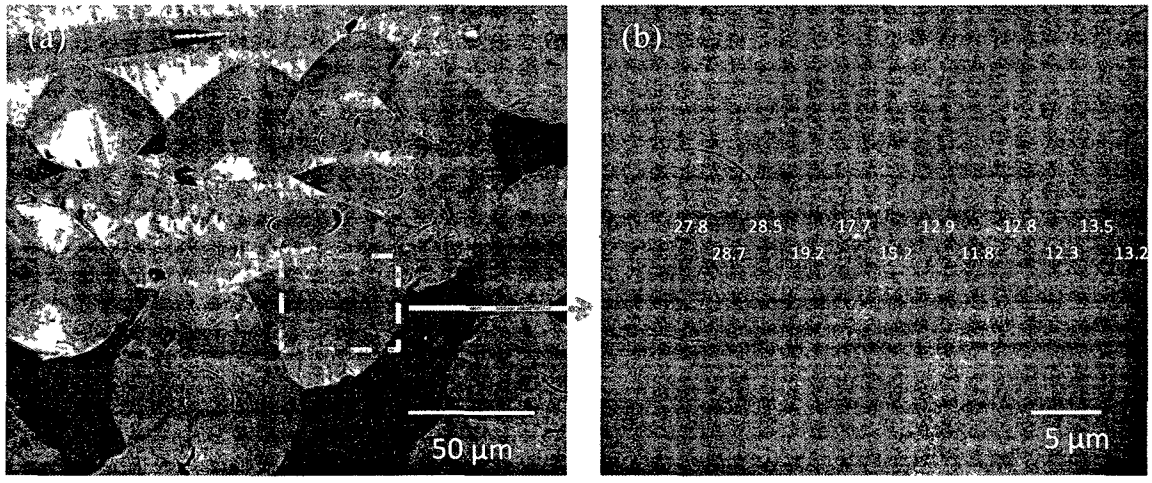

Figure 39: (a) PLM image showing the cross-section of a typical carbon fiber surrounded by PyroC deposited at 10 kPa and (b) the corresponding SPM image of the same area on which we performed nanoindentation with the spacing of 3 µm.

These experiments were also carried out in the direction normal to the length of the fibers as shown in Figure 40 (a-b). In both cases, however, in the directions parallel and normal to the fibers, the indentation was performed parallel to the expected plane of isotropy of the pyrolytic carbon layers. We observed similar values of the indentation modulus of the PyroC and practically the same trend of the indentation modulus variation as a function of distance from the fiber. However, it was not clear why the indentation

modulus of the fibers in the direction normal to the length of the fibers exhibited lower indentation modulus comparing to the indentation along the length of the fibers. This result may be explained by the microstructure of the carbon fibers used as preforms (i.e. PAN-, MP, etc.).

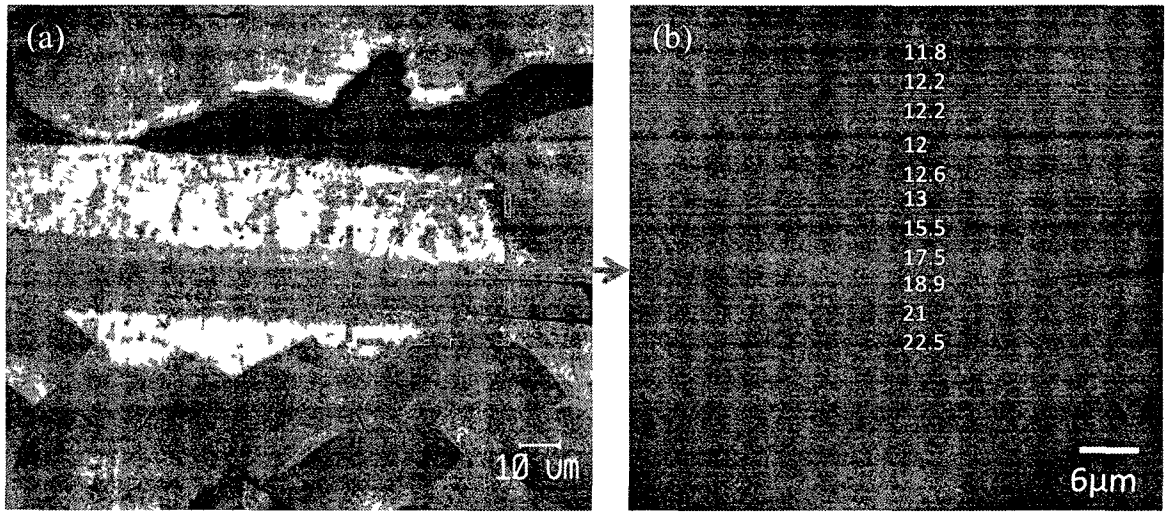

Figure 40: (a) PLM image showing the cross-section of a typical carbon fiber surrounded by PyroC normal to the length of the fiber and (b) the corresponding SPM image of the same area on which we performed nanoindentation with the spacing of 3 µm.

Nanoindentation was also performed on the other two samples manufactured at 20 and 30 kPa. The average indentation modulus of at least three different areas for each of the 10, 20, and 30 kPa samples as a function of distance away from a fiber is shown in the Figure 41 below. The indentation modulus of the carbon fibers for all three samples was found to be relatively uniform through the cross-section of the fiber; however, we observed lower values near the interface of the fiber and the matrix. Lower indentation modulus of the fibers may be attributed to a smaller fraction of the lateral constraint when indenting near the edge due to the softer matrix and cracks between fibers and the PyroC.

The 10 kPa sample exhibited the lowest indentation modulus with different values at the MT and HT regions, but without a textural gradient within those regions. The indentation modulus for the 20 kPa sample was found to be higher than for the 10 kPa sample and uniform along the deposition direction of the PyroC. The 30 kPa sample exhibited the highest values of the indentation modulus and we also observed a slight drop in indentation modulus at about 6 μm away from the fiber, approximately at the same distance at which we observed the decrease in the extinction angle.

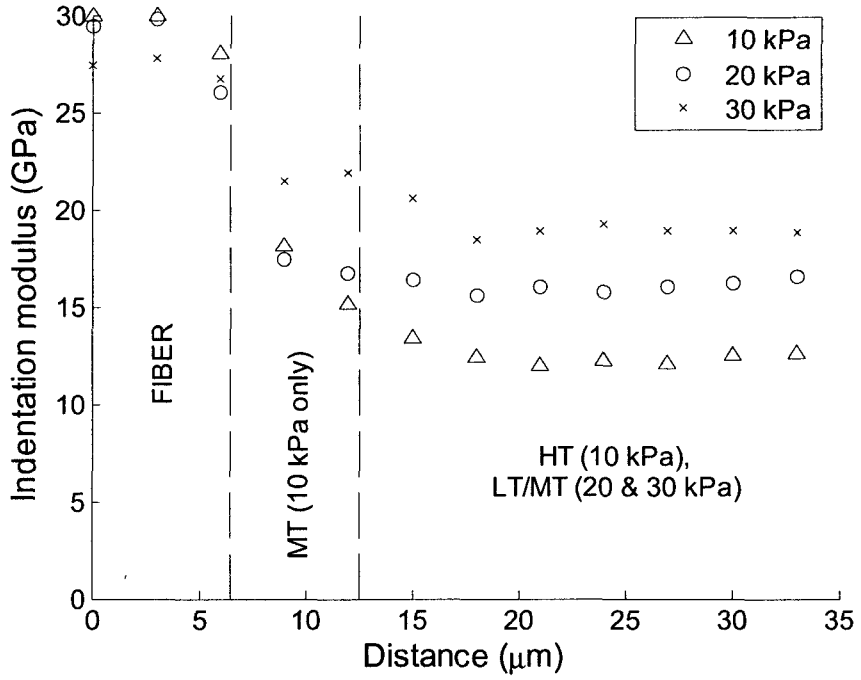

Figure 41: Average in-plane indentation modulus estimates of the C/C composites manufactured at 10, 20, and 30 kPa pressures as a function of distance away from the center of a fiber.

The indentation modulus of the fibers, although important, was not our primary focus. We were primarily interested in the spatial resolution of the elastic properties of the pyrolytic carbon layers that surround the fibers. The estimates of the indentation

modulus presented in Figure 41 provide some useful information on how the manufacturing conditions affect the elastic properties of the deposited pyrolytic carbon.

Correlation between Nanoindentation and Extinction Angle Measurements

Both nanoindentation and extinction angle measurements yielded consistent results. This enabled us to correlate the optical anisotropy of the PyroC observed in PLM with the structural anisotropy detected by the indenter and to make an assessment on how the manufacturing pressure affects the microstructure and the elastic properties of the pyrolytic carbon matrix.

The PLM studies of the 10 kPa sample have shown that the PyroC have two distinct areas: a narrow band which corresponds to MT PyroC with the rest of the matrix being high texture pyrolytic carbon. The nanoindentation into the MT PyroC yielded higher values of the indentation modulus than in the areas with the high texture. It may be attributed to the fact that the layers of the HT PyroC are more sensitive to the nanobuckling damage mechanism than the layers of the MT PyroC when indenting parallel to the plane of isotropy because the graphene planes of the high texture pyrolytic carbon have a higher degree of order and are more likely to buckle under the indenter. In addition, the indenter tip used for these experiments was the cube corner tip which has a greater tendency to activate the nanobuckling deformation mechanism.

The indentation modulus of the pyrolytic carbon was significantly higher for the 20 kPa sample and was relatively constant through the thickness. We estimated low to low/medium texture for this sample based on the extinction angle measurements and, therefore, the graphene planes are less likely to buckle under the tip because they were not nearly as parallel to the direction of indentation as in HT PyroC. The indentation

modulus of the 30 kPa sample yielded the highest estimates of the indentation modulus and the lowest degree of texture among the considered samples. This trend suggests that the increase in the manufacturing pressure decreases the degree of the pyrolytic carbon texture.

The lower indentation modulus, however, does not necessarily imply a lower elastic modulus in the direction of indentation. In fact, the value of the in-plane elastic modulus of a HT PyroC is expected to be higher than the one of a LT PyroC because high textured pyrolytic carbon has a higher fraction of the strong σ-bonding in-plane. Indentation parallel to the plane of isotropy, however, does not accurately capture the macroscopic materials properties.

CHAPTER 5

MECHANISM OF DAMAGE DURING INDENTATION OF BULK PYROC

Failure of the Bulk PyroC Layers Subjected to Nanoindentation

As stated previously, the nanoindentation curves chosen for the analysis exhibited a nearly elastic response with a certain amount of hysteresis. No evidence of permanent deformation was observed neither in the load-displacement curves nor at the surface of a sample after scanning the site of an indentation using SPM mode for the nanoindenter. This was the case for most of the nanoindentation experiments. However, we observed some permanent damage caused by the cube corner tip and by the cono-spherical tip indenting normal to the plane of isotropy of the bulk PyroC at loads exceeding 400 μN and 5000 μN respectively. This observation was confirmed by the presence of the discontinuities in the load-displacement curves and by the material pile-ups around an indentation area.

Discontinuities in the Load-Displacement Curves

The examples of the load-displacement curves obtained by the cube corner tip and by the cono-spherical tip that featured the discontinuities are shown in Figure 42 below.

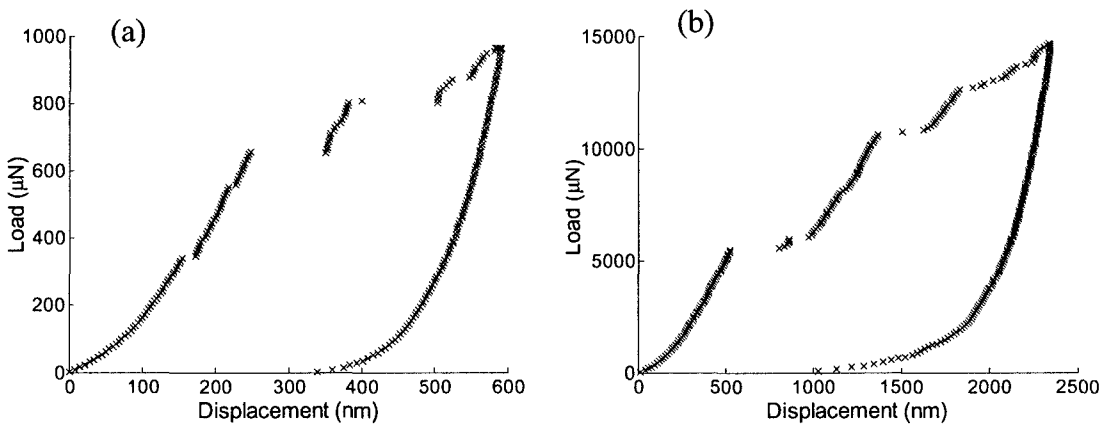

Figure 42: Discontinuities in the load-displacement curves attributed to pop-ins of the pyrolytic carbon layers during the indentation normal to the plane of isotropy using (a) the cube corner indenter and (b) the cono-spherical indenter.

These discontinuities represent the release of the elastic strain energy which results from the substantial pop-ins of the pyrolytic carbon layers under a given indenter load. For the cube corner indenter, the discontinuities began to occur at the loads of 300-400 μN which corresponds to only about 150-180 nm depth. It took a lot more force to cause pop-ins using the cono-spherical indenter. The pop-ins were not observed until the loads exceeded 5,000 μN which corresponds to the displacement of 500 nm. No discontinuities were observed using the Berkovich indenter up to the instrument's maximum load of 15,000 μN as shown in Figure 43.

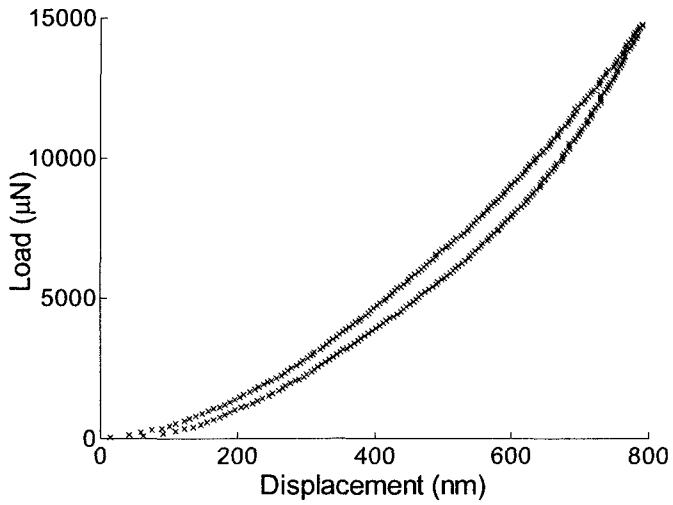

Figure 43: The load-displacement curves obtained by the Berkovich tip indenting normal to the plane of isotropy of the bulk PyroC showing its complete reversibility without any permanent deformation up to the max load of 15,000 μN.

Material Pile-Ups Observed by SEM and by SPM

In addition to the discontinuities in the load-displacement curves, the further evidence of the permanent deformation was found by SEM and by SPM. Figure 44 (a-d) shows the SEM images of the material pile-ups that were formed after the indentations for which discontinuities were observed. In the cases for both the cube corner tip and the cono-spherical tip, the damaged layers of the pyrolytic carbon seem to pucker open and to create large material pile-ups when the load is released.

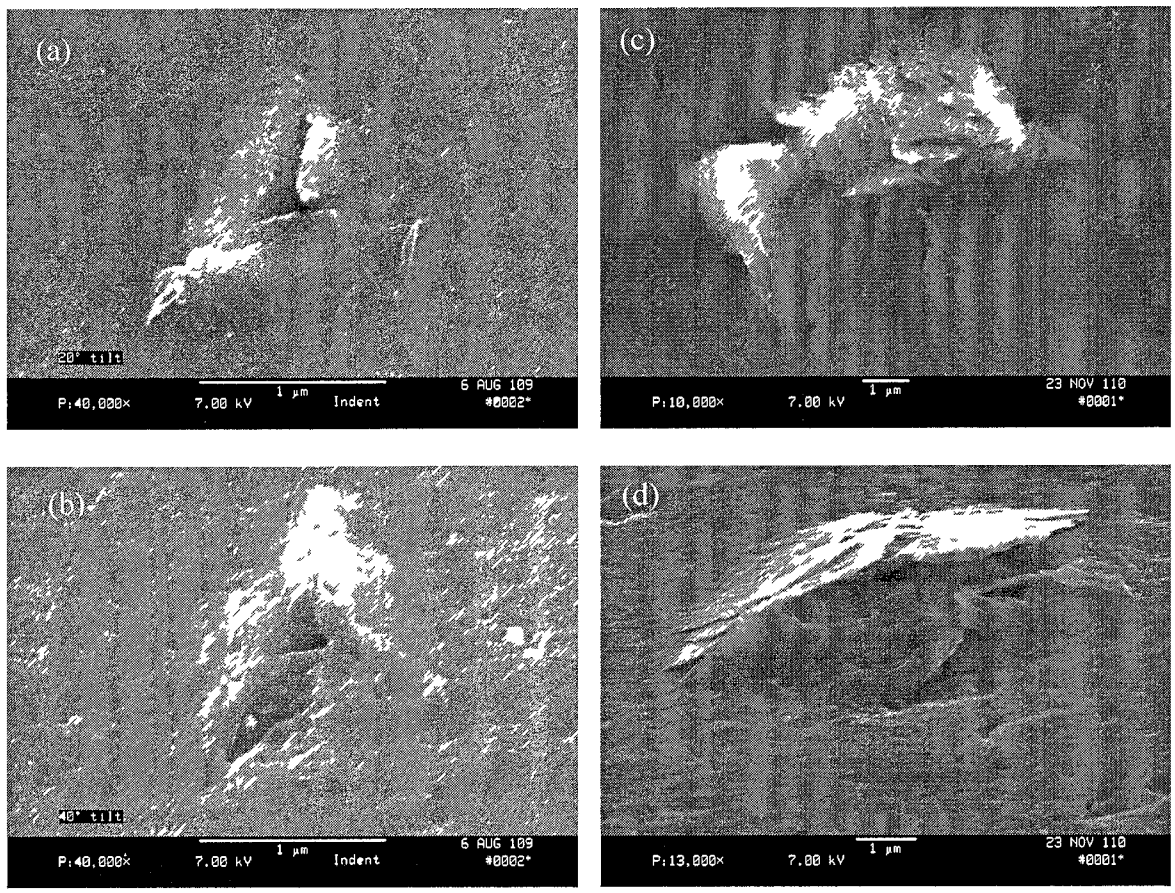

Figure 44: SEM images of the material pile-ups at the sites of the indents for which discontinuities were observed using (a,b) the cube corner tip and (c,d) cono-spherical tip.

Similar observations were made using SPM. Figure 45 shows the topographical scan of the surface on which we performed a series of indentations using the cube corner indenter. Considering that it was an array of indents with the constant spacing, it became apparent that some of those indents exhibited permanent deformation while others were elastic. The corresponding load-displacement curves are also shown for several of those indents. It is important to note that the indents with the larger discontinuities in the load-displacement curves produced larger material pile-ups than the indents that exhibited smaller discontinuities. For the indents with no discontinuities, there were no material pile-ups, thus no permanent deformation. In fact, the upper portion of the surface was

also subjected to indentation but those indents exhibited an elastic response and left no distinct marks on the surface.

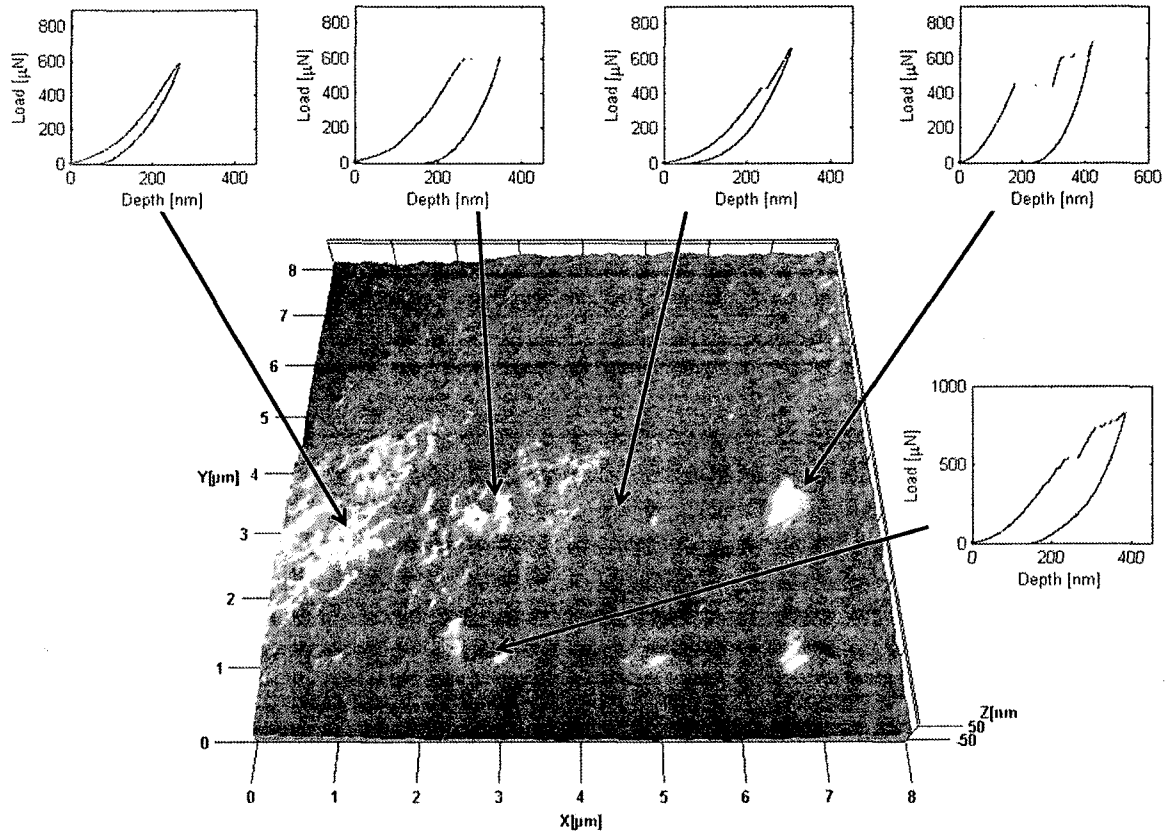

Figure 45: SPM image of the area on which an array of indents with a constant spacing in between the indents was carried out showing the evidence of permanent deformation for some of the indents and the absence thereof for other indents with several corresponding load-displacement curves.

Failure of the Fused Quartz Subjected to Nanoindentation

The failure mechanism of the pyrolytic carbon layers which were subjected to the indentation normal to the basal planes is not what is typically observed for continuous solid materials such as fused quartz. Figure 46 shows the residual impression of an indent performed using a cube corner indenter on the sample of a fused quartz. The release of the elastic strain energy occurred by crack propagation radially from the corners of the indent as opposed to the rupture of the basal planes observed for the bulk pyrolytic carbon. There is only a small pile-up of the material along the perimeter of the indent, but not nearly as much as in the case of the bulk PyroC. It suggests that the layers of the bulk PyroC samples that we tested failed by some variation of the delamination failure mechanism.

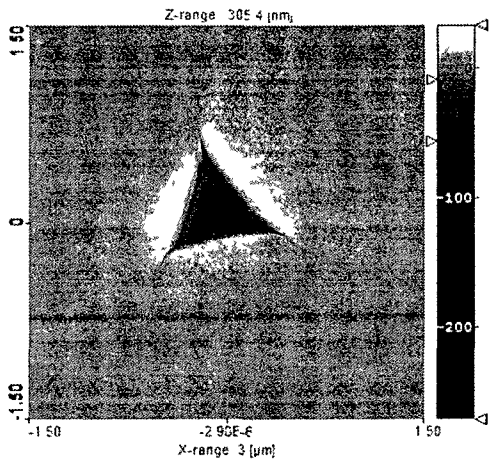

Figure 46: Indentation of the sample of a fused quartz that resulted in the permanent deformation with the crack propagation radially from the corners of the indent.

Layer Delamination of the Single Crystal Graphite

Barsoum et al[45] performed microindentation on single crystal graphite and also observed discontinuities in the load-penetration curves at high stress levels when indenting normal to the basal planes. They attributed this behavior to the series of events described below that result in delamination of the graphite layers. They proposed the kinking-based mechanism schematic[45] of which is shown in Figure 47.

According to this mechanism, at the initial stages of an indentation when the stresses are small under the tip indenting normal to the basal planes, the incipient kink bands comprised of two walls of dislocations of opposite polarity are formed which allow the elastic deformation upon load removal. However, when those stresses under the tip reach a critical value, the dislocation walls that were attached to the incipient kink bands separate from them and become mobile. They slip on the delamination plane causing permanent deformation in a form of the rupture of the basal planes. The transition from the incipient kink band formation which is reversible to the formation of the mobile dislocation walls which is irreversible cannot occur without delamination. The delaminated graphite planes pucker open similarly to what we observed for the samples of the pyrolytic carbon. The zone of influence of subsurface damage including dislocations, kinking and delamination can extend at least one radius away into the surface.

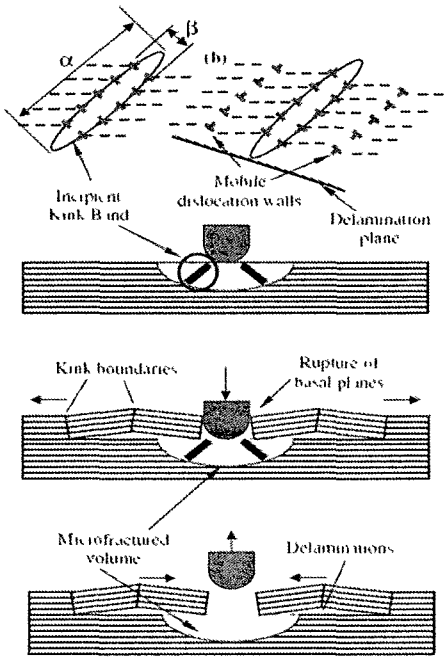

Figure 47: Schematic[45] of the kink band formation and layer delamination.

Proposed Failure Mechanism of the Bulk PyroC Subjected to Nanoindentation

We propose that the layers of the pyrolytic carbon material we tested failed by the mechanism shown in Figure 48 (a-b). Since the material is fairly crystalline, it is unlikely it could fail by the mean shear band deformation as we observed for the fused quartz. Moreover, the relatively low out-of-plane Young's modulus of this material allows for

the large tensile elastic strains which enable the fully reversible deformation for quite some depth. However, we believe that when the compressive stresses under the tip reach a certain level, they initiate the crack propagation along the indentation axis as shown in Figure 48 (a) causing the permanent tear of the graphene planes directly at the corners of the indenter. The cracks, however, arrest at weak interfaces and turn to grow in the plane of isotropy. When load is removed, the misregistry between the cracked surfaces and the elastic strain energy drive the ruptured planes upward forcing them to pucker open as shown in Figure 48 (b).

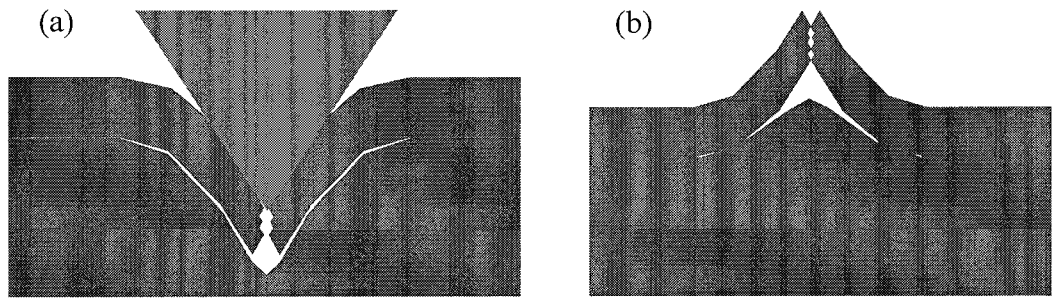

Figure 48: The proposed mechanism of the failure of the pyrolytic carbon layers indenting normal to the plane of isotropy.

The FEA model has shown that these stress levels are much higher for the indenters with the sharper included angles. This possibly explains why the cube corner tip with included angle of only 90° requires the least amount of force to cause the pop-ins. Despite the larger radius of curvature of the cono-spherical tip than of the Berkovich tip, its included angle of 60° is much sharper than the included angle of the Berkovich tip (142.3°). While it takes quite some depth for the material to reach past the spherical portion of the cono-spherical tip, its lateral component of the force vector becomes greater than the one of the Berkovich tip with the increasing depth. The acute angle of the inclined shoulder of the cube corner tip and of the cono-spherical tip exerts higher

lateral forces that are pushing the material in the lateral direction thus stretching the graphene layers. This is likely why the discontinuities for the cono-spherical tip are observed at high penetration depths only. The obtuse angle of the Berkovich indenter exerts forces predominantly in the direction of indentation and does not trigger the mobility of the dislocations, thus, resulting in an elastic deformation only.

Failure of Tempered Pyrolytic Graphite and HOPG Subjected to Microindentation

The microindentation load-displacement curves of the bulk PyroC samples using Vickers indenter exhibited the fully reversible behavior similar to the response obtained by the Berkovich indenter at the nanoindentation scale. The microindentation on the samples of the tempered pyrolytic graphite (TPG), however, produced the permanent deformation that is evident from both the load-displacement curves and from the PLM images of the residual impressions. The distinct feature of the TPG sample is that its microstructure has achieved a higher degree of graphitization as the result of the heat treatment, thus increasing the number of the graphene layers parallel to the plane of isotropy and reducing the fraction of covalent bonding in the deposition direction. We will now discuss how these factors may affect the indentation results.

The load-displacement curves of the tempered pyrolytic graphite are shown in Figure 49 (a-b) for the indentations normal and parallel to the plane of isotropy. Only the indentations normal to the plane of isotropy exhibited the pop-ins. They were not observed for the indentations in the other direction. However, the indentations in both directions produced a substantial amount of permanent deformation.

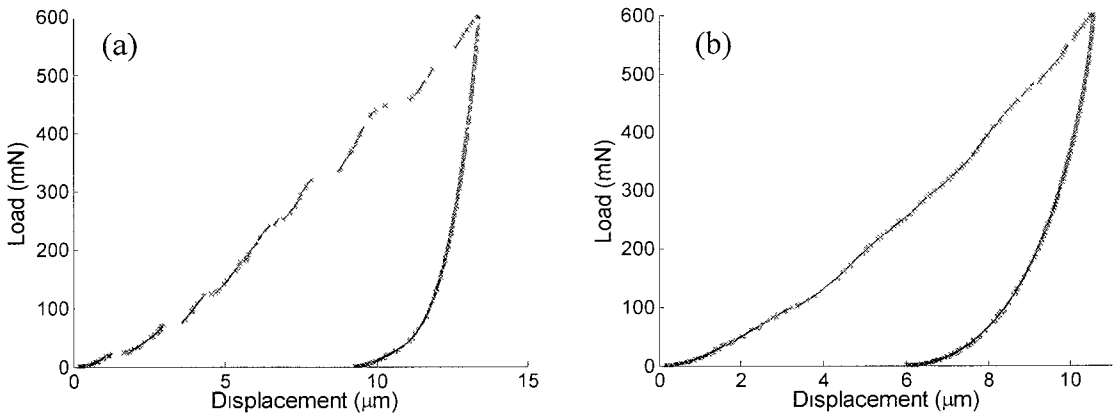

Figure 49: Microindentation load-displacement curves of the tempered pyrolytic graphite (TPG) (a) normal to the plane of isotropy and (b) parallel to the plane of isotropy.

This permanent deformation can also be observed in the PLM images shown in Figure 50 (a-b). The Vickers indenter left a deep impression on the surface of the tempered pyrolytic graphite when indenting normal to the plane of isotropy with the depth of about 75 percent of the maximum displacement.

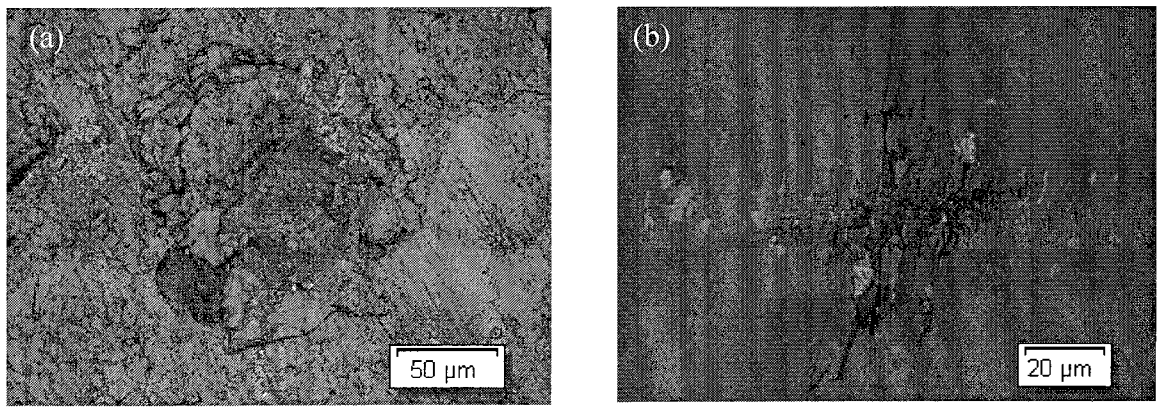

Figure 50: PLM images of the residual impressions created by the Vickers indenter in the directions (a) normal to the plane of isotropy and (b) parallel to the plane of isotropy of the TPG samples.

Also, there appeared to be a zone of the material pile-ups around the indent with the radius of one to two times the radius of the indent. These pile-ups were most likely caused by delamination of the graphite basal planes similar to what was observed by

Barsoum et al[45] for single crystal graphite. This argument is also supported by the presence of the discontinuities in the load-displacement curves.

We suspect that the combination of the increased apparent layer stack length of the TPG sample with the layers being more parallel with the plane of isotropy enhances the ability of an indenter to cause the layer delamination which is reflected in the prolonged discontinuities of the load-displacement curves. We do not have the knowledge of how the TPG sample was manufactured and to what post-treatment conditions it was exposed to, but according to Guellali et al[29,30], the heat treatment of a pyrolytic graphite at temperatures of over 2000°C for the low-temperature (LT) and 2900°C for the high-temperature (HT) PyroC leads to the decrease of the interlayer spacing and to the increase of the apparent layer stack length. This metamorphosis of the microstructure translates into the increased number of thinner graphite layers that become more parallel with the deposition plane. These changes are more pronounced for the LT PyroC samples than for HT PyroC samples and there is a potential to convert the lamellar microstructure of a LT PyroC sample to the microstructure of highly oriented pyrolytic graphite (HOPG) by the heat treatment. In spite of the fact that the samples of the bulk PyroC were determined to be the high-textured by Gebert et al[19], we suspect that TPG samples achieved even higher degree of graphitization by the means of heat treatment. However, this difference was not quantified.

The permanent deformation of the TPG sample was also observed when indenting parallel to the plane of isotropy. This deformation was represented by the cracks propagating in the direction parallel to the plane of isotropy and no discontinuities were observed in the load-displacement curves (Figure 49 (b)) indenting in this direction.

Crack propagation parallel to the plane of isotropy was observed not just in the vicinity of the indents but even some distance away from the indents as shown in Figure 51. The FEA model of indentation has shown that there is a zone of the tensile stresses on the surface of a substrate extending past the immediate point of the contact between the tip and the surface. The magnitudes of these tensile stresses are small comparing to the magnitudes of the axial stresses under the tip. However, those stresses might be above the critical value to break the weak Van der Waals bonds that hold the graphite basal planes together resulting in the small secondary cracks extending several diameters away from the immediate zone of an impact as shown in Figure 51 below.

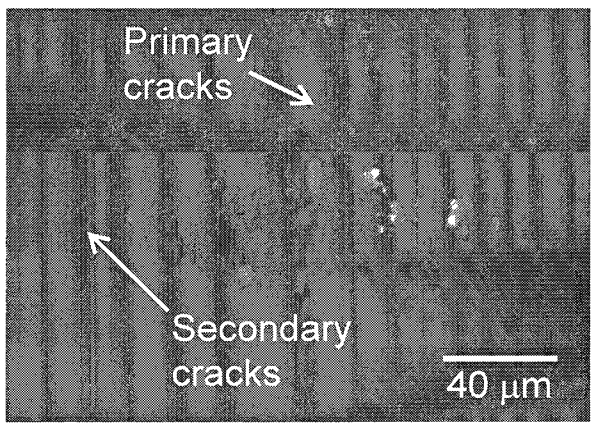

Figure 51: PLM image showing the primary and secondary cracks that resulted from the microindentation into the sample of the tempered pyrolytic graphite parallel to the plane of isotropy.

The reason for the crack propagation of the TPG sample when it is subjected to indentation parallel to the plane of isotropy can again be attributed to the high degree of graphitization of the graphite layers as the result of the heat treatment. The further alignment of the graphene layers parallel to the plane of isotropy greatly reduces the fraction of the strong covalent σ-bonds in the direction normal to the plane of isotropy. Therefore, the bonding that exists in between the graphene layers of the TPG sample is

governed by the weak Van der Waals bonds. We propose that the tensile stresses exerted by the indenter tip exceed the critical value and cause the crack propagation along the weak interfaces by tearing these weak bonds in the vicinity of an indentation. Furthermore, the tensile zone that extends on the surface causes the failure of the weak bonds in between the graphene sheets leading to additional secondary crack formation parallel to the plane of isotropy away from the immediate indentation site. The indentation in this direction was fully reversible for the bulk PyroC samples which is believed to possess a lower degree of texture and a higher fraction of covalent bonding in between the less aligned graphene layers.

Figure 52 shows the load-displacement curves as well as the PLM image of the indenter impression on the sample of a HOPG. Note the similarities with the corresponding plots and images of the TPG sample. In both cases, there is a large amount of pop-ins which occurs throughout the entire loading process causing a large permanent deformation.

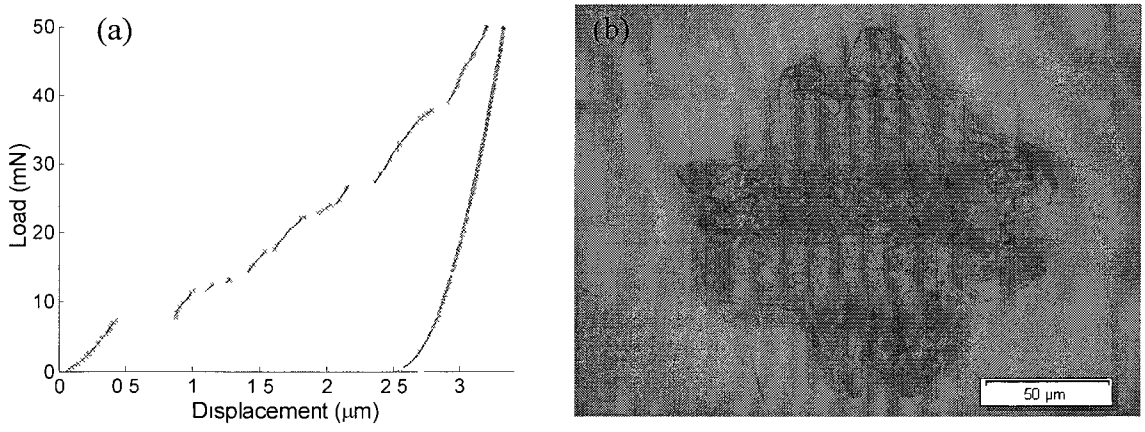

Figure 52: (a) The load-displacement curve of the HOPG sample and (b) the PLM image of the indenter impression showing the pop-ins and permanent deformation caused by Vickers indenter.

CHAPTER 6

SUMMARY AND CONCLUSIONS

This work was intended to provide the experimental support to the fidelity of the theoretical models that correlate the manufacturing conditions of C/C composites with the resulting microstructure and mechanical properties. Nanoindentation was the primary experimental tool in characterizing the elastic properties of C/C composites because it operates on a sub-micron length scale and enables measuring the spatial variation of the indentation modulus across the layers of the pyrolytic carbon as a function of distance from carbon fibers.

Pyrolytic carbon, however, is an anisotropic material and does not yield to the indentation in the same manner as the isotropic materials for which the analytic models used to deduce the properties such as Young's modulus and hardness were developed. The majority of the work presented in this thesis was performed on the samples of the bulk PyroC for which the elastic constants were measured using strain gage methods by us and ultrasonic phase spectroscopy methods by others. We used the same samples of the bulk PyroC to perform the nano- and microindentation to address the ability of indentation methods to capture the anisotropic elastic properties of the pyrolytic carbon.

We determined that pyrolytic carbon exhibits tension-compression anisotropy by performing the in-plane and out-of-plane tension and compression test using strain gage

methods. We measured the compression out-of-plane Young's modulus to be 5.2±0.3 GPa while the in-plane Young's modulus was measured to be 18.8±0.7 GPa in compression and 30.2±1.1 GPa in tension. We attribute the tension-compression anisotropy of the pyrolytic carbon to the buckling and puckering of the graphene planes when they are subjected to a compressive load yielding a lower modulus while straightening in tension resulting in a higher modulus. Also, there might be the disk-like voids that "buckle open" when loaded in compression.

We performed nanoindentation on the same samples of the bulk PyroC using the cube corner, Berkovich, and cono-spherical tips in the directions both normal and parallel to the plane of isotropy. Indentation normal to the plane of isotropy yielded values of the out-of-plane indentation modulus in the vicinity of 12 GPa for all three indenters which was more than a factor of two higher comparing to the out-of-plane Young's modulus measured by strain gages. This result suggest that indentation modulus is different from the Young's modulus in the direction of indentation and the difference depends on the degree of anisotropy of a given material which was also confirmed by the 2D axisymmetric FE studies on the effects of anisotropy on the resulting indentation modulus.

The expected out-of-plane indentation modulus of the bulk PyroC based on the approximations by Delafargue and Ulm[32] utilizing the measured elastic constants using strain gage methods was calculated to be 9.38 GPa. The 2D axisymmetric FE models also predicted the out-of-plane modulus to be within 9-10 GPa for all three indenters based on the elastic constants measured by strain gage methods. The difference between the expected and experimental values may be attributed to the viscoelastic behavior of the

experimental unloading curve which was not taken into the account in the theoretical predictions.

Nanoindentation parallel to the plane of isotropy yielded different values of the in-plane indentation modulus for all three indenter tips (6.67±0.79 GPa for the cube corner, 9.25±0.89 GPa for the cono-spherical, and 12.19±1.02 GPa for the Berkovich tip). We attribute the unexpectedly lower values of the in-plane indentation modulus, comparing to the out-of-plane indentation modulus of the bulk PyroC, to the nanobuckling deformation mechanism when indenting parallel to the plane of isotropy. Moreover, the FE studies have shown that the combination of higher compressive axial stresses with higher lateral tensile stresses further enhance the nanobuckling and this combination is dependent upon the geometry of the indenter. The cube corner tip, which is the sharpest of all three considered indenters, imposes the highest values of these stresses on the substrate and is more likely to cause the nanobuckling.

We also performed nanoindentation experiments on three different samples of C/C composites manufactured at pressures of 10, 20, and 30 kPa and at the temperature of 1100°C. In addition, we measured the extinction angles of the same samples using PLM to determine the degree of anisotropy of the pyrolytic carbon layers and to correlate the optical anisotropy with the structural anisotropy detected by nanoindentation.

The C/C composite sample manufactured at 30 kPa exhibited a higher in-plane indentation modulus (~18 GPa) than the samples manufactured at lower pressures. Also, the same sample exhibited the lowest degree of texture with the extinction angle of approximately 8° throughout the entire PyroC region. The 10 kPa sample exhibited an

indentation modulus of about 13 GPa through the PyroC thickness and an extinction angle of about 18° (high texture). No distinct gradients in the indentation modulus and in the degree of texture were observed either by nanoindentation or by extinction angle measurements.

Since nanoindentation was performed in the direction parallel to the plane of isotropy only, we propose that the lower indentation modulus observed for the PyroC with a high degree of order is attributed, once again, to the nanobuckling of the graphene planes under compressive load of the indenter. C/C composites manufactured at lower pressure appear to have higher texture PyroC than the samples manufactured at higher pressures. A lower indentation modulus of the high texture PyroC does not imply, however, that the material has inferior elastic properties. HT PyroC has a larger fraction of the strong σ-bonding in-plane and if loaded in tension, it is expected to exhibit a higher macroscopic elastic modulus.

Although most of the nanoindentation load-displacement curves were nearly elastic, we observed large discontinuities in some cases indenting normal to the plane of isotropy of the bulk PyroC samples. These discontinuities were triggered by the cube corner and cono-spherical tips at loads exceeding 400 μN and 5000 μN respectively. No discontinuities were observed for the Berkovich indenter. We also observed large material pile-ups around the site of an indentation.

We propose the damage occurs by tearing of the graphene planes directly at the corners of the indenter. These cracks rotate and propagate on the weak planes parallel to the surface. When load is removed, the misregistry between the cracked surfaces and the

elastic strain energy drive the ruptured planes upward forcing them to pucker open. This theory, however, has not been experimentally validated.

This work has identified the correlation between the indentation modulus obtained by indenting into a transversely isotropic material and the value of the Young's modulus in the direction of the indentation. However, more research is required to determine the relationships between these two parameters in order to deduce the elastic constants of anisotropic materials from the indentation load-displacement curves.

APPENDICES

APPENDIX A

Validation of the 2D Axisymmetric FE Modeling

The load-displacement curve obtained by the 2D axisymmetric FE model with isotropic elastic properties was validated against the theoretical load-displacement relationship for a spherical indenter proposed by Hertz[33]:

$$P(h) = \frac{4E}{3(1-\upsilon^2)}\sqrt{Rh^{3/2}} \tag{18}$$

where P is the load, E is the Young's modulus, v is the Poisson's ratio, h is the displacement, and R is the radius of the spherical indenter. The validation was performed on the substrate with the same dimensions and the element sizes used for the most of the FE studies. We used the geometry of the cube corner tip with 200 nm radius of curvature. However, since the indentation depth was only 100 nm, the contact between the indenter and the substrate did not exceed the spherical part of the tip; therefore, it was considered as a spherical indentation.

Figure 53 shows the load-displacement curves obtained by the 2D axisymmetric model and by the Equation 18. The FEA curve nearly overlaps the theoretical prediction curve which provides confidence in our models.

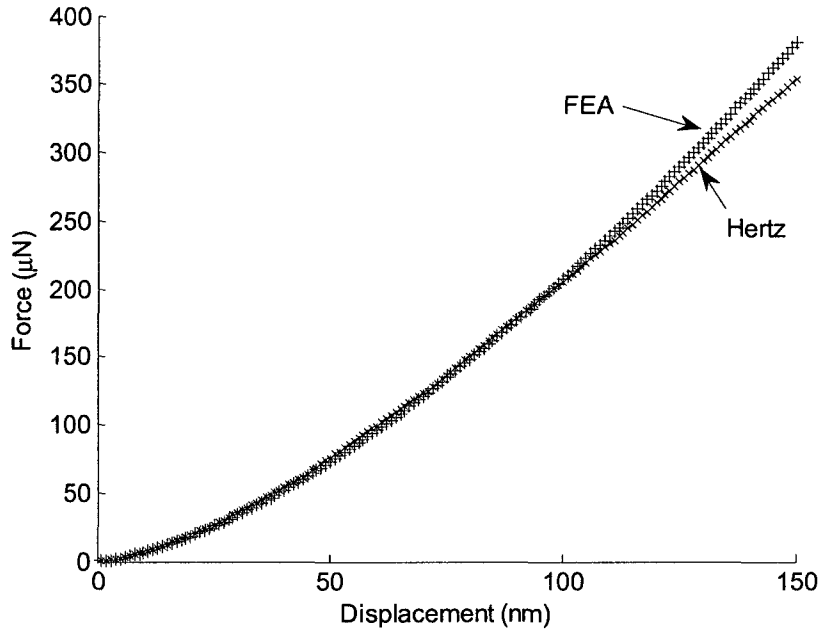

Figure 53: Load-displacement curves obtained by the 2D axisymmetric model and the theoretical prediction (Equation 18) showing an excellent agreement.

To quantify the agreement between the theoretical and the FEA predictions, we applied the power law fit to both of the load-displacement curves. The fit was perfect for the theoretical curve as expected. The fit for the curve predicted by the FEA also yielded an excellent fit with the R-squared value of virtually 1 and the power of nearly 1.5. We took the derivatives of these fits to obtain the expression for the slope at each 1nm increment. The differences in slopes over the range of 100nm were averaged and provided an agreement on the order of 1%.

APPENDIX B

Substrate Size Selection for the 2D Axisymmetric FE Modeling

The conventional procedure of deriving elastic properties from indentation load-displacement curves proposed by Oliver and Pharr[26] is based on the Sneddon's solution[24] for linearly elastic solids which assumes that the substrate is an infinite half-space. Therefore, to accurately represent the contact between a rigid indenter and a deformable substrate using FE modeling, the load-displacement curve obtained using the chosen substrate must achieve convergence with the load-displacement curves of bigger substrates.

Poon at al[47] performed FE studies to investigate the effects of the specimen geometry on the values of the measured load and displacement. They modeled the indentation experiment as a 2D axisymmetric problem with three-node linear triangular elements using ABAQUS® FE package. The indenter was modeled as a rigid tip with a conical shape and 200 nm radius of curvature. The substrate was an isotropic deformable body with E=70 GPa and ν=0.3. The width/length ratio of the substrate and the ratio of the substrate length to the indentation depth were varied to investigate the effects of the substrate geometry on the resulting load-displacement curves. They concluded that the convergence can be achieved when the width/length ratio is equal to unity or greater and when the ratio of the substrate length to the indentation depth equal to 100 or greater.

The general rule of thumb suggested by Fisher-Cripps[48] implies that the convergence is achieved when the ratio of substrate length to indentation depth is greater than 10. However, this ratio is suggested to be greater than 100 according to the FE studies by Poon et al[47]. We constructed several 2D axisymmetric models of our own with the length of the substrate being 10, 25, 50, and 100 times larger than the maximum indentation depth to examine at which substrate dimensions our models achieve convergence. We used a rigid conical tip with 200nm radius of curvature indenting into an isotropic deformable substrate with E=10 GPa and ν=0.3.

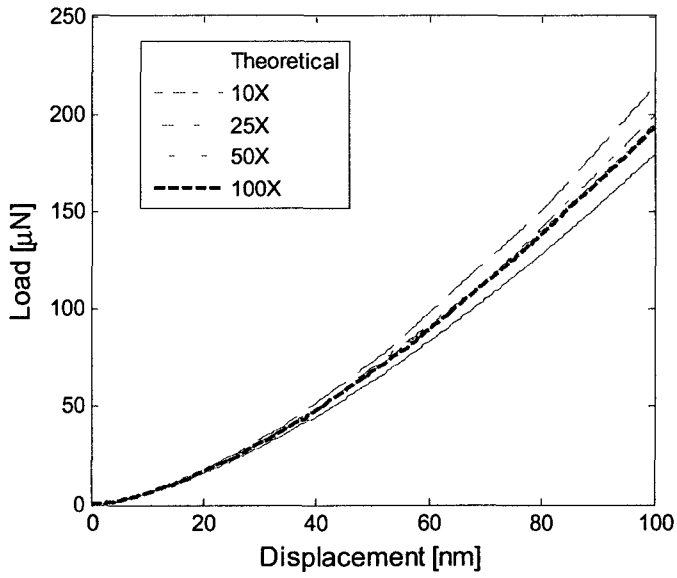

Figure 54: Load-displacement curves for different ratios of the substrate length to the indentation maximum depth.

The load-displacement curves for the 50X and 100X substrates nearly coincide which suggests that the ratio of the substrate length to the indentation depth does not have to exceed more than 50. Moreover, the load-displacement curve for the 25X substrate is only within 1%. Therefore, the ratio within the range of 30-50 times was found to be reasonable.

LIST OF REFERENCES

[1] Stahl D. Materials Engineering Newsline...Items of Interest to JME Readers. J Mat Eng 1988; 9(4):324-6.

[2] Piat R, Lapusta Y, Bohlke T, et al. Microstructure-induced thermal stresses in pyrolytic carbon matrices at temperatures up to 2900°C. J Eur Cer Soc 2007; 27(16):4814.

[3] Hu ZJ, Hüttinger KJ. Mechanisms of carbon deposition – A kinetic approach. Carbon 2003; 41(2):376-80.

[4] Reynolds W. Physical Properties of Graphite. Amsterdam, London, New York: Elsevier Pub Co 1988; 1-62.

[5] Oberlin A. Pyrocarbons. Carbon 2002; 40(4):7-24.

[6] Reznik B, Hüttinger KJ. On the terminology for pyrolytic carbon. Carbon 2002; 40(4):620-4.

[7] Reznik B, Gerthsen D, Zhang W, Hüttinger KJ. Texture changes in the matrix of an infiltrated carbon fiber felt studied by polarized light microscopy and selected area electron diffraction. Carbon 2003; 41(2):376-80.

[8] Reznik B, Norinaga K, Gerthsen D, Deutschmann O. The effect of cooling rate on hydrogen release from a pyrolytic carbon coating and its resulting morphology. Carbon 2006; 44(7):1298-352.

[9] De Pauw V, Reznik B, Kalhöfer S, et al. Texture and nanostructure of pyrocarbon layers deposited on planar substrates in a hot-walled reactor. Carbon 2003; 41(1):71-7.

[10] Pfrang A, Reznik B, Gerthsen D, Schimmel T. Comparative study of differently textured pyrolytic carbon layers by atomic force, transmission electron and polarized light microscopy. Carbon 2003; 41(1):181-5.

[11] Chen T, Reznik B, Gerthsen D, et al. Microscopical study of carbon/carbon composites obtained by chemical vapor infiltration of 0°/0°/90°/90° carbon fiber preforms. Carbon 2005; 43(15):3088-3098.

[12] Pfrang A, Reznik B, Schimmel T, Gerthsen D. Microstructure Analysis of a Carbon-Carbon Composite Using Argon Ion Etching. Microsc Microanal 2005; 11(1):46-55.

[13] Reznik B, Gerthsen D, Hüttinger KJ. Micro- and nanostructure of the carbon matrix of infiltrated carbon fiber felts. Carbon 2001; 39(2):215-29.

[14] Reznik B, Gerthsen D, Bortchagovsky E. An improved method for angular-resolved characterization of the optical anisotropy of pyrolytic carbon. J Microsc 2006; 224(pt.3):322-7.

[15] Bourrat X, Trouvat B, Limousin G, et al. Pyrocarbon anisotropy as measured by electron diffraction and polarized light. J Mat Res 2000; 15:92-101.

[16] Vallerot J-M, Bourrat X. Pyrocarbon optical properties in reflected light. Carbon 2006; 44(8):1565-71.

[17] Bortchagovsky E. Reflection polarized light microscopy and its application to pyrolytic carbon deposits. J Appl Phys 2004; 95(9):5192-99.

[18] Bortchagovsky E, Reznik B, Gerthsen D, et al. Optical properties of pyrolytic carbon deposits deduced from measurements of the extinction angle by polarized light microscopy. Carbon 2003; 41(12):2430-33.

[19] Gebert JM, Reznik B, Piat R, et al. Elastic constants of high-texture pyrolytic carbon measured by ultrasound phase spectroscopy. Carbon 2010; 48(12):3647-50.

[20] Bokros JC, Price RJ. Deformation and fracture of pyrolytic carbons deposited in a fluidized bed. Carbon 1966; 3(4):503-19.

[21] Sakai M, Hanyu H, Inagaki M. Indentation-induced contact deformation and damage of glass-like carbon. J Amer Ceram Soc 1995; 78(4):1006-12.

[22] Richter A, Ries R, Smith R, et al. Nanoindentation of diamond, graphite and fullerene films. Diam Rel Mat 2000; 9(2):170-84.

[23] Diss P, Lamon J, Carpentier L, et al. Sharp indentation behavior of carbon/carbon composites and varieties of carbon. Carbon 2002; 40(14):2567-79.

[24] Sneddon IN. The relation between load and penetration in the axisymmetric Boussinesq problem for a punch of arbitrary profile. Int J Eng Sci 1965; 3:47-57.

[25] Marx D, Riester L. Mechanical properties of carbon-carbon composite components determined using nanoindentation. Carbon 1999; 37(11):1679-84.

[26] Oliver W, Pharr G. An improved technique for determining hardness and elastic modulus using load and displacement sensing indentation experiments. J Mat Res 1992; 7(6):1564-83.

[27] Hofmann G, Wiedenmeier, Freund M, et al. An investigation of the relationship between position within coater and pyrolytic carbon characteristics using nanoindentation. Carbon 2000; 38(5):645-53.

[28] López-Honorato E, Meadows PJ, Xiao P, et al. Structure and mechanical properties of pyrolytic carbon produced by fluidized bed vapor deposition. Nucl Eng Design 2008; 238(11):3121-8.

[29] Guellali M, Oberacker R, Hoffmann MJ. Influence of heat treatment on microstructure and mechanical properties of CVI-CFC composites with medium and highly textured pyrocarbon matrices. Composites Sci Tech 2008; 68(5):1115-21.

[30] Guellali M, Oberacker R, Hoffmann MJ. Influence of heat treatment on microstructure and properties of highly textured pyrocarbons deposited during CVD at about 1100 °C and above 2000 °C. Composites Sci Tech 2008; 68(5):1122-30.

[31] Ozcan S, Tezcan J, Filip P. Microstructure and elastic properties of individual components of C/C composites. Carbon 2009; 47(15):3403-14.

[32] Delafargue A, Ulm FJ. Explicit approximations of the indentation modulus of elastically orthotropic solids for conical indenters. Int J Solids Struct 2004; 41(26):7351-60.

[33] Hertz H. Ueber die beruehrung elastischer koerper (On contact between two elastic bodies) 1882. Leipzig: Gesammelte Welke (Collected Works) 1895; Vol 1.

[34] Vlassak J, Nix W. Measuring the elastic properties of anisotropic materials by means of indentation experiments. J Mech Phys Solids 1994; 42(8):1223-45.

[35] Swadener J, Pharr G. Indentation of elastically anisotropic half-spaces by cones and parabola of revolution. Phil Mag A: Phys of Condensed Matter, Struct, Defects and Mech Prop 2001; 81(2):447-66.

[36] Elliot H. Axial symmetric stress distributions in aelotropic hexagonal crystals: The problem of the plane and related problems. Proc Camb Phil Soc 1949; 45:621-30.

[37] Hanson M. The elastic field for conical indentation including sliding friction for transverse isotropy. J Appl Mech 1992; 59:S123-30.

[38] Kachanov M, Shafiro B, Tsukrov I. Handbook of elasticity solutions. Dordrecht: Kluwer Academic Pub 2003; 340.

[39] Saint-Venant B. Mémoir sur la distribution des élasticités. J Math Pures et Appl Liouville 1863; Sér II(8):353-430.

[40] Cazacu O. A new hyperelastic model for transversely isotropic solids. Zeitschrift für angewandte Math and Phys 2002; 53(6):901-11.

[41] Worotnicki G. Stress measurements in anisotropic rocks, in Comprehensive Rock Eng (ed. Hudson J). Oxford: Pergamon Press 1993; 330-391.

[42] Gross T, Nguyen K, Buck M, et al. Tension-compression anisotropy of in-plane elastic modulus for pyrolytic carbon. Carbon 2011; in press.

[43] Oya N, Johnson D. Longitudinal compressive behavior and microstructure of PAN-based carbon fibres. Carbon 2001; 39(5):635-45.

[44] Riter Jr J. Interpretation of diamond and graphite compressibility data using molecular force constants. J Chem Phys 1970; 52:5008-10.

[45] Barsoum MW, Murugaiah A, Kalidindi SR, et al. Kink bands, nonlinear elasticity and nanoindentations in graphite. Carbon 2004; 42(8-9):1435-45.

[46] Galer M, Horvat L. Digital Imaging. Oxford: Focal Press 2001.

[47] Poon B, Rittel D, Ravichandran G. An analysis of nanoindentation in linearly elastic solids. Int J Sol Struct 2008; 45(24):6018-33.

[48] Fischer-Cripps AC. Nanoindentation. Berlin: Springer 2004.